Development of GaAs Detectors for Ionising Radiation

John M. C. Matheson

Department of Physics and Astronomy
The University of Glasgow
Glasgow
Scotland

Thesis submitted for the degree of Doctor of Philosophy

November 1993

ProQuest LLC.
789 East Eisenhower Parkway
P.O. Box 1346
Ann Arbor, MI 48106 – 1346

Abstract

This thesis presents an account of the development of particle detectors made on gallium arsenide semiconductor material. The state of the art in semiconductor detectors is reviewed and likely requirements for the future at LHC outlined. Fabrication of devices is described, as is their characterisation and testing in the laboratory. Less than full charge collection efficiency for devices fabricated on semi-insulating material has been explained in terms of a limited sensitive thickness. Reverse-bias leakage currents appear to be due to generation of carriers at surface states. The performance of materials grown by different processes is compared. Detectors have been tested in particle beams at CERN and analysis of test beam data is presented for single-sided devices and a double-sided device. The radiation hardness of the detectors is examined with reference to LHC requirements.

Preface

This thesis describes the development of gallium arsenide semiconductor particle detectors for application in the ATLAS experiment which will be used to study proton-proton collisions at the forthcoming LHC accelerator at CERN, Geneva. Radiation doses to detectors at this facility will be higher than those at any previous colliding beam machine and it is hoped that the gallium arsenide devices will provide a more radiation-hard alternative to the widely used silicon detectors.

The work was carried out as part of the RD8 Collaboration and depended on the participation of many people. The author was involved in the testing and characterisation of detectors in the laboratory and contributed to test beam running at CERN in the period 1991-1993. The analysis of test beam data presented here is his own.

Saverio D'Auria is acknowledged for the results from C-V and SEM measurements in Chapter 3. Robert Bertin tested the simple Schottky-Schottky devices at CERN. The pulse shape measurements in the same chapter were carried out by P.G. Pelfer, who was also responsible for the proton microprobe study. The MIP spectra for a simple device before and after irradiation in Chapter 4 were provided by Robert Bertin. The data analysis for the Telettra device before irradiation presented in Chapter 5 was performed by Saverio D'Auria and Ilvydas Matulionis.

No portion of the work referred to in this thesis has been submitted in support of an application for another degree or qualification in this, or any other, institute of learning.

Acknowledgements

I would like to acknowledge the support which I have received whilst carrying out this work.

Financial support was provided by the Science and Engineering Research Council and by Micron Semiconductor Ltd., Lancing.

I am grateful to Professor David Saxon for accepting me into the High Energy Physics group at the University of Glasgow, and to Professor Ken Smith for his supervision and for his proof-reading of this thesis.

Thanks in particular to Dr.Colin Raine and Dr.Saverio D'Auria for many useful discussions; thanks also to Val O'Shea and Dr. Robert Bertin. Dr.Andy Halley was responsible for my initiation to computing. Dave Martin, Alan Flavell and staff have provided assistance with further computer-related problems.

The technical staff of the Departments of Physics and of Electrical and Electronic Engineering are thanked for their assistance. Thanks to Alan Hamill for his fabrication skills and to Fred Docherty for his help in taking some of the measurements on simple devices. Catherine MacIntyre dealt with the bureaucrats at SERC on my behalf.

Thanks to my fellow research students Bill, Johnny and Paul for their friendship during the last three years, to Dev Lall, Gary van Breda and Graham Parker who have had to put up with me for rather longer and to Roy Percy and James Kean who apparently still have periods of lucidity after more than a decade.

Finally, I would like to thank my family for their support; it is to them that I dedicate this work.

Contents

Chapter 1

Introduction

1.1 Semiconductor Detectors- Principle of Operation

The first reported use of a semiconductor device for the detection of ionising radiation was that of McKay et al in 1951 [1]. In this case, a point-contact germanium diode was used in reverse bias to record the passage of alpha particles. At the present time, the applications for which semiconductor detectors are used are widespread, from the use of charge-coupled devices (CCDs) in television cameras to the tracking of particles in high energy physics experiments as part of the search for an ultimate theory of matter. In each case, the device retains in some way the structure of the reverse-biased diode.

The operation of semiconductor detectors depends on the so-called band structure of the material from which they are made [6]. The band structure represents the states available to electrons in a solid and determines its conduction properties. The simplest picture is that of a valence band, separated from a conduction band by an energy gap forbidden to electrons (Fig.1.1). Conduction may occur by the motion of electrons in the conduction band under the influence of an external electric field and by the motion of empty states (holes) in the valence band. A

full or empty band makes no contribution to conduction.

In the case of an insulator, the forbidden gap is large, so that the valence band remains filled with electrons, whilst the conduction band is empty and so no conduction can occur. In the case of a conductor, states at the top of the valence band overlap those at the bottom of the conduction band, so that there is no forbidden zone. Electrons are always present in the conduction band and holes in the valence band, allowing conduction. The limits to the passage of free charge carriers through the material are due to scattering by lattice vibrations (phonons). Thus, the conductivity of the material decreases as its temperature increases. A semiconductor has a band gap which is sufficiently small that some carriers may be thermally excited across the band gap. Thus, it will behave as an insulator at absolute zero and its conductivity will increase as its temperature rises.

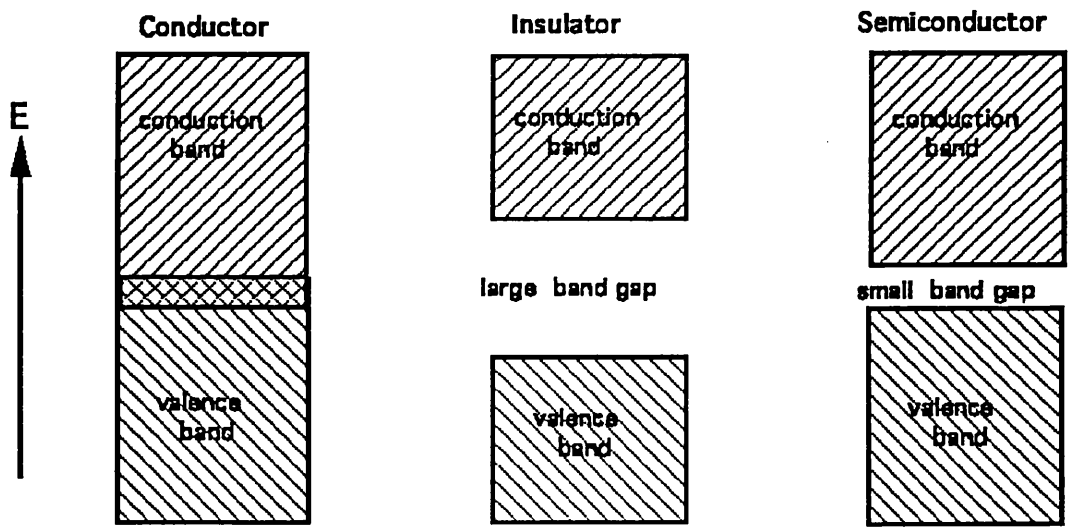

Figure 1.1: Energy Band Diagrams

In principle, a detector could consist of a piece of semiconductor material with an electric field applied across it; the passage of an ionising particle would promote electrons to the conduction band, leading to a current pulse in an external circuit. However, this is not a realistic solution, since the resistivity of commercially

available silicon, for example, is around 20 kΩcm at most. With a field applied across such a device sufficient to suppress carrier recombination, the resulting current through the device would have an associated shot noise which would swamp the signal of interest. The use of a diode-type configuration overcomes this problem.

A typical diode is made by forming a so-called p-n junction, which relies on the introduction of impurity atoms into the semiconductor lattice in order to affect its conduction properties. Considering a perfect silicon crystal at absolute zero, all the bonds between silicon atoms will be saturated, and no electrons will be free to conduct. If a group V atom is introduced to the lattice in place of a silicon atom, it will contibute an extra electron beyond those needed for bonding, which then becomes available for conduction (Fig.1.2).

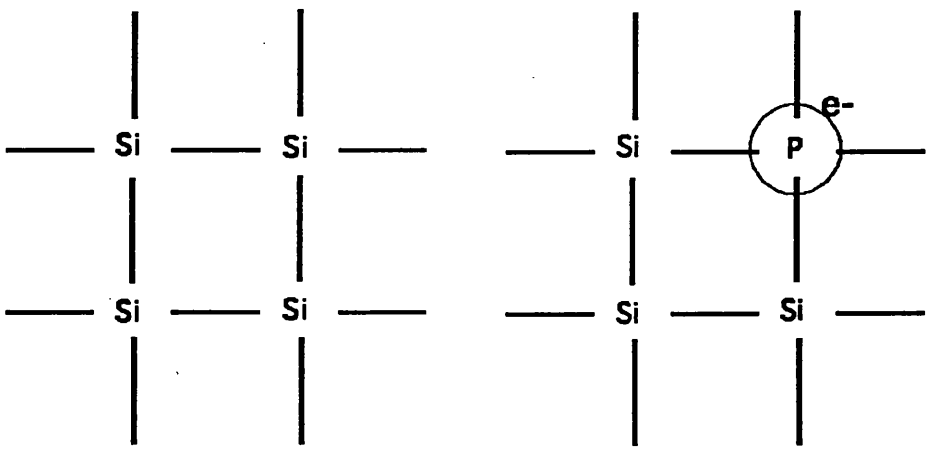

Figure 1.2: **Doping in Silicon**

Similarly, a group III atom will lead to a hole becoming available. In this manner, the conduction type and resistivity of a semiconductor material may be varied at will. This is known as doping; material in which conduction by electrons dominates is known as n-type, whilst that in which conduction by holes dominates is termed p-type.

If a piece of n-type material is brought into contact with a piece of p-type material,

holes will diffuse from the p-type side of the junction to the n-type side, where their concentration is less, according to Fick's Law. Electrons will diffuse in the opposite direction. The separation of charges will lead to a field opposing the diffusion, which will increase until the tendencies for carriers to drift and diffuse are balanced (Fig.1.3).

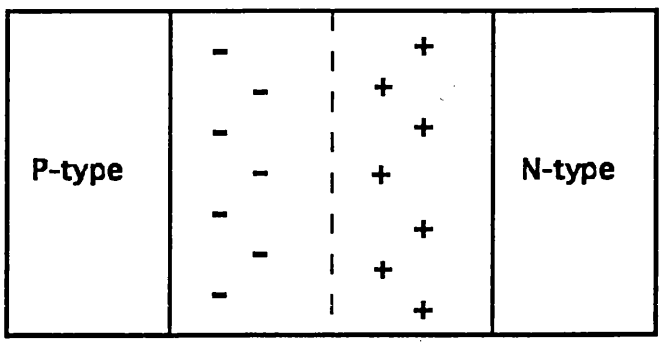

Figure 1.3: **P-N Junction**

Close to the interface, there will lie a region with no free charges; this is termed the depletion region. If a bias voltage is applied across this p-n junction, with the p-side negative with respect to the n-side, free carriers will be pulled away from the interface; the depletion region becomes wider and current cannot flow through the junction. If a bias is applied in the opposite sense, carriers are forced towards the interface and charges of opposite sign come close enough to recombine, causing a current to flow. This is the manner in which a diode behaves.

For the device to be used as a detector, it must be reverse-biased; now a field across the depletion region sufficient to prevent carrier recombination may be sustained without the large current flow of a conduction device. An ionising particle traversing the detector will deposit charge in the device, and that charge in the depletion region will be swept out by the reverse-bias field, leading to a current pulse in an external circuit.

1.2 Manufacture of Detectors

It is not a practical method to form a device from two separately doped pieces of material. The simplest method of producing a working device is to use a metal Schottky barrier contact in place of the p-layer on top of n-type material. If the work function of the metal is larger than that of the semiconductor, then there will be electrons in the semiconductor with sufficient energy to fill unoccupied states in the metal and a flow of electrons will occur from the n-type material, leading to the formation of a depletion region as before. The Schottky barrier contact is identical in behaviour to a p-n junction in which the p-side is very heavily doped. The point-contact diode was the first application of this type of junction, but it is now the case that metal is deposited onto the semiconductor surface by evaporation to give a reliable device. If a metal is used whose work function is smaller than that of the semiconductor, no depletion region can be formed, and current is able to pass across the junction in either direction; this is termed an ohmic contact.

The most common semiconductor detectors at present in use are silicon devices made by the planar process developed for the manufacture of integrated circuits [8]. They typically make use of ion-implanted junctions. Schottky contacts can be vulnerable to contamination on the surface of the crystal during processing, which can lead to increased reverse bias leakage currents; thus the first step in the planar process is to grow a layer of oxide on the silicon wafer which acts to protect it [5]. The oxidation is carried out in an atmosphere of oxygen at $1000^{o}C$ (Fig.1.4). Photoresist is spun onto the wafer, and baked to cure it. Where the implants are required, the oxide layer must first be removed. The photoresist is exposed to an ultra-violet light source through a mask. The mask consists of a glass plate with an opaque metal film upon it defining the device structure. Development of the photoresist leads to it dissolving in those areas where it was exposed to light; this leaves the oxide exposed in those areas where it must be etched off. A hydrofluoric acid etch is used. The crystal is then

ion implanted by accelerating impurity ions in an electrostatic accelerator and allowing the collimated beam to impinge upon the wafer. The depth to which the implant penetrates is determined by the energy used, and the oxide layer should be thick enough to stop the ions before they reach the silicon in the areas where an implant is not required. Having doped the semiconductor in this way, it must be annealed in a furnace at $600°C$ for 2 hours. This has the function of allowing self-repair of damage to the crystal structure caused by the incident ions, and allows impurity atoms to migrate onto lattice sites, which is necessary for them to become electrically active [4]. Contacts to the device are made in the same general way using photolithography, but depositing the required metal by evaporation. The devices are then packaged as required.

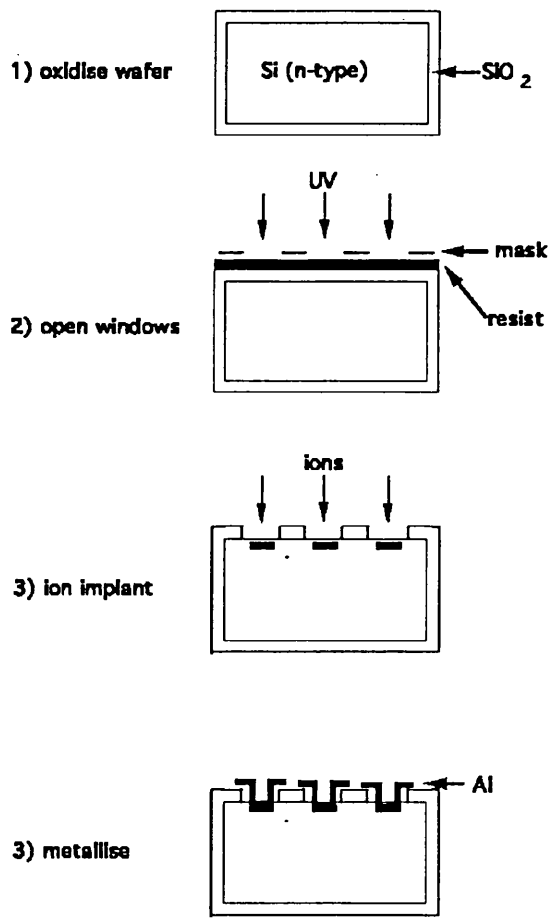

Figure 1.4: The Planar Process

1.3 Detectors for Spectroscopy

Different types of detector are used for different applications. Single element devices with Schottky contacts are commonly used for energy measurements of heavy charged particles such as heavy ions and fission fragments [3], which would otherwise lose a significant amount of their energy in the layer outside the depletion region, where the device is not sensitive. For very heavily ionising particles, the charge read out from the detector may be smaller than that expected from measurements on less heavily ionising particles. This is due to recombination of carriers along the particle track, and is termed the pulse height deficit. It may be minimised by use of lower resistivity silicon which leads to a higher average field across the device at depletion, or by use of non-injecting contacts which allow an increase in field by over depletion. Non-injecting contacts will be discussed later. In both cases, the increased field separates the charge along the particle track more quickly, suppressing recombination. Carrier recombination is characterised by the minority carrier lifetime of the material, and this should be as high as possible for any semiconductor detector. Schottky barrier devices are also frequently used in alpha particle spectroscopy. As there is a wide availability of monoenergetic alpha sources, it is common to use measurements of known sources to evaluate the performance of new detectors.

For more penetrating radiation, measurement of energy is made more difficult by the limited depletion depth of the detector. For greater depletion depth, a greater reverse bias voltage is required, until the field in the device reaches the breakdown field of the semiconductor. This limits the achievable depletion depth of devices made on commercial high-resistivity silicon to the order of 1mm. A reduction in the free carrier concentration would allow a greater depletion depth for the same maximum field, but the purity of crystal which can be obtained in practice limits this. A method of overcoming this problem is that of lithium drifting, which is used with both silicon and germanium.

The principle of this technique is to take a piece of highly pure p-type material, and to compensate the p-type impurities with lithium donor atoms. This is achieved by diffusing lithium into one surface of a p-type crystal, forming a p-n junction, which is then reverse-biased. The temperature of the crystal is increased in order to speed up diffusion, and the field draws the lithium ions into the p-type material, where their concentration will tend to increase until exact compensation between acceptor impurities and lithium donors is achieved. The free carrier concentration of the material may be kept below $10^9 cm^{-3}$ in this way, allowing depletion depths of a few mm. The mobility of lithium ions in germanium is sufficiently high that the detector must always be cooled in order that the compensation is not lost. Germanium lithium-drifted (Ge(Li)) devices are commonly stored and operated at liquid nitrogen temperature.

Since the atomic mass of germanium is greater than that of silicon, its photoelectric cross section is higher; thus Ge(Li) devices are used for gamma-ray spectroscopy except at low energies. Si(Li) devices are used for beta spectroscopy, since the smaller atomic number will in this case lead to fewer incident betas being backscattered out of the device.

1.4 Position-Sensitive Detectors

1.4.1 Microstrip Detectors

The simplest form of position-sensitive detector is the microstrip type (Fig.1.5). A typical microstrip device consists of a slab of hyperpure, slightly n-type silicon, $300\mu m$ thick, a few cm^2 in area with implanted p^+-type strips on one side. On the other side, an n^+ implant is used, ohmic contacts being made to the implants. The device is thus an array of individual detectors, which are able to give spatial information in one dimension.

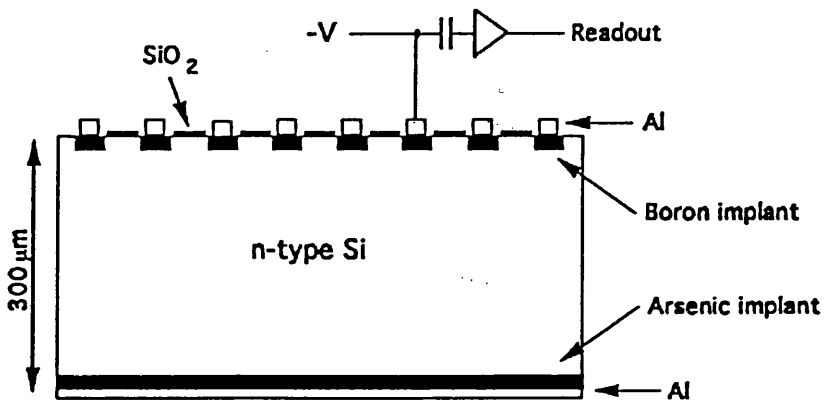

Figure 1.5: Typical Microstrip Detector

Two dimensional spatial information may be obtained by using two such devices with their strips orthogonal to each other, whilst in a high energy physics experiment, many layers of such devices may be used to track the daughter particles of a collision. In early experiments using microstrip devices, the lack of VLSI readout led to the use of readout by capacitive coupling between strips. In this way, it was not necessary to instrument every channel and the readout electronics, with their associated bulk and heat generation, were minimised. More recently, ASICs[1] have become available which may be bonded channel for channel to the detectors without the bulk of hybrid electronics. By reading several adjacent channels, for any hit, the centroid of the charge distribution left by

[1]Assignment Specific Integrated Circuit

the passage of an ionising particle may be found to a greater accuracy than the strip pitch. The accuracy achievable is limited in practice by the signal to noise ratio of the device, according to:

$$\frac{\sigma x}{s_A} = a_{cf} \cdot \frac{ENC}{Q_s} \tag{1.1}$$

where s_A is the amplifier pitch, or the strip pitch for the case where all strips are read out, a_{cf} is the centroid finding constant, ENC is the equivalent noise charge for one channel, and Q_s is the signal charge [6].

The spatial resolution of any position-sensitive semiconductor detector is limited in principle by the probability of an incident minimum ionising particle (MIP) ejecting a delta ray from its path with sufficient energy to shift the centroid of the charge distribution [7] (Fig.1.6).

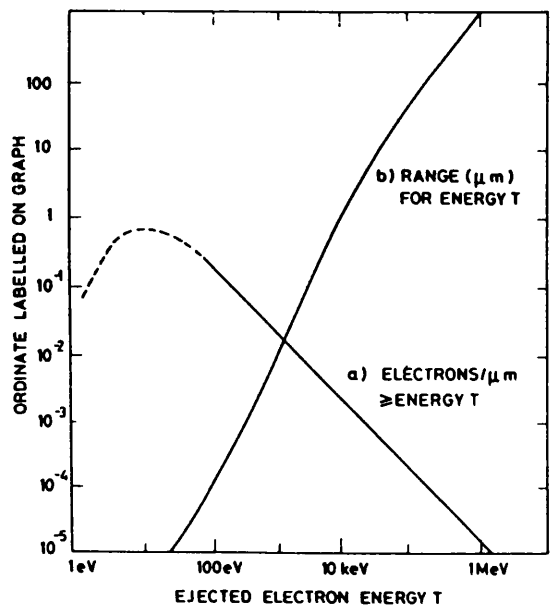

Figure 1.6: **a) No. of electrons ejected by a MIP per μm of path with energy T. b) Range vs. T (From [17])**

Thus, the thinner the detector, the better its position resolution can be in principle, but the lower its signal to noise ratio for MIPs. A practical limit for

position resolution in typical microstrip devices is of the order of $1\mu m$ (Fig.1.7).

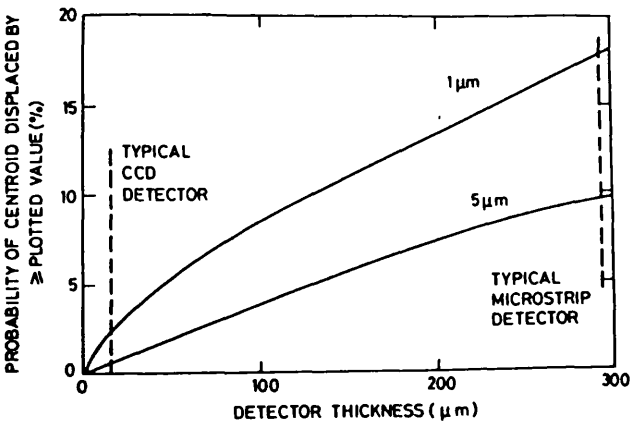

Figure 1.7: **Detector precision limitations from δ electrons for tracks at normal incidence as a function of detector thickness (From [17])**

The trend in the development of microstrip devices has been towards the integration of biasing resistors and coupling capacitors onto the device itself. AC-coupled strips may be produced by leaving a layer of oxide above the strip implants, and evaporating metal strips onto the oxide. Effectively a parallel plate capacitor is formed between the implant and the metal. Biasing resistors have been made using polysilicon and also by exploiting the resistivity of the bulk material. A further method of biasing strips has used a field effect transistor fabricated between the strips and a biased implant. The resistance between the implant and the strips may then be altered by a control voltage applied to the FET gate [10].

A recent advance in the microstrip configuration has been the development of double-sided devices, which allow the gathering of spatial information in two directions for one device thickness, thus minimising scattering material in the path of the particles emerging from a collision. Another advantage is that the charge collected at each side should be the same for each hit, allowing better discrimination between multiple hits and better rejection of false hits than is possible with two crossed single-sided devices. The construction of a double

sided device is necessarily more complicated, however.

The naive solution of structuring the n^+ implantation into strips as is done for the p^+ side cannot be used, because positive fixed charges are invariably found at the interface between the silicon and the oxide. These charges attract electrons to the silicon surface below the oxide, forming a so-called accumulation layer which shorts out the n^+-type strips. Several methods have been used to overcome this; one relies on separating the strips using a p^+-type implantation between them [9] (Fig.1.8).

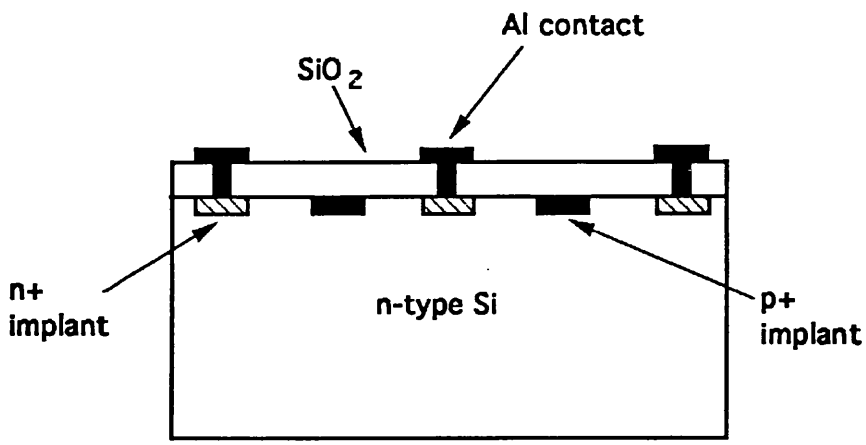

Figure 1.8: **Ohmic Strip Isolation**

Another method, used with AC-coupled strips involves extending the strip metallization so that it is able to be used as a field plate, repelling the electrons from the interface [11]. Dedicated polysilicon field plates have also been employed. Devices have also been fabricated in which the n^+ implantation is omitted entirely, the p^+ isolation implants serving to define areas in which the accumulation layer itself is employed to give an n^+ region. Double-sided microstrips have been sufficiently developed to be used in large collider experiments; for example, in the vertex detector of the ALEPH experiment [12] at CERN.

1.4.2 Pixel Detectors: Microdiode Arrays

The definition "pixel detector" is usually taken to refer to any detector in which the sensitive area is covered by a mosaic of sensitive elements, rather than strips. This definition refers to both the microdiode array and the charge coupled device. The former is conceptually simpler, and will be dealt with first.

The simplest microdiode array is identical to a single-sided microstrip device, apart from the subdivision of the strips into individual pads. The principal advantage over crossed or double-sided strips is the better resolution of multiple hits. The central technological problem with this type of device is the means of reading out the pads. The simplest solution has been to make a flat kapton readout cable with readout lines on its upper side, which are connected via plated-through holes to an array of conducting pads, one for each detector element. The pads are glued to the element metallisations using conductive epoxy [13]. A similar solution is to grow on the surface of the device a thick layer of oxide, upon which conductive metal tracks may be layed down to take the signals from each pixel to bond pads at the edge of the detector chip. The performance of either method is liable to suffer from parasitic capacitances between signal lines and detector pads from which they are isolated [14].

Methods of avoiding the parasitic capacitance problem are to use "flip-chip" technology or to fabricate the readout electronics directly onto the pixel, which open up interesting possibilities for data processing at the front end itself. The former method relies on fabricating the readout electronics on a separate substrate to the detector; interconnect is provided by metal pads on which solder or indium bumps are applied [15]. The two chips are brought face to face and joined by pressure in the case of indium bumps (Fig.1.9); for solder, heat must be applied. The method of growing the electronics on the detector itself is the most ambitious, and also the most technically difficult. Prototype devices have been made [16], but neither this nor any other microdiode array has yet reached maturity enough

to be used in a collider experiment.

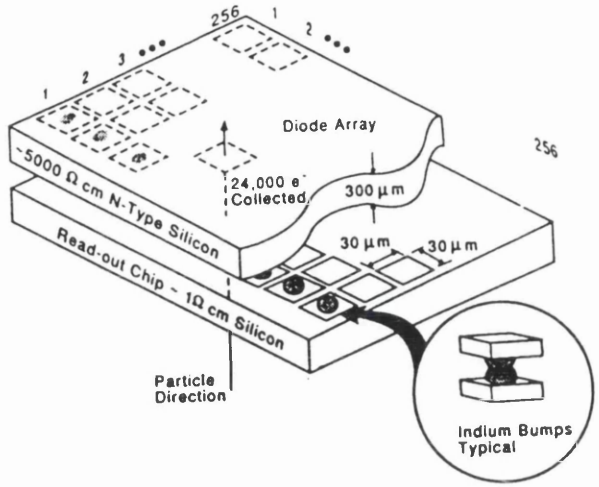

Figure 1.9: **The "Flip-Chip" Hybrid Technology (From [15])**

1.4.3 Pixel Detectors: Charge Coupled Devices

A diagram of a typical, buried-channel device such as might be used in particle detection is shown. Consider first one pixel. This has a structure similar to a MOS diode (Fig.1.10).

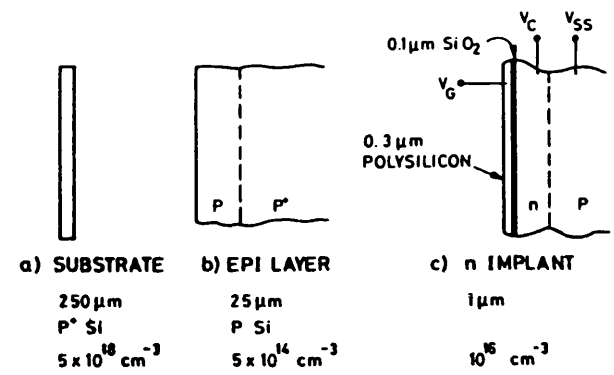

Figure 1.10: Cross-Section Through a Typical CCD (From [17])

It consists of a p-type substrate, typically $250\mu m$ thick, onto which is grown $25\mu m$ of epitaxial p-type silicon. The surface of this is then implanted to be n-type to a depth of around $1\mu m$, forming a p-n junction. A layer of oxide and a conductive polysilicon electrode follow. If the p-n junction is reverse biased and an ionising particle traverses the pixel, holes will be swept into the p-type substrate and electrons will be swept to the silicon-silicon oxide interface. Here they would be lost to trapping and recombination; however if a suitable bias is applied on the polysilicon electrode, electrons may be repelled from the interface itself. A potential mimimum may be formed and the electrons held in the epitaxial region, where their recombination lifetime is longest.

The entire CCD is made up of such pixels, defined in one direction by p^+ isolating implants, and in the other direction by poysilicon electrode strips (Fig 1.11). Readout proceeds by altering the potential of the polysilicon electrodes so that charge is transferred from one pixel to the next through the epitaxial layer. The charges stored on all the pixels between each pair of polysilicon strips are brought

in parallel, a row at a time, to a readout register, from which they are read sequentially. In this way the whole surface of the device is scanned.

The technology of CCDs has reached an advanced stage, principally due to their application in optical imaging, whence the use of optically transparent polysilicon rather than an opaque metallisation in the structure described. They have also been implemented in the NA32 fixed target experiment at CERN [7] and in the SLD experiment at the SLAC collider [17]. They can in principle give spatial resolutions which are superior to those of detector types with thicker active regions, although for detection of MIPs they must be cooled in order to achieve a good signal to noise ratio.

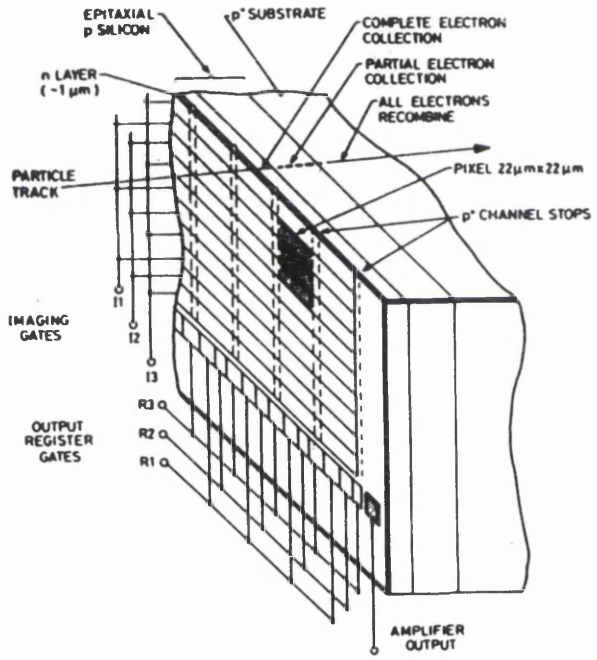

Figure 1.11: **Pixel Structure of a Typical CCD (From [17])**

1.4.4 Silicon Drift Chambers

The silicon drift chamber [18] is, in cross-section, two $p^+ - n$ junctions with the n-sides back to back (Fig.1.12). An edge contact allows the middle of the device to be held at ground potential, so that negative biasing of the p^+ regions creates a potential well at the centre of the device into which electrons deposited by an incident ionising particle will fall. The p^+ regions are fabricated in the form of parallel strips, and are biased so that an additional, linear field is created along the length of the device. The two fields combined produce a potential "gutter" from one end of the device to the other. Electrons drift down the gutter to collecting anodes at one end of the device.

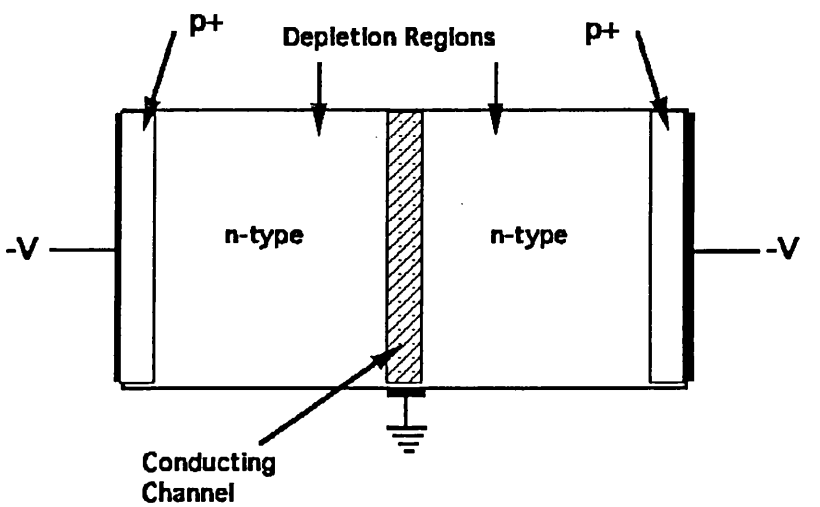

Figure 1.12: Cross-Section Through a Silicon Drift Chamber

Position information in one direction is available from the knowledge of which collecting anode bears a signal and in the other direction from the time between incidence of the particle and collection of the signal (Fig.1.13). The drift velocity must be known in the device from a calibration.

Silicon drift devices have been used in a prototype detector for tracking in the UA6 experiment at CERN, where a resolution of $15\mu m$ was obtained [19]. This performance was worse than expected due to inhomogeneities in the doping which

caused local variations in the drift field.

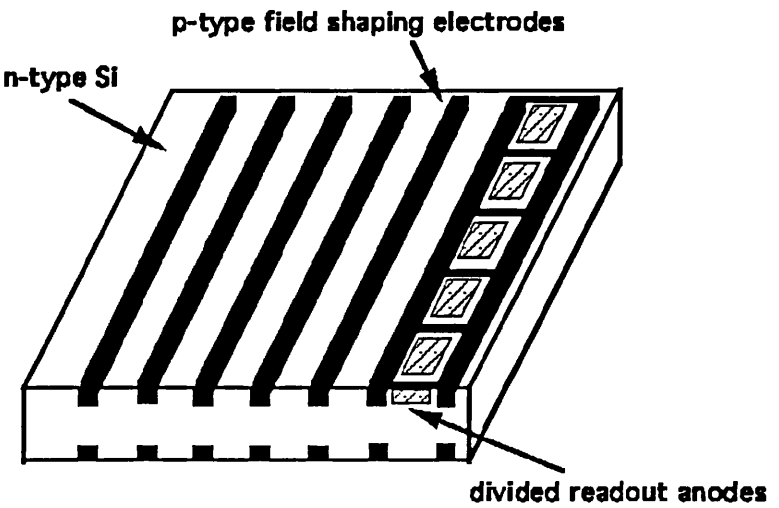

Figure 1.13: Schematic of a 2D Drift Detector

1.5 Position Sensitive Detectors for LHC

1.5.1 The Use of PSDs in HEP

Position-sensitive silicon detectors for high energy physics were developed in order to study the decays of the charmed particles which were discovered in 1974. These have lifetimes in the region of 10^{-13} to $10^{-12}s$, typically travelling $\sim 1mm$ from the primary vertex before decaying; the requirement for tracking devices was to separate the secondary, decay vertex from the primary interaction point. The nuclear emulsions and bubble chambers which were then common could provide the necessary tracking accuracies, but had very low data-taking rates and could not provide an on-line trigger. These limitations were overcome by the use of microstrip devices, as in the NA11 experiment at CERN, for example. Here, the hadronic production of charmed particles in a beryllium target was successfully studied using a vertex detector consisting of six planes of silicon microstrips [5]. Since that time, silicon detectors have been used in many HEP experiments, and indeed are used in vertex detectors for all four of the large experiments on the LEP collider at CERN. Preparations are now in progress for the building of the next generation of collider experiments, which will study proton-proton collisions from the Large Hadron Collider (LHC) machine, to be built in the LEP tunnel (Fig.1.14). As will be discussed, if use is to be made of semiconductor detectors for tracking and vertex detection, they must perform in a much more hostile environment than has been the case in the past.

1.5.2 The Objective of the LHC

The LHC machine will be used to investigate further the "Standard Model" [26] of the structure of matter. At the present time, the particles of which all matter is made are believed to consist of three generations of leptons:

$$\begin{pmatrix} e \\ \nu_e \end{pmatrix} \quad \begin{pmatrix} \mu \\ \nu_\mu \end{pmatrix} \quad \begin{pmatrix} \tau \\ \nu_\tau \end{pmatrix}$$

and three generations of quarks:

$$\begin{pmatrix} d \\ u \end{pmatrix} \quad \begin{pmatrix} s \\ c \end{pmatrix} \quad \begin{pmatrix} b \\ t \end{pmatrix}$$

In this scheme, each generation from left to right is a heavier analogue of the preceding generation. Experiment has precluded the existence of more than three such generations [27] and the top quark, t, has not yet been experimentally observed. For every particle in this scheme, there exists an anti-particle with the same mass but opposite charge. Leptons and quarks are all fermions. Forces between these particles are due to the exchange of gauge bosons. Four forces occur within the Standard Model; the electromagnetic force, the weak force, the strong force and the gravitational force. The gravitational force is important only for the behaviour of macroscopic bodies, and a successful, quantised picture for its action has not been found. The electromagnetic force is responsible for the interactions between electric charges and is carried by the massless photon. The weak force governs interactions such as beta decay, and is carried by the massive vector bosons W^+, W^- and Z^o. All particles are subject to the weak force. The strong force is responsible for the cohesion of atomic nuclei, and is carried by an octet of massless gluons.

The electron, e, muon, μ, and tau, τ carry unit electric charge and also carry mass, whilst the neutrinos, ν, are all without electric charge and are thought to be massless. The down, d, strange, s, and beauty (or bottom), b, quarks carry an electric charge of $-\frac{1}{3}e$ whilst the up, u, charm, c, and top, t, quarks carry $\frac{2}{3}e$. All quarks have mass and carry a colour charge of red, green, or blue which combine to form only colourless composite states. It is the colour charge to which the strong interaction couples, and those composite particles subject to the strong force are termed hadrons.

The central question to be answered by experiments at LHC is that of mass generation. The photon and gluons are massless; why should the bosons of the weak force be massive? A theoretical answer was provided by Higgs, who proposed the existence of an additional field, with associated Higgs bosons. Three of these are "absorbed" by the originally massless weak bosons, allowing them to acquire mass. There also remains a massive Higgs boson, which should be detectable by experiment, if the theory is correct. An extension of the Higgs mechanism is used to account for the masses of the fermions. It is planned to undertake a search for the Higgs boson at the LHC.

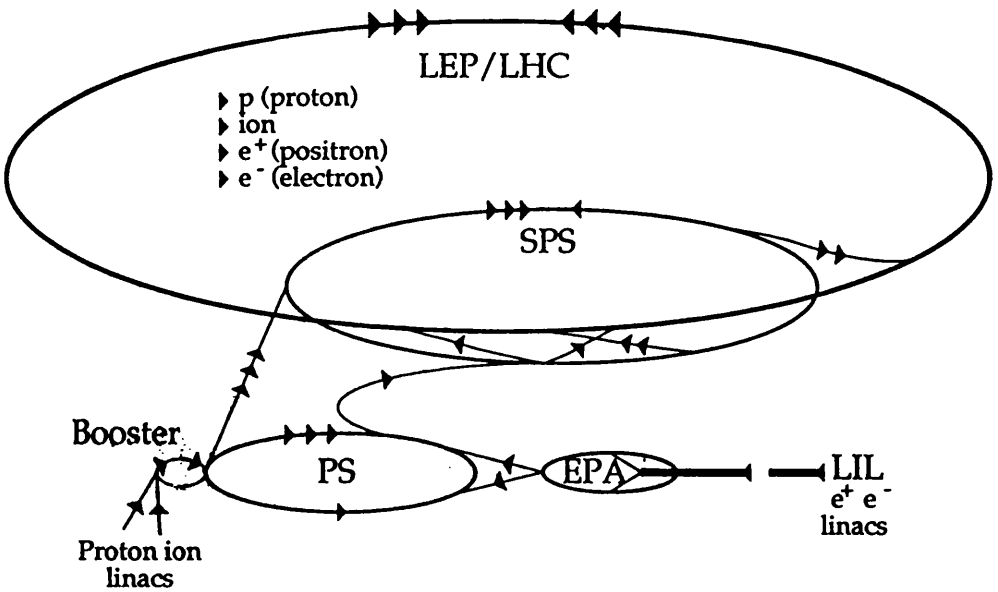

Figure 1.14: The CERN Accelerator Complex (From [21])

1.5.3 The LHC and the ATLAS Detector

There is no prediction of the Higgs mass: by the time the LHC comes on stream, however, the region up to 80-90 GeV will have been probed by the LEP 200 machine. This, then, represents the lower end of the mass range which will be of interest. Despite the lack of a prediction for the mass itself, for any postulated Higgs mass, the likely behaviour of the particle has been widely studied and is well known. As the Higgs mass approaches ~1 TeV, its width increases until it is no longer meaningful to think of a particle with a specific mass [20]. The energy range of interest for a Higgs search at LHC is then ~90 GeV to ~1 TeV.

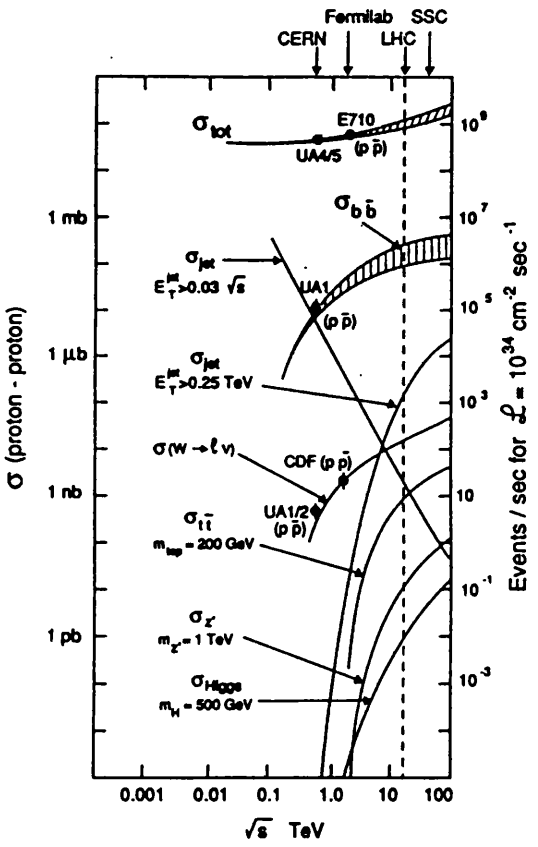

Figure 1.15: **Energy Dependence of Some Characteristic Cross-Sections (From [24])**

Collision energies of this magnitude are difficult to achieve with electron acceler-

ating rings, due to energy loss as synchrotron radiation, so that the LHC will be a proton-proton collider. Each proton is composed of quarks and gluons, and a collision between these single constituents with energy well in excess of 1 TeV per particle is required. Thus, the LHC will have an energy of 8 TeV per beam, and a luminosity of $10^{34} cm^2 s^{-1}$ in order to achieve a sufficient rate of the interactions of interest [21]. A bunch crossing time of 25 ns will be used, leading to $\sim 10^9$ events per second in total; for a 500 GeV Higgs, $\sim 10^{-2}$ Higgs creations per second are expected (Fig.1.15). The enormous number of charged particles passing through a detector at LHC is expected to lead to a stringent requirement for radiation hardness. This flux will decrease as r^{-2} away from the beam pipe; in addition, there is expected to be an isotropic flux of albedo neutrons from the calorimeter within the tracking volume. In present collider experiments, radiation damage problems within the detectors are predominantly due to synchrotron radiation and beam loss; for the first time at LHC, radiation levels will be dominated by particles from the interactions themselves.

A diagram of a possible layout for the proposed ATLAS detector is shown (Fig.1.16). The inner detector consists of a semiconductor vertex detector, semiconductor tracking detectors, and microstrip gas chambers [23]. These are surrounded by a superconducting solenoid producing a field of 2 Tesla. Charged particle track reconstruction allows the determination of momenta and charge sign from the track curvature in the magnetic field.

Outside the superconducting solenoid lies the electromagnetic calorimeter, which will probably be an accordion-type structure using lead as the converter and liquid argon as the shower sampler material, although other structures are under consideration. Beyond the electromagnetic calorimeter will lie the hadron calorimeter, which will use steel as the converter and for which several options are under consideration for the sampler type. Separate hadron calorimeters for jet identification will be used in the forward regions.

The outermost detector is that for muons, which will consist of layers of gas-filled detectors with spatial resolution to allow for reconstruction of muon tracks and hence momentum measurement. The necessary magnetic field for the momentum measurement will be provided by a toroid lying between the hadron calorimeter and the muon chambers. Options for the toroid are either a superconducting air-cored device or a conventional warm iron toroid. Detailed construction of the muon chambers themselves is also still to be decided.

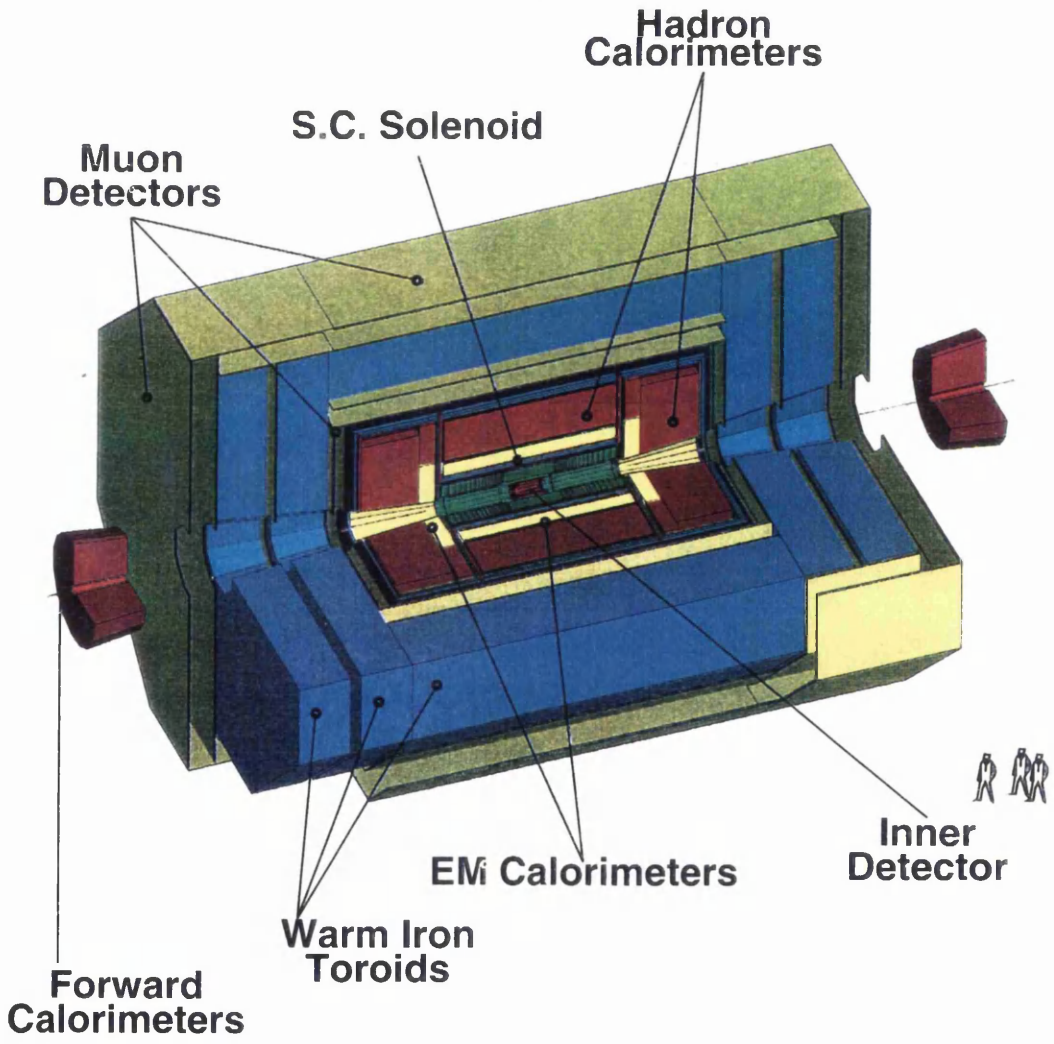

Figure 1.16: The ATLAS Detector (From [23])

1.5.4 The Search for the Higgs with ATLAS

The most likely process for Higgs production will be gluon-gluon fusion, although for a Higgs mass exceeding ~700 GeV, WW or ZZ fusion may begin to dominate, depending on the top quark mass. The lower the top mass, the more likely is the latter process to dominate [24]. It is of interest due to the signature provided by the two forward energetic quark jets. The decay processes of interest in order of increasing Higgs mass are [24] [12]:

i) $80GeV \leq M_H \leq 130GeV : \quad WH \longrightarrow l\nu\gamma\gamma$

This mass range is of interest because it bridges between the maximum mass limit attainable at LEP200 and the mass range likely to be probed at LHC. Statistics are expected to be poor due to the small branching ratio of the decay channel, and electron identification will be needed.

ii) $90GeV \leq M_H \leq 150GeV : \quad H \longrightarrow \gamma\gamma$

Again useful for probing the low end of the Higgs mass range, this channel requires excellent energy resolution for the γs in order to reject $\gamma\gamma$ events from QCD backgrounds. Vertex location must be precise.

iii) $130GeV \leq M_H \leq 2M_Z : \quad H \longrightarrow ZZ^* \longrightarrow 4l$

Statistics will be limited by the small branching ratio at either end of this mass range. Detector tracking acceptance is crucial for this channel (see Fig.1.17) [1].

iv) $2M_Z \leq M_H \leq 800GeV : \quad H \longrightarrow ZZ \longrightarrow 4l$

This channel requires fair ($\Delta p/p \sim 10\%$) muon chamber performance. The growth of the Higgs decay width at the upper end of this range is expected to make recognition more difficult.

[1] η is related to angle θ from the beam pipe by: $\eta = \frac{1}{2} \ln\left(\frac{1+\cos\theta}{1-\cos\theta}\right)$.

v) M_H up to $1TeV$: $H \longrightarrow ZZ$, $WW \longrightarrow l\nu$ 2 jets, $2l$ 2 jets, $2l$ 2ν

The channel decaying to $ll\nu\nu$ is difficult due to background processes, and requires calorimeter coverage to $\eta = 4$. The channels requiring jet tagging place even stricter requirements on the calorimeter coverage, which must extend beyond $\eta = 4.5$.

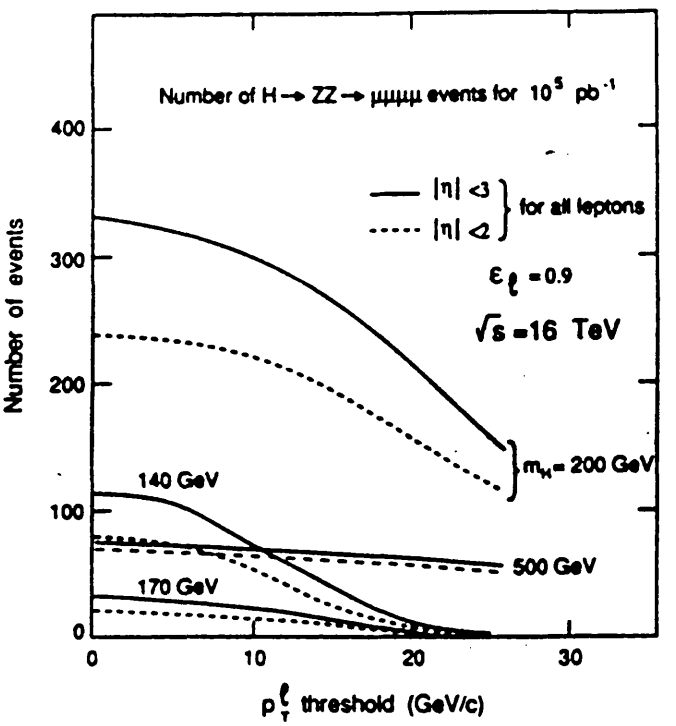

Figure 1.17: No. of Detected Higgs Events as a Function of Geometrical Acceptance Cuts (From [24])

The detailed structure of the ATLAS detector has been conceived in order to achieve coverage of each of these mass ranges. For example, the forward calorimeters will cover the region up to $\eta = 5$ in order to cover a maximum M_H of 1TeV. The forward region is one of the most difficult in terms of radiation hardness, so that devices based either on gas ionisation or liquid scintillation will be used in order to make replacement of the active material an easy matter.

Similar considerations apply for the inner detector, details of which are shown

in Fig.1.18. A polythene moderator will be used to reduce the flux of neutrons reaching the inner detector by an order of magnitude. The outer region of the inner detector will be composed of microstrip gas counters (MSGC) at $\eta > 1.5$, and silicon tracking detectors (SIT) or a combination of silicon tracking detectors and a transition radiation detector (TRD) will cover $\eta < 1.5$. The beam crossing rate and radiation hardness problems will preclude the use of silicon CCDs and drift chambers for tracking at LHC [25]. The region closest to the interaction point will be covered by a silicon tracker and vertex detector (SITV), up to $\eta = 1.8$, which will consist of a layer of silicon pixel detectors at 10cm radially from the beam pipe, surrounded by layers of double-sided silicon microstrips at 20cm and 30cm. Radiation dose due to charged particles is expected to be a problem particularly for the innermost layer, which has therefore been designed with easy replacement in mind.

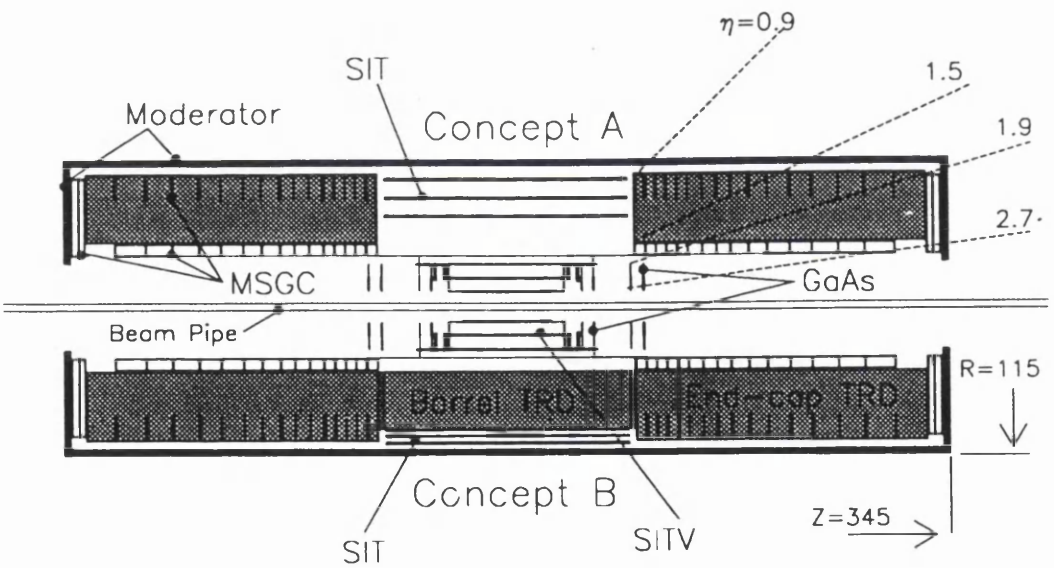

Figure 1.18: **ATLAS Inner Detector - Showing Two Possible Layouts (From [23])**

The use of semiconductor tracking detectors to cover the region from $\eta = 1.8$ upwards would be an advantage, especially for smaller M_H, when the muon momentum measurement from the inner detector will be used to supplement

that from the outer muon system. From Fig.1.17, it can be seen that increasing the η coverage from $\eta = 2$ to $\eta = 3$ is able to increase the Higgs detection rate by a factor of 50 % for $M_H = 200$ GeV; this factor increases with decreasing M_H. Fig.1.19 shows the improvement in momentum resolution which could be achieved by covering the same region with detectors of spatial resolution $20\mu m$, arranged in rings in the forward region.

The precise requirements for radiation hardness in this region will be discussed in the next chapter, but it is very unlikely that any silicon device would be able to survive here. Gallium arsenide semiconductor devices are known to be more radiation tolerant [28] than silicon; in addition, they are fast and the direct band gap of the material should lead to the opportunity of optical signal coupling. The RD8 Collaboration was formed with the intention of developing GaAs based detectors for tracking in those regions where silicon cannot be used due to radiation hardness problems.

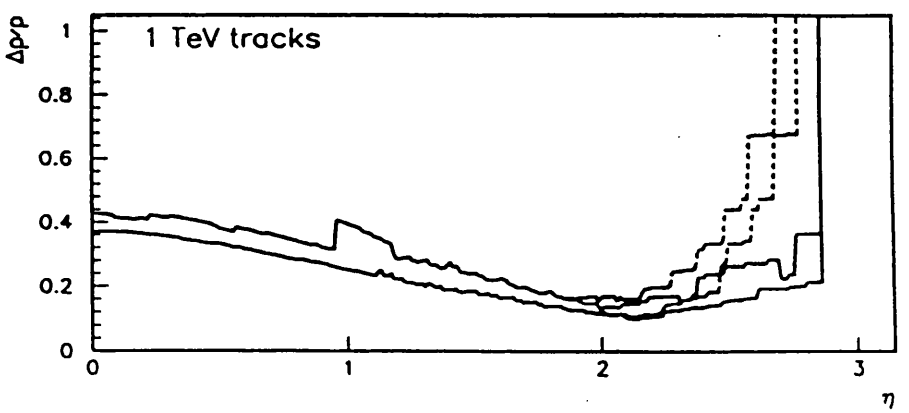

Figure 1.19: Improvement in Momentum Resolution due to GaAs Solid line: without GaAs Dotted line: with GaAs (From [22])

References

[1] MCKAY,K.G. *Physics Review 84 (1951) 829*

[2] SEYMOUR,J. *Electronic Devices and Components (Pitman)*

[3] KNOLL,G.F. *Radiation Detection and Measurement (Wiley)*

[4] MORGAN,D.V. and BOARD,K. *An Introduction to Semiconductor Microtechnology (Wiley)*

[5] ELLISON,J. *PhD Thesis, Imperial College (1987)*

[6] RADEKA,V. *Nuclear Instruments and Methods 226 (1984) 209*

[7] DAMERELL,C.J.S. *Techniques and Concepts of High Energy Physics IV (Plenum)*

[8] KEMMER,J. *Nuclear Instruments and Methods 169 (1980) 499*

[9] HOLL,P. et al *IEEE Transactions on Nuclear Science, Vol.36 No.1 (1989) 251*

[10] ALLPORT,P. et al *Nuclear Instruments and Methods 310 (1991) 155*

[11] AVSET,B. et al *CERN Preprint EP/90-11 Jan.23rd.1990*

[12] BATIGNANI,G. et al *Nuclear Instruments and Methods 326 (1993) 183*

[13] SITP Collaboration *Private Communication*

[14] THOMAS,S.L. and SELLER,P. *Nuclear Instruments and Methods 275 (1989) 564*

[15] SHAPIRO,S.L. et al *Nuclear Instruments and Methods 275 (1989) 580*

[16] SNOEYS,W. et al *Nuclear Instruments and Methods 326 (1993) 144*

[17] DAMERELL,C.J.S. et al *Nuclear Instruments and Methods 275 (1989) 484*

[18] GATTI,E. and REHAK,P. *Nuclear Instruments and Methods 225 (1984) 608*

[19] VACCHI,A. et al *Nuclear Instruments and Methods 306 (1991) 187*

[20] KANE,G. *Modern Elementary Particle Physics (Addison-Wesley)*

[21] RUBBIA,C. *LHC Workshop, Aachen (1990)*

[22] POPPLETON,A. et al *ATLAS Internal Note INDET-NO-001*

[23] ATLAS Collaboration *CERN/LHCC/92-4*

[24] DENEGRI,D. *LHC Workshop, Aachen (1990)*

[25] HEIJNE,E. and JARRON,P. *Nuclear Instruments and Methods 275 (1989) 467*

[26] GRIFFITHS,D. *Introduction to Elementary Particles (Wiley)*

[27] ALEPH Collaboration *Z. Phys. C.-Particles and Fields 53 1-20 (1992)*

[28] MESSENGER,G.C. and ASH,M.S. *The Effects of Radiation on Electronic Systems (VNR)*

Chapter 2

The Physics of Semiconductor Detectors

2.1 The Behaviour of Electrons in Crystals

2.1.1 Energy Bands-Qualitative Description

In order to understand the operation of a semiconductor detector, it is necessary to understand the behaviour of charge carriers in the crystal from which the device has been made.

In an isolated atom, quantum mechanics predicts that electrons will occupy states with discrete energies, between which solutions of the Schrodinger equation do not exist. Thus, transitions in energy of the electron amongst these states give rise to the discrete lines in the emission and absorption spectra of gases. If N such individual atoms are assembled together to form a crystal, the presence of each perturbs the energy level structure in the others; for sufficiently large N, the discrete levels of the isolated atoms become spread out into so-called energy bands. The distribution of available energy states is then continuous within a band, individual bands being separated by forbidden energy gaps.

2.1.2 Energy Levels and Density of States

The simplest model of the motion of electrons in a crystal is that of the free electron gas. Here, the atoms of the crystal are considered to be completely ionised, their valence electrons permeating the space about the ion cores, with which they do not interact. The behaviour of these electrons is described by quantum mechanics and the Pauli exclusion principle. For a free electron in a one dimensional crystal occupying the space 0 to L, the time-independent Schrodinger equation is [4]:

$$-\frac{\hbar^2}{2m}\frac{d^2\psi}{dx^2} = E\psi \tag{2.1}$$

This has solutions of the form:

$$\psi = A\cos kx + B\sin kx \quad \text{where} \quad k = \sqrt{\frac{2mE}{\hbar^2}} \tag{2.2}$$

In order to satisfy the boundary conditions that ψ is zero at $x = 0$ and $x = L$, A must be zero and k must be equal to $n\pi/L$. Thus, the required solution is:

$$\psi = B\sin\frac{n\pi x}{L} \tag{2.3}$$

Possible electron energies are then given by:

$$E = \frac{\hbar^2}{2m}\left(\frac{n\pi}{L}\right)^2 \tag{2.4}$$

For each value of the energy E of an electron state, the Pauli principle allows the accomodation of two electrons, with opposite spin orientations. Considering a crystal in its ground state (i.e. $T = 0K$), containing N free electrons, the highest occupied energy state is that for which $n = N/2$, which has energy:

$$E = \frac{\hbar^2}{2m}\left(\frac{N\pi}{2L}\right)^2 \tag{2.5}$$

This is known as the Fermi level, and is written as E_f. At absolute zero, all the available energy states up to the Fermi level are filled by electrons.

As temperature rises, some electrons may acquire sufficient thermal energy to populate higher states, leaving behind empty states at low energy. Away from

0K, the probability that a state at energy E is populated is given by the Fermi-Dirac function:

$$f(E) = \frac{1}{1 + exp^{(E - E_f)/k_BT}} \tag{2.6}$$

The form of this function is shown in Fig.2.1. The Fermi level is now that energy at which the probability of a state being occupied by an electron is 1/2. For conditions where $E - E_f > k_BT$, the 1 in the denominator may be neglected, and the Fermi-Dirac function may be approximated by a Maxwell-Boltzmann distribution.

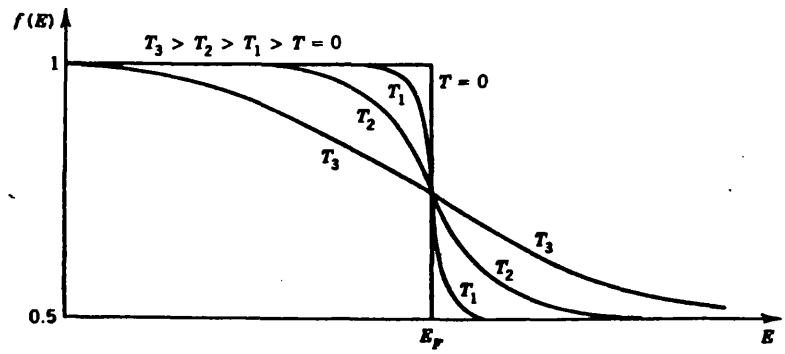

Figure 2.1: **The Fermi-Dirac Function (From [2])**

For a crystal in three dimensions, the time-independent Schrodinger equation becomes:

$$-\frac{\hbar^2}{2m}\nabla^2\psi(r) = E\psi(r) \tag{2.7}$$

Considering the crystal to be unbounded, the periodicity of the lattice may be imposed on the solutions to the above equation by demanding that they be periodic over some large distance L:

$$\psi(x, y, z) = \psi(x + L, y + L, z + L) \tag{2.8}$$

This requirement is satisfied by travelling wave solutions of the form:

$$\psi(r) = exp^{ik.r} \quad \text{where} \quad k = \frac{2n\pi}{L} \tag{2.9}$$

The energy of these solutions being given by:

$$E = \frac{\hbar^2}{2m}(k_x^2 + k_y^2 + k_z^2) \tag{2.10}$$

Each value of energy corresponds to some particular momentum value for an electron in that state; this momentum is given by the quantum mechanical operator $-i\hbar\nabla$ acting on the electron wavefunction $\psi(r)$. Thus:

$$p = -i\hbar\nabla\left(exp^{ik.r}\right) = \hbar k\psi(r) \tag{2.11}$$

The ground state of N electrons in the crystal may therefore be represented in momentum space as N/2 points filling a sphere up to that momentum which corresponds to the Fermi energy. Such a sphere will then have a radius of $k_f = \sqrt{\frac{2mE_f}{\hbar^2}}$. Since $k = \frac{2n\pi}{L}$, there is one electron state per $\left(\frac{2\pi}{L}\right)^3$ volume of momentum space, and so the total number of states in the sphere will be:

$$N = \left(\frac{4}{3}\pi k_f^3\right) \cdot \left(\frac{L^3}{8\pi^3}\right) \cdot 2 \tag{2.12}$$

By rearranging this in order to obtain k in terms of N, it is possible to calculate the Fermi level of a system containing N states:

$$E_f = \frac{\hbar^2}{2m}k_f^2 = \frac{\hbar^2}{2m}\left(\frac{N}{V} \cdot 3\pi^2\right)^{\frac{2}{3}} \tag{2.13}$$

By rearranging this to give N in terms of E, and differentiating with respect to E, the number of states available to an electron in an energy interval dE per unit crystal volume is given by :

$$D(E) \equiv \frac{dN}{dE} = \frac{m^{\frac{3}{2}}}{\hbar^3} \cdot \frac{\sqrt{2}}{\pi^2} \cdot E^{\frac{1}{2}} \tag{2.14}$$

$D(E)$ is termed the "density of states", and is important in determining the distribution of electrons in a crystal over the energy bands, the probability of an electron being found in a state at energy E being given by $P(E) = D(E) \cdot f(E)$.

2.1.3 The Origin of Energy Gaps - The Nearly Free Electron Model

In the free electron model, the wavefunctions $\psi(r) = exp^{ik.r}$ describe travelling wave solutions to the Schrodinger equation, with momentum $\hbar k$ and energies given by :

$$E_k = \frac{\hbar^2}{2m}(k_x^2 + k_y^2 + k_z^2) \quad \text{where} \quad k_x,\ k_y,\ k_z, = \frac{2n\pi}{L} \tag{2.15}$$

This describes a parabolic relation between E and k, where for any allowed value of k, there is a corresponding value for E which an electron in that particular state may have. There are no forbidden energy gaps. It is important that any model attempting to account for the behaviour of electrons in crystals describes the band gaps, as they determine the conduction properties of the material. The origin of energy gaps becomes clear when the potential due to the ion cores is allowed to perturb the behaviour of the electrons [4].

Considering a crystal of lattice spacing a, if such a crystal is illuminated with radiation of wavelength $\lambda << a$, diffraction of the incident beam into fringes is observed. The condition for a bright fringe to be observed is given by the Bragg law:

$$2a \sin\theta = n\lambda \tag{2.16}$$

It is Bragg reflection of travelling electron waves within a crystal which causes the existence of the band gap. Consider an electron wave propagating through a crystal at normal incidence to the crystal planes; if its wavelength satisfies $\lambda = \frac{2a}{n}$, it will suffer repeated strong reflections; the only reasonable solution to the time independent Schrodinger equation for such a mode must be a standing wave.

Such a standing wave may be formed from the superposition of the two travelling

waves, $exp^{\frac{i\pi x}{a}}$ and $exp^{\frac{-i\pi x}{a}}$. These can be superimposed in two ways:

$$\psi(+) \quad = \quad exp^{\frac{i\pi x}{a}} + exp^{\frac{-i\pi x}{a}} \quad = \quad 2\cos\left(\frac{\pi x}{a}\right) \tag{2.17}$$

$$\psi(-) \quad = \quad exp^{\frac{i\pi x}{a}} - exp^{\frac{-i\pi x}{a}} \quad = \quad 2i\sin\left(\frac{\pi x}{a}\right) \tag{2.18}$$

Now, considering where an electron is likely to be found in the crystal, for the travelling wave case, the electron probability density is:

$$\rho \quad = \quad |\psi^*\psi| \quad = \quad exp^{\frac{i\pi x}{a}} \,.\, exp^{\frac{-i\pi x}{a}} \quad = \quad 1 \tag{2.19}$$

Similarly, for $\psi(+)$, $\rho(+) \sim \cos^2\left(\frac{\pi x}{a}\right)$, and for $\psi(-)$, $\rho(-) \sim \sin^2\left(\frac{\pi x}{a}\right)$. Thus, an electron described by the travelling wave solution is equally likely to be found anywhere in the crystal. An electron described by $\psi(-)$ is most likely to be found at the points $x = (n + \frac{1}{2})a$, and an electron described by $\psi(+)$ is most likely to be found at the points $x = na$, where n is an integer. So $\psi(+)$ describes a standing wave distribution with electrons accumulated close to the ion cores, whilst $\psi(-)$ describes the situation where the electrons are accumulated mid-way between the ion cores. Clearly, the potential energy due to the interaction between the ions and the electrons will be greater in the latter case. For the point in momentum space where $\lambda = \frac{2a}{n}$, i.e. $k = \frac{n\pi}{a}$, then, travelling wave solutions are forbidden over an energy range of:

$$E \quad = \quad \text{potential energy of } \psi(+) \quad - \quad \text{potential energy of } \psi(-) \tag{2.20}$$

This is the band gap energy, written as E_g. Diagrams of E versus k for the free electron and nearly free electron models are shown in Fig.2.2. The value of E_g is $1.12eV$ for silicon and $1.42eV$ for gallium arsenide.

2.1.4 The Distribution of Carriers over the Bands

The behaviour of semiconductor devices is governed by the availability of carriers for conduction, which requires that there be partly filled bands. For the case of

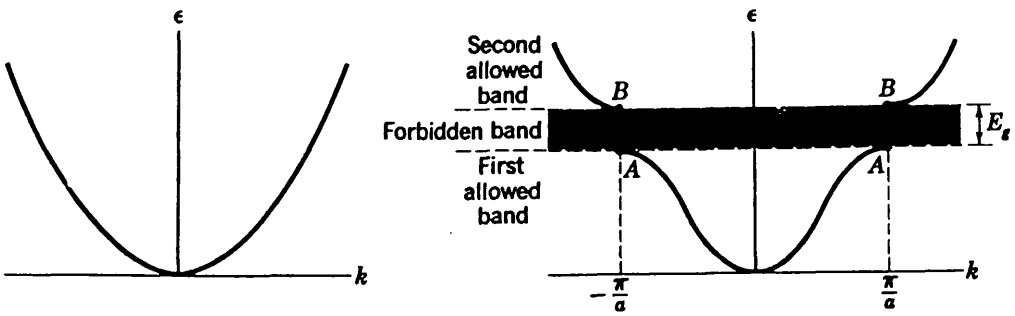

Figure 2.2: E vs. k from the Free Electron (left) and Nearly Free Electron (right) Models. (From [4])

a conduction band and a valence band separated by energy E_g, the density of states:

$$N(E) = \frac{m^{\frac{3}{2}}}{h^3} \cdot \frac{\sqrt{2}}{\pi^2} \cdot E^{\frac{1}{2}} \tag{2.21}$$

may be applied [6] by taking the kinetic energy of an electron as zero at the bottom of the conduction band (E_c) and increasing upwards on the energy band diagram, whilst the kinetic energy of a hole is taken to be zero at the top of the valence band (E_v) and increases downwards. Thus, for electrons:

$$N(E) = \frac{m_e^{\frac{3}{2}}}{h^3} \cdot \frac{\sqrt{2}}{\pi^2} \cdot (E - E_c)^{\frac{1}{2}} \tag{2.22}$$

and for holes:

$$N(E) = \frac{m_h^{\frac{3}{2}}}{h^3} \cdot \frac{\sqrt{2}}{\pi^2} \cdot (E_v - E)^{\frac{1}{2}} \tag{2.23}$$

For both electrons and holes, the probability of a state being occupied is given by the Fermi function; the probability of a state in the valence band being occupied by a hole is just that of it not being occupied by an electron. For electrons:

$$P_{e^-}(E) = F(E) = \frac{1}{1 + exp^{\frac{E-E_f}{kT}}} \approx exp^{\frac{-(E-E_f)}{kT}} \tag{2.24}$$

For holes:

$$P_{h+}(E) = 1 - F(E) = 1 - \frac{1}{1 + exp^{\frac{E-E_f}{kT}}} \approx exp^{\frac{-(E_f-E)}{kT}} \quad (2.25)$$

Thus, the distribution of carriers over the bands can be found, the number of electrons in the conduction band per unit volume of the crystal being:

$$n = \int_0^\infty N(E)\, F(E)\, dE \quad (2.26)$$

Where the integral has been taken from zero to infinity, since as $E \rightarrow \infty$, $F(E) \rightarrow 0$.

$$\Rightarrow \quad n = \int_0^\infty \frac{m_e^{\frac{3}{2}}}{h^3} \frac{\sqrt{2}}{\pi^2} E^{\frac{1}{2}}\, exp^{\frac{-(E-E_f)}{kT}}\, dE \quad (2.27)$$

$$\Rightarrow \quad n = 2\left(\frac{m_e kT}{2\pi h^2}\right)^{\frac{3}{2}} exp^{\frac{E_f}{kT}} \quad (2.28)$$

Since the zero of energy has been taken as E_c:

$$n = N_c\, exp^{\frac{-(E_c-E_f)}{kT}} \text{ where } N_c = 2\left(\frac{m_e kT}{2\pi h^2}\right)^{\frac{3}{2}} \quad (2.29)$$

Thus, it is as if the conduction band were replaced by a single level at E_c, with an effective density of states N_c. For a hole in the valence band, a similar calculation gives:

$$p = N_v\, exp^{\frac{-(E_f-E_v)}{kT}} \text{ where } N_v = 2\left(\frac{m_h kT}{2\pi h^2}\right)^{\frac{3}{2}} \quad (2.30)$$

This applies to any semiconductor with doping concentration such that the Fermi level lies within the band gap. The distribution of the carriers over the bands in an n-type semiconductor at room temperature is shown in Fig.2.3.

For a doped material, the number of extra electrons in the conduction band will be equal to the number of ionised donor atoms, which is equal to the total number of donors minus the number of unionised donors. The number of unionised donors may be calculated, since the probability of finding an electron on a donor is the

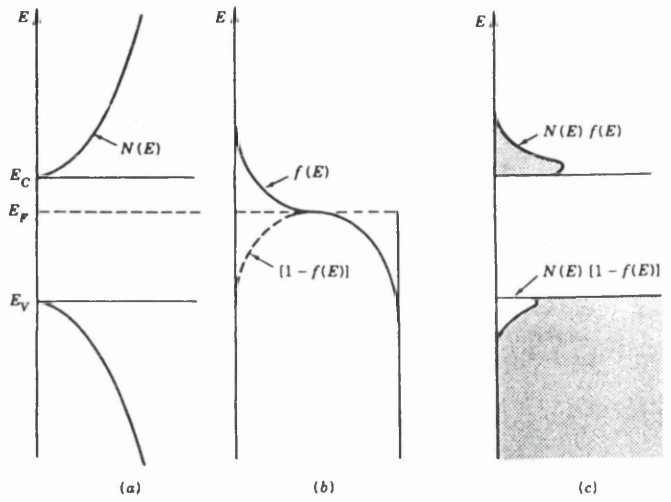

Figure 2.3: a) **Density of States. b) Distribution Functions of Electrons and Holes. c) Carrier Concentrations Within the Bands. (From [2])**

number of donor atoms multiplied by the probability of any one electron having the donor level energy. Thus, the number of electrons on the donors is:

$$n_d = N_d \, exp^{\frac{-(E_d - E_f)}{kT}} \tag{2.31}$$

where N_d is the number density of donor atoms. Similarly, the number of holes on the acceptors is given by:

$$p_a = N_a \, exp^{\frac{-(E_f - E_a)}{kT}} \tag{2.32}$$

where N_a is the number density of acceptor atoms. Thus, the total number of negative charges in a doped semiconductor will be $n + (N_a - p_a)$, whilst the total number of positive charges will be $p + (N_d - n_d)$. Since an accumulation of charge in any particular region of a semiconductor in equilibrium would not be expected, the charge neutrality condition must hold:

$$n + (N_a - p_a) = p + (N_d - n_d) \tag{2.33}$$

In a doped material, the Fermi level will be shifted from the position at which it lies in the intrinsic material. Denoting the intrinsic Fermi level by E_i, (2.29) and

(2.30) become:

$$n_i = N_c\, exp^{\frac{-(E_c-E_i)}{kT}} \quad \text{and} \quad p_i = N_v\, exp^{\frac{-(E_i-E_v)}{kT}} \tag{2.34}$$

combining this with (2.29) and (2.30) leads to:

$$n = n_i\, exp^{\frac{(E_f-E_i)}{kT}} \quad \text{and} \quad p = n_i\, exp^{\frac{(E_i-E_f)}{kT}} \tag{2.35}$$

whence it can be seen that, in equilibrium conditions, for any doping type, that $pn = n_i^2$.

2.1.5 Carrier Transport Properties of Semiconductors

Having found the distribution of charge carriers over the bands, their transport properties may be used in explaining the behaviour of devices [1],[6].

Drift Mobility. This is defined according to:

$$|v| = \mu|\epsilon_{ext}| \tag{2.36}$$

where v is the velocity of the carriers moving under the influence of an applied electric field ϵ_{ext}. Electrons and holes move in opposite directions due to their opposite charge, and in general have different mobilities. This expression predicts a linear rise of carrier velocity with field, which does not take into account velocity limiting phenomena such as scattering of the carriers. In reality, the carrier velocity will tail off to some asymptotic value v_{sat} at high fields. The carrier mobilities for silicon and gallium arsenide are shown in Fig.2.4.

Conductivity. The conductivity of a material is proportional to the mobility of the charge carriers therein. Current density is $J_n = nev_n$ for electrons, and $J_p = pev_p$ for holes. Thus, the total conductivity due to carriers of both signs is:

$$\sigma_{total} = ne\mu_n + pe\mu_p \tag{2.37}$$

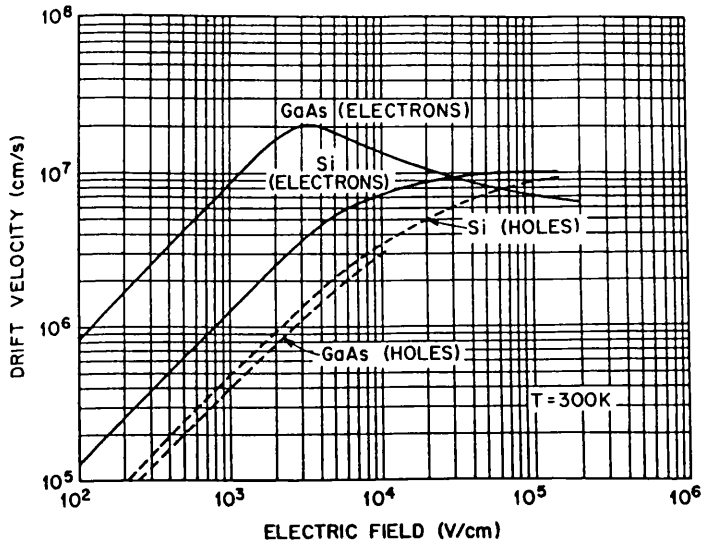

Figure 2.4: **Drift Velocity vs. Electric Field for Si and GaAs (From [1])**

Carrier Diffusion. In general, a current through a semiconductor will be composed of two currents, that due to carrier drift under the influence of an external field, and that due to diffusion. Fick's Law states that diffusion flux is proportional to concentration gradient, since, if there exists a higher concentration of carriers in some region, they will tend to diffuse away. The current density due to a certain flux of carriers is simply the flux multiplied by the charge per carrier. Thus, for electrons in one dimension:

$$J_n = e \cdot D_n \frac{dn}{dx} \tag{2.38}$$

Similarly, for holes:

$$J_p = -e \cdot D_p \frac{dp}{dx} \tag{2.39}$$

where D_n and D_p are the diffusion coefficients for electrons and holes respectively.

Einstein Relation between Diffusion Coefficient and Mobility. If it is easy for carriers to drift in a material under the influence of an applied field, it is reasonable to suppose that it will be easy for them to diffuse under the influence of thermal excitation in that material. If at some point in a crystal, there exists a higher concentration of electrons than elsewhere, they will diffuse away. The resulting

motion of the charges will create a field opposing further diffusion, in accordance with Le Chatelier's Principle. In equilibrium, then, the tendency to drift and to diffuse will balance. Thus:

$$J_{drift} = J_{diff} \quad \Rightarrow \quad en\mu_n\epsilon_x = eD_n\frac{dn}{dx} \tag{2.40}$$

If the concentration gradient is described by the Maxwell-Boltzmann distribution $n = n_0 exp^{\frac{eV}{kT}}$, then it is found that the mobility is related to the diffusion coefficient by the Einstein relation:

$$\mu_n = \frac{e}{kT}D_n \quad \text{for electrons, and} \quad \mu_p = \frac{e}{kT}D_p \quad \text{for holes.} \tag{2.41}$$

2.2 Contacts Between Materials

2.2.1 P-N Junction Current-Voltage Characteristic

Junction with no applied bias

Consider a p-n junction formed by bringing together a sample of p-type material and a sample of n-type material, as described in Chapter 1 (Fig.2.5).

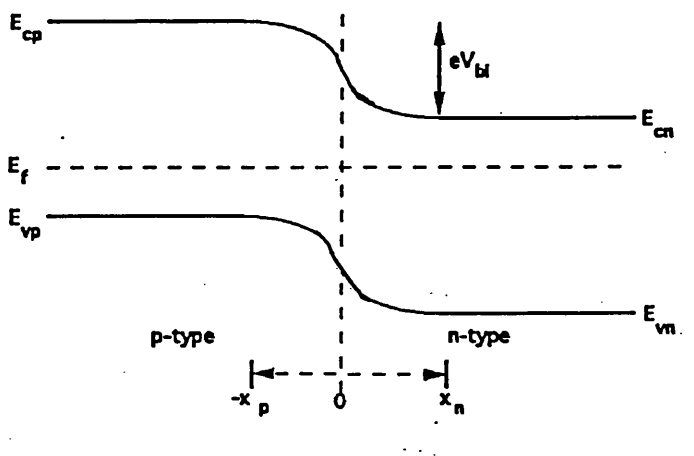

Figure 2.5: Energy-Band Diagram of P-N Junction

The conduction electron concentration on the n-side will be given by [3]:

$$n_n = N_c exp^{\frac{-(E_{cn}-E_f)}{kT}} \tag{2.42}$$

where E_{cn} is the energy level of the conduction band on the n-side. The electron concentration on the p-side will be:

$$n_p = N_c exp^{\frac{-(E_{cp}-E_f)}{kT}} \tag{2.43}$$

where E_{cp} is the energy level of the conduction band on the p-side. The electron concentrations on the two sides of the junction are related by:

$$n_{po} = n_{no} exp^{\frac{-(E_{cp}-E_{cn})}{kT}} = n_{no} exp^{\frac{-eV_{bi}}{kT}} \tag{2.44}$$

where the additional subscript "o" has been used to denote equilibrium.

Junction Under Forward Bias

Under forward bias V_{app}, the concentration of electrons on the n-side becomes:

$$n_p = n_n exp^{\frac{-e(V_{bi}-V_{app})}{kT}} = n_{po} exp^{\frac{eV_{app}}{kT}} \quad (2.45)$$

Thus, on the p-side, there is an excess of electrons equal to $(n_p - n_{po})$, which diffuses away across the junction, recombining. The same situation occurs for holes on the n-side of the junction. Current is thus carried by minority carriers close to the junction. The excess of electrons is given explicitly by:

$$n_p - n_{po} = n_{po}[exp^{\frac{eV_{app}}{kT}} - 1] \quad (2.46)$$

If the concentration profile of an excess of electrons diffusing away is described in terms of the diffusion length for electrons L_n by the exponential decay $\delta n(x) = \delta n(0)\ exp^{-\frac{x}{L_n}}$, then the current density across the junction due to diffusion will be:

$$J_{diff} = eD_n \frac{dn}{dx} = \frac{eD_n}{L_n}\ \delta n(0) exp^{-\frac{x}{L_n}} \quad (2.47)$$

$$= \frac{eD_n}{L_n} exp^{-\frac{x}{L_n}} \cdot (n_p - n_{po}) \quad (2.48)$$

$$= \frac{eD_n}{L_n} exp^{-\frac{x}{L_n}} \cdot (exp^{\frac{eV_{app}}{kT}} - 1) \quad (2.49)$$

If L_n exceeds the depletion region width W, then the first exponential term tends to unity. Thus we have:

$$J_{diff} = e\left[\frac{D_n n_{po}}{L_n} + \frac{D_p p_{no}}{L_p}\right] \cdot (exp^{\frac{eV_{app}}{kT}} - 1) \quad (2.50)$$

which predicts the typical diode current-voltage characteristic (Fig.2.6):

$$I = I_0(exp^{\frac{eV_{app}}{kT}} - 1) \quad (2.51)$$

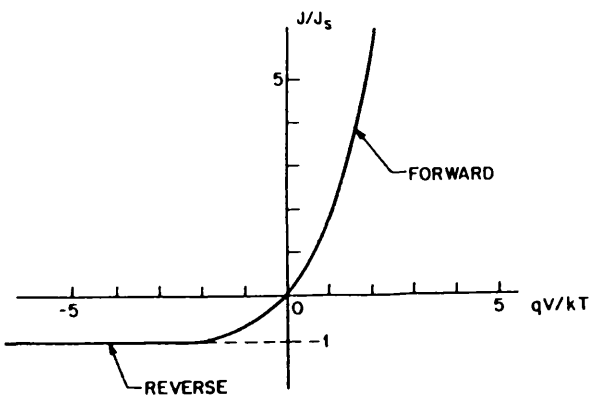

Figure 2.6: P-N Junction Current-Voltage Characteristic (From [1])

2.2.2 Schottky Contact Current-Voltage Characteristic

For Schottky barrier contacts on Si and GaAs, the dominant mechanism of electron transport over the barrier is due to thermionic emission; an electron will be able to cross from the semiconductor to the metal if it acquires sufficient thermal energy to reach the top of the barrier. Consider the metal-semiconductor rectifying contact shown in Fig.2.7 [2].

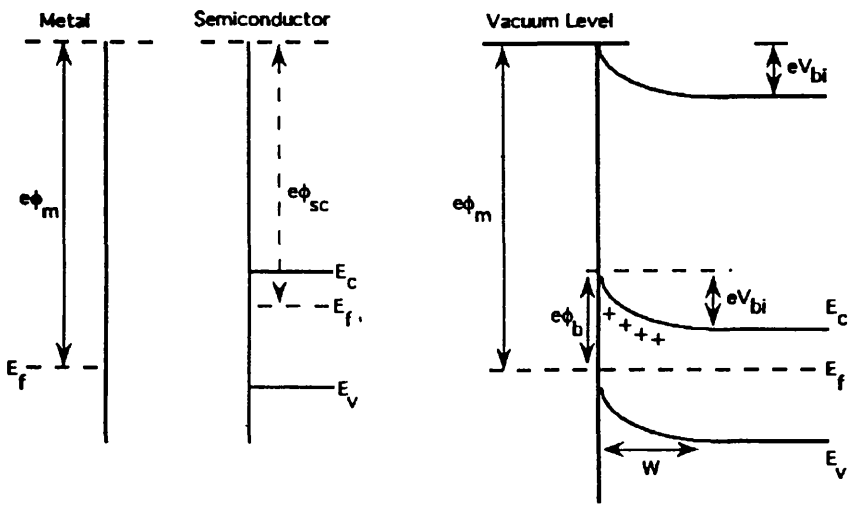

Figure 2.7: Schottky Contact Formation

The barrier energy will be:

$$e\Phi_b \quad = \quad e(\phi_m - \phi_{sc}) \quad = \quad eV_{bi} + (E_c - E_f) \tag{2.52}$$

Assuming that eV_{bi} is sufficiently large with respect to kT, so that Maxwell-Boltzmann statistics may be used, the number of electrons per unit volume with sufficient energy to surmount the barrier will be:

$$n_b \quad = \quad n_{sc} exp^{-e\frac{(V_{bi} - V_{app})}{kT}} \tag{2.53}$$

where n_{sc} is the electron concentration at the bottom of the conduction band in the bulk semiconductor. Substituting for n_{sc} from (2.29) and for $(E_c - E_f)$ from above:

$$n_b \quad = \quad N_c exp^{-e\frac{(\Phi_b - V_{app})}{kT}} \tag{2.54}$$

Assuming that all those electrons which reach the top of the barrier from the semiconductor side pass into the metal, the flux of electrons over the barrier will be $\frac{n\bar{c}}{4}$, where $\bar{c}$ is their mean velocity. The current density from the metal to the semiconductor will then be:

$$J_{m \to sc} \quad = \quad e\frac{n\bar{c}}{4} N_c exp^{-e\frac{(\Phi_b - V_{app})}{kT}} \tag{2.55}$$

If no bias voltage is applied, with the contact at equilibrium, the current must be the same in both directions:

$$J_{m \to sc} \quad = \quad J_{sc \to m} \quad = \quad e\frac{n\bar{c}}{4} N_c exp^{-e\frac{\Phi_b}{kT}} \tag{2.56}$$

Now an electron moving from the metal to the semiconductor will always see the same barrier height $e\Phi_b$. When a bias voltage is applied, the net current density is:

$$J_{m \to sc} \quad = \quad e\frac{n\bar{c}}{4} N_c exp^{-e\frac{\Phi_b}{kT}} \left(exp^{e\frac{V_{app}}{kT}} - 1 \right) \tag{2.57}$$

which predicts a current-voltage characteristic of:

$$I \quad = \quad I_0 \left(exp^{e\frac{V_{app}}{kT}} - 1 \right) \tag{2.58}$$

which is of the same form as that of a p-n junction. Now, I_0 may be written as:

$$I_0 = AR^*T^2 exp^{-e\frac{\Phi_b}{kT}} \tag{2.59}$$

where R^* is the Richardson constant for the emission of electrons from the metal into the semiconductor. Substituting for N_c from equation (2. 29) and for $\bar{c}$ from the mean velocity for a Maxwellian velocity distribution [5] , namely $\bar{c} = \left(\frac{8kT}{\pi m_e^*}\right)^{\frac{1}{2}}$, R^* is given by:

$$R^* = \frac{4\pi m_e^* e k^2}{h^3} \tag{2.60}$$

2.2.3 Field and Potential in Rectifying Junctions

The Field Distribution

The field distribution within a p-n junction may be found by solving the Poisson equation. This is most simply done subject to the assumptions that all donor and acceptor atoms in the material are ionised, that there are no free carriers within the depletion region, and that the total change in potential across the junction occurs over the depletion region alone. Then for the depletion region on the p-side, the charge density will be $-eN_a$, whilst that on the n-side will be eN_d. From Fig.2.5, taking the origin at the interface and the depletion regions extending to $-x_p$ and x_n, the Poisson equation becomes on the p-side:

$$\frac{\partial^2 V}{\partial x^2} = \frac{eN_a}{\epsilon_0 \epsilon_r} \quad \text{for} \quad -x_p \leq x < 0 \tag{2.61}$$

Integrating once with respect to x, subject to the boundary condition that the field must be zero at the edge of the depletion region on the p-side, the field within the p-side is given by:

$$\mathcal{E}(x) = -\frac{\partial V}{\partial x} = -\frac{eN_a}{\epsilon_0 \epsilon_r} \cdot (x_p + x) \tag{2.62}$$

It can be seen that the maximum value of the field occurs at $x = 0$, and has the value:

$$\mathcal{E}_{max} = -\frac{eN_a}{\epsilon_0 \epsilon_r} \cdot (x_p) \tag{2.63}$$

For the n-side, the Poisson equation is:

$$\frac{\partial^2 V}{\partial x^2} = -\frac{eN_d}{\epsilon_0 \epsilon_r} \quad \text{for} \quad 0 \leq x < x_n \tag{2.64}$$

Solving this subject to the boundary condition that the field is zero at the edge of the depletion region on the n-side, the field within the n-side is given by:

$$\mathcal{E}(x) = -\frac{\partial V}{\partial x} = \frac{eN_d}{\epsilon_0 \epsilon_r} \cdot (x - x_n) \tag{2.65}$$

$$\text{where} \quad \mathcal{E}_{max} = -\frac{eN_d}{\epsilon_0 \epsilon_r} \cdot (x_n) \quad \text{at} \quad x = 0 \tag{2.66}$$

The field must be continuous at $x = 0$, thus the combination of (2.63) with (2.66) yields:

$$N_d \, x_n = N_a \, x_p \tag{2.67}$$

For a Schottky barrier diode on n-type material, the field within the metal is zero. If the depletion depth is denoted by W, (2.65) becomes modified to give:

$$\mathcal{E}(x) = \frac{eN_d}{\epsilon_0 \epsilon_r} \cdot (x - W) \tag{2.68}$$

$$\text{where} \quad \mathcal{E}_{max} = -\frac{eN_d}{\epsilon_0 \epsilon_r} \cdot (W) \quad \text{at} \quad x = 0 \tag{2.69}$$

The Potential Distribution

The potential distribution across the junction $V(x)$ may be found by integrating the field with respect to x over the two regions. For the p-side, integration of (2.62) yields:

$$V(x) = \frac{eN_a}{\epsilon_0 \epsilon_r} \cdot \left(\frac{x^2}{2} + x_p x\right) \tag{2.70}$$

whilst for the n-side, integration of (2.65) gives:

$$V(x) = -\frac{eN_d}{\epsilon_0 \epsilon_r} \cdot \left(\frac{x^2}{2} - x_n x\right) \tag{2.71}$$

If (2.70) is evaluated between the limits $x = -x_p$ and $x = 0$, (2.71) is evaluated between the limits $x = 0$ and $x = x_n$, and the two results summed, the total potential drop across the junction is:

$$V = \frac{eN_a}{\epsilon_0 \epsilon_r} \frac{x_p^2}{2} + \frac{eN_d}{\epsilon_0 \epsilon_r} \frac{x_n^2}{2} \tag{2.72}$$

For a $p^+ - n$ junction of the type commonly used for the manufacture of detectors, N_a is very large compared to N_d. Thus, the depletion depth on the p^+ side of the contact is small, and may be neglected. For a Schottky contact, there is no depletion region on the metal side of the junction. In either case, if $V = V_{bi} + V_{app}$, where V_{app} is an applied reverse bias voltage, the depletion depth W is given by (2.72) as:

$$W = \sqrt{\frac{2\epsilon_0\epsilon_r}{eN_d} \cdot (V_{bi} + V_{app})} \tag{2.73}$$

Thus, it can be seen that to obtain full depletion of the thick detectors required for minimum ionising particles at reasonable reverse bias voltages, hyper-pure semiconductor materials with low dopant concentrations must be used. The charge, field and potential distributions for a $p^+ - n$ junction are shown in Fig.2.8.

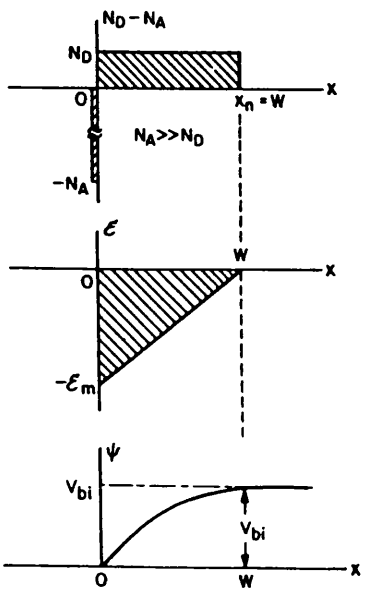

Figure 2.8: **Abrupt Junction: a) Charge Distribution b) Field Distribution c) Potential Distribution (From [1])**

2.2.4 Capacitance of p^+-n and Schottky Junctions

In any system involving a detector and charge preamplifier, the noise of the system increases with the capacitance of the detector, which will vary with the depletion

depth W of the detector. The capacitance will be given by:

$$C \equiv \frac{dQ}{dV} = \frac{dQ}{dW} \cdot \frac{dW}{dV} \tag{2.74}$$

For a device of cross sectional area A, the charge within an element dW of the depletion region is:

$$dQ = e\, N_d\, A\, dW \tag{2.75}$$

Then, differentiating (2.73) to give $\frac{dW}{dV}$, the capacitance of the junction is obtained:

$$C = A \sqrt{\frac{\epsilon_0 \epsilon_r e N_d}{2}} \cdot (V_{bi} + V_{app})^{\frac{-1}{2}} \tag{2.76}$$

2.2.5 Breakdown in Semiconductor Junctions

At large reverse bias voltages, a rectifying junction may break down, leading to a large increase in reverse current. There are two processes which contribute to this current, namely Zener breakdown and avalanche breakdown. Avalanche breakdown is the process which limits the voltage which can be applied across a detector.

Considering a typical p^+-n structure in reverse bias, for avalanche breakdown to occur, an electron must first be thermally excited across the band gap. Once in the conduction band, if the field is sufficiently high, it may gain enough energy to disrupt bonds in the crystal by collision with its constituent atoms. For such a broken bond, one electron will reach the conduction band and one hole will reach the valence band. These are in turn accelerated by the field, causing further ionisation. Thus, the number of carriers present within an element dx at distance x across the depletion region will increase exponentially with x, and a large breakdown current will flow. Hence, breakdown will occur if the field within the device at any point exceeds some critical value for the semiconductor. The breakdown voltages of silicon and gallium arsenide abrupt junctions have been

shown [7] to follow approximately the empirical relation:

$$V_{bd} = 60\ (E_g/1.1)^{3/2}\ .\ (N_d/10^{16})^{-3/4} \tag{2.77}$$

This should be considered as an approximate upper limit only.

2.3 Noise in Semiconductor Detectors

2.3.1 Sources of Noise

It has already been stated that the detector capacitance affects the noise generated within the chain of detector and preamplifier; here the problem is one of optimising the preamplifier to match a particular detector.

There are two sources of noise within the detector itself, the first being due to thermal diffusion of electrons within the resistances associated with the detector, and the second being due to its reverse leakage current. Thus, there is a thermal noise voltage due to the series resistance of the contacts of the detector and a thermal noise voltage due to the resistance of the bulk material which constitutes the detector.

The leakage current itself is nominally a steady value, and so does not make a direct contribution to the noise of the detector; rather it is the shot noise associated with the flow of the discrete charge carriers constituting the leakage current which leads to current fluctuations through the device. These fluctuations may be represented by a current source in parallel with the detector, of magnitude:

$$i_{noise} = \sqrt{2\ I_L\ e\ \Delta f} \tag{2.78}$$

where Δf is the bandwidth of the system and I_L is the detector leakage current.

In a properly designed and constructed detector and readout chain, the contribution of thermal noise in resistances is small [8]. However, the the leakage current

in a real device is usually considerably larger than the value predicted for an ideal situation by equation 2.50 for a p-n junction or equations 2.57 and 2.58 for a Schottky contact. It is this noise source which dominates in the performance of semiconductor detectors.

2.3.2 Sources of Leakage Current

There are three sources of leakage current within a p-n junction; generation of free carriers in the undepleted material which subsequently diffuse into the depletion region and are swept away by the field, generation of carriers by crystal defects in the bulk material within the depletion region, and generation at the surface of the material due to surface states.

The first of these, diffusion current, should be negligible for a detector, which is operated in an essentially fully depleted mode; it will not be examined further.

The magnitude of the second may be calculated as follows [14]. Consider a material with crystal defects manifesting themselves by energy levels near the centre of the band gap (deep level defects). Assume that each defect has associated with it only one energy level. Four processes may occur at such a centre; an electron may be captured from the conduction band or a hole may be captured from the valence band, or an electron or hole may be released to the conduction or valence band, respectively (see Fig.2.9).
For an efficient generation-recombination centre, the capture of an electron must be followed by the capture of a hole; both events must have equal probability, and levels near the centre of the band gap will dominate. Let there be N_t such centres at energy E_t. The probability that such a level will be occupied by an electron is:

$$P(E_t) = \frac{1}{1 + exp^{\frac{(E_t - E_f)}{kT}}} \equiv f \qquad (2.79)$$

The rate of electron capture, R_{nc}, will be proportional to the number per unit volume of centres not occupied by an electron, $(1 - f)N_t$, the number of electrons

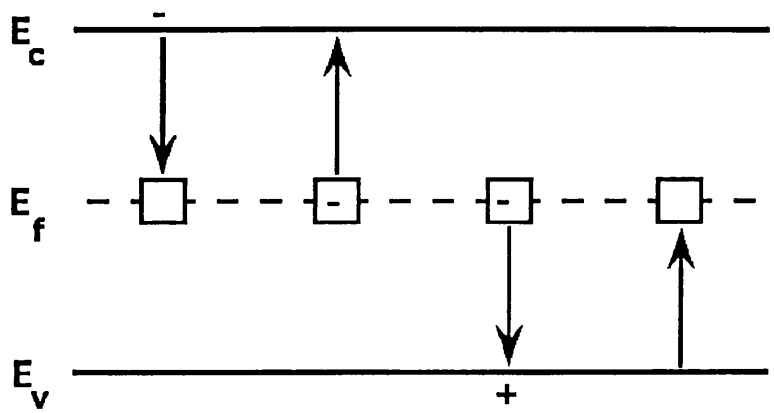

Figure 2.9: **Generation-Recombination Processes**

per unit volume, and their thermal velocity:

$$R_{nc} = \sigma_n n v_{th}(1 - f)N_t \tag{2.80}$$

where σ_n is the trap cross-section for electron capture. The rate of electron emission to the conduction band, R_{ne}, will be proportional to the number per unit volume of centres occupied by an electron, fN_t:

$$R_{ne} = \xi_n f N_t \tag{2.81}$$

where ξ_n is the electron emission probability. Similarly, for holes, the rates of hole capture and emission are respectively:

$$R_{pc} = \sigma_p p v_{th} f N_t \quad \text{and} \quad R_{pe} = \xi_p(1 - f)N_t \tag{2.82}$$

The rate of capture of carriers of either sign must be equal to the rate of emission for carriers of that sign; thus, the emission probability may be obtained from the trap cross section. Then:

$$\xi_n = \sigma_n n v_{th}\frac{(1 - f)}{f} \quad \text{and} \quad \xi_p = \sigma_p p v_{th}\frac{f}{(1 - f)} \tag{2.83}$$

Now, substituting directly for f and substituting from (2.35) for n and p: the electron and hole emission probabilities become explicitly:

$$\xi_n = \sigma_n v_{th} n_i exp^{\frac{(E_t - E_i)}{kT}} \quad \text{and} \quad \xi_p = \sigma_p v_{th} n_i exp^{\frac{(E_i - E_t)}{kT}} \tag{2.84}$$

Now, considering the introduction of electron-hole pairs at a steady rate of g per unit volume per second, the increase of carriers in the bands will lead to an increase in the capture rates:

$$R_{nc} = g + R_{ne} \quad \text{and} \quad R_{pc} = g + R_{pe} \tag{2.85}$$

Then, the recombination rate of the excess carriers will be, at the new equilibrium:

$$U = R_{nc} - R_{ne} = R_{pc} - R_{pe} \tag{2.86}$$

In order to calculate the overall rate of recombination from the individual process rates, the fact must be taken into account that the probability f of a defect centre being occupied by an electron will have changed. Substituting the expressions for the rates of capture and emission of electrons and holes into (2.87), the new occupation probability will be:

$$f = \frac{\sigma_n n + \sigma_p p_1}{\sigma_n(n + n_1) + \sigma_p(p + p_1)} \tag{2.87}$$

Then, calculating the recombination rate for electrons as $U = R_{nc} - R_{ne}$ using this new value of f:

$$U = \frac{\sigma_n \sigma_p v_{th} N_t (np - n_i^2)}{\sigma_n(n + n_1) + \sigma_p(p + p_1)} \tag{2.88}$$

where $n_1 = n_i exp[(E_t - E_i)/kT]$ and $p_1 = n_i exp[(E_i - E_t)/kT]$. This may be re-expressed in terms of the carrier lifetimes $\tau_{po} = \frac{1}{\sigma_p v_{th} N_t}$ and $\tau_{no} = \frac{1}{\sigma_n v_{th} N_t}$ to give:

$$U = \frac{(np - n_i^2)}{\tau_{po}(n + n_1) + \tau_{no}(p + p_1)} \tag{2.89}$$

With a forward bias V_{app} across the junction, the pn product is $pn = n_i^2 exp^{\frac{eV_{app}}{kT}}$, and the rate of recombination becomes:

$$U = \frac{n_i^2(exp^{\frac{eV_{app}}{kT}} - 1)}{\tau_{po}(n + n_1) + \tau_{no}(p + p_1)} \tag{2.90}$$

Considering the application of a sufficiently high reverse bias, the exponential term will vanish, as will the equilibrium carrier concentrations n and p in the

depletion region. Then:

$$U = \frac{-n_i^2}{\tau_{no} p_1 + \tau_{po} n_1} \tag{2.91}$$

This predicts a negative recombination rate - i.e. a net rate of generation within the depletion region. If the electron and hole lifetimes are equal, this may be simplified. Thus, taking $\tau_{no} = \tau_{po} = \tau_o$, and further assuming that the trap energy E_t is at the intrinsic Fermi level E_i, as is necessary for an efficient generation-recomination centre, so that $n_1 = p_1 = n_i$, the generation rate becomes:

$$U = \frac{-n_i}{2\tau_0} \tag{2.92}$$

The total generation current density in the depletion region will be given by the integral of this across the depletion region width, multiplied by the charge on the electron, so that the generation current itself will be:

$$I_g = eA \int_{-x_p}^{x_n} U \, dx = -\frac{eAn_iW}{2\tau_0} \tag{2.93}$$

The third source of leakage current is due to effects at the surface of the device. This may be due to generation of carriers at the crystal surface. Here, the crystal lattice ends abruptly, leaving unsaturated covalent bonds; these lead to allowed states for electrons appearing within the forbidden band at the crystal surface. These may then act as generation-recombination centres. For N_{st} such traps per unit area of the surface, a similar derivation to that of equation (2.93) yields for a junction of area A [15]:

$$I_s = -\epsilon A n_i S \tag{2.94}$$

where:

$$S \equiv v_{th} \, \sigma_h \, N_{st} \tag{2.95}$$

is known as the surface recombination velocity, and is affected greatly by the conditions present at the surface. It may reach 10^5 $cm\ s^{-1}$ for a sand-blasted surface, whilst for a clean etched surface, it may be 10 $cm\ s^{-1}$. Surfaces coated

with a so-called passivating layer, usually silicon dioxide or silicon nitride, may exhibit a surface recombination velocity as low as 0.1 $cm\ s^{-1}$, due to saturation of all the bonds at the crystal surface.

Poor processing of devices may leave ionic contaminants on the crystal surface, which move under the application of an electric field. Such contaminants may also cause localised inversion on the p-side of the junction, leading to conducting pathways across the device. This may cause high leakage currents or breakdown. Such leakage currents typically behave as a resistive function of the applied bias voltage [16].

For silicon detectors, good process control and the use of passivating layers have reduced surface leakage currents so as to be negligible with respect to volume generation currents within the depletion region.

2.4 Pulse Formation in Semiconductor Detectors

When a minimum ionising particle passes through a semiconductor detector, it leaves behind it a trail of electron-hole pairs. The field in the detector must be high enough to suppress carrier recombination along the track of ionisation, and to sweep out the carriers from the depletion region. Since the speed of carrier motion rises linearly with applied field up to the saturation velocity, for a detector to give a fast pulse requires that the field be as high as possible throughout the depletion region. However for a device operated at its depletion voltage, the field drops linearly from its maximum value to zero across the detector (equation 2.65). For a device consisting of a rectifying junction on one face of a piece of n-type material, and on the other an ohmic metallisation, should the field reach the metal of the back contact, carriers will be injected into the semiconductor and the device will break down. This condition is termed "punch-through" [1]. Therefore, where

biasing the detector to over-depletion is required, this simple type of contact cannot be used. A non-injecting contact must be made; this [10] typically consists of a highly doped n-type layer between the lightly doped detector material and the back contact. The field then drops from $\mathcal{E}_{max} = eN_dW/\epsilon_0\epsilon_r$ to some value $\mathcal{E}_{min}$ over the lightly doped layer, and thence to zero across the n^+ region. Thus, the field is zero at the surface of the metal, and carrier injection is obviated.

In order to calculate the current and charge pulse shapes from a semiconductor detector, consider a typical device, which will be assumed, for generality, to be over-depleted [9]. If the minimum field at the edge of the n-region is $\mathcal{E}_{min}$, then the field throughout the n-region will be:

$$\mathcal{E}(x) = \frac{qN_d}{\epsilon_0\epsilon_r}x + \mathcal{E}_{min} \tag{2.96}$$

Let an incident ionising particle produce an electron-hole pair at the point x_0 within the depletion region (see Fig.2.10).

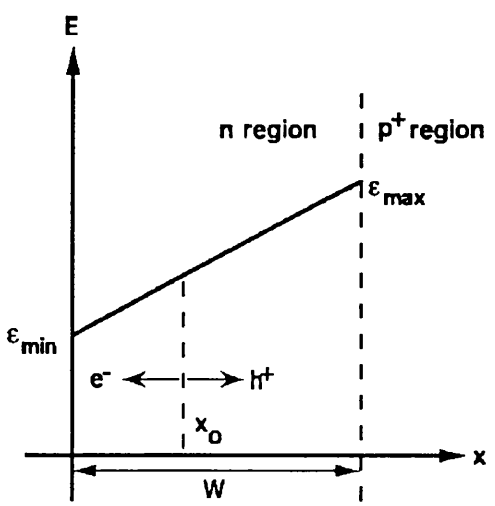

Figure 2.10: **Electric Field Inside the p-n Junction.**

The equation of motion of the hole will be:

$$\frac{d}{dt}x_h = \mu_h\frac{qN_d}{\epsilon_0\epsilon_r}x + \mu_h\mathcal{E}_{min} \tag{2.97}$$

The equation of motion of the electron will be:

$$\frac{d}{dt}x_e = -\mu_e\frac{qN_d}{\epsilon_0\epsilon_r}x - \mu_e\mathcal{E}_{min} \tag{2.98}$$

Integrating these two equations subject to the initial condition that $x = x_0$ at $t = 0$, the positions of the carriers evolve according to:

$$x_h = -\frac{\epsilon_0\epsilon_r}{qN_d}\mathcal{E}_{min} + \left(x_0 + \frac{\epsilon_0\epsilon_r}{qN_d}\mathcal{E}_{min}\right) exp^{\frac{\mu_h qN_d}{\epsilon_0\epsilon_r}t} \tag{2.99}$$

for $0 \leq t \leq t_h$, where t_h is the hole collection time, and:

$$x_e = -\frac{\epsilon_0\epsilon_r}{qN_d}\mathcal{E}_{min} + \left(x_0 + \frac{\epsilon_0\epsilon_r}{qN_d}\mathcal{E}_{min}\right) exp^{-\frac{\mu_e qN_d}{\epsilon_0\epsilon_r}t} \tag{2.100}$$

for $0 \leq t \leq t_e$, where t_e is the electron collection time. From these expressions, the collection times for the carriers may be found explicitly by setting $x = 0$ for electrons and $x = W$ for holes and solving for t. Thus:

$$t_h = \frac{\epsilon_0\epsilon_r}{\mu_h qN_d}\ ln\frac{W + (e/qN_d)\mathcal{E}_{min}}{x_0 + (e/qN_d)\mathcal{E}_{min}} \tag{2.101}$$

and:

$$t_e = \frac{\epsilon_0\epsilon_r}{\mu_h qN_d}\ ln\frac{x_0 + (e/qN_d)\mathcal{E}_{min}}{(e/qN_d)\mathcal{E}_{min}} \tag{2.102}$$

Differentiation of (2.99) with respect to time yields the time dependence of hole velocity:

$$v_h = \mu_h\left(\mathcal{E}_{min} + \frac{qN_d}{\epsilon_0\epsilon_r}x_0\right) exp^{\frac{\mu_h qN_d}{\epsilon_0\epsilon_r}t} \tag{2.103}$$

whilst (2.100) yields the electron velocity:

$$v_e = -\mu_e\left(\mathcal{E}_{min} + \frac{qN_d}{\epsilon_0\epsilon_r}x_0\right) exp^{-\frac{\mu_e qN_d}{\epsilon_0\epsilon_r}t} \tag{2.104}$$

Considering the detector as two infinite, parallel plane electrodes, the current induced by a charge carrier moving between the electrodes is given by Ramo's Theorem [11],[13] to be $i = q\frac{v}{W}$. This expression also holds in the presence of the space charge due to dopant atoms present in a real device [12]. Thus, the currents induced by the electron and hole traversing the detector are:

$$i_h(t) = \frac{q}{W}\mu_h\left(\mathcal{E}_{min} + \frac{qN_d}{\epsilon_0\epsilon_r}x_0\right) exp^{\frac{\mu_h qN_d}{\epsilon_0\epsilon_r}t} \quad , \quad 0 \leq t \leq t_h \tag{2.105}$$

and:

$$i_e(t) = \frac{q}{W}\mu_e\left(\mathcal{E}_{min} + \frac{qN_d}{\epsilon_0\epsilon_r}x_0\right)exp^{-\frac{\mu_e qN_d}{\epsilon_0\epsilon_r}t} \quad , \quad 0 \leq t \leq t_e \qquad (2.106)$$

These two expressions may be integrated with respect to time to give the charges induced by the two carrier types as they travel across the device:

$$Q_h = \frac{\epsilon_0\epsilon_r}{WN_d}\mu_h\left(\mathcal{E}_{min} + \frac{qN_d}{\epsilon_0\epsilon_r}x_0\right)\left[exp^{\frac{\mu_h qN_d}{\epsilon_0\epsilon_r}t} - 1\right] \qquad (2.107)$$

and:

$$Q_e = \frac{\epsilon_0\epsilon_r}{WN_d}\mu_e\left(\mathcal{E}_{min} + \frac{qN_d}{\epsilon_0\epsilon_r}x_0\right)\left[1 - exp^{-\frac{\mu_e qN_d}{\epsilon_0\epsilon_r}t}\right] \qquad (2.108)$$

For incident radiation interacting at a localised point within the detector volume, the current and charge pulses are approximately described by the expressions given, but with the charge q replaced by the total charge liberated by the ionisation. For an incident minimum ionising particle, the contributions of all the individual electron-hole pairs must be taken into account. Fig.2.11 shows the expected charge pulse from MIPs in a $160\mu m$ thick gallium arsenide device; this thickness was chosen as it yields the same total charge for MIPs as would a typical $300\mu m$ silicon detector. A donor concentration of $10^{13}cm^{-3}$ was assumed and the device was taken to be just depleted.

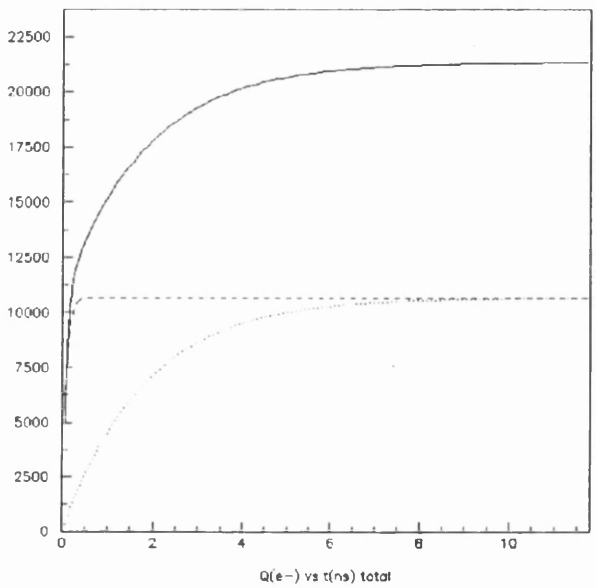

Figure 2.11: **Theoretical Charge Pulse for MIP in** $160\mu m$ **GaAs Detector.** Horizontal Axis: Time (ns). Vertical Axis: Collected Charge (electrons). **Dotted Line: Holes. Dashed Line: Electrons. Full Line: Total.**

References

[1] SZE,S.M. *Semiconductor Devices: Physics and Technology (Wiley)*

[2] TYAGI,M.S. *Semiconductor Materials and Devices (Wiley)*

[3] ALLEN,J.F. *Lectures on Physical Electronics, University of St. Andrews*

[4] KITTEL,C. *Solid State Physics (Freeman)*

[5] KITTEL,C. and KROEMER,H. *Thermal Physics (Freeman)*

[6] SEYMOUR,J. *Electronic Devices and Components (Pitman)*

[7] SZE,S.M. and GIBBONS,G. *Applied Physics Letters, 8, 111 (1966)*

[8] BERTOLINI,G. and COCHE,A. (Editors) *Semiconductor Detectors (North-Holland)*

[9] GATTI,E. and MANFREDI,P.F. *Rivista Del Nuovo Cimento, Vol.9, No.1 (1986)*

[10] ENGLAND, J.B.A. and HAMMER, V *Nuclear Instruments and Methods 96 (1971)*

[11] RAMO,S. *Proceedings of the Institute of Radio Engineers, 27, 584 (1939)*

[12] CAVALLERI, G. et al. *Nuclear Instruments and Methods 21 (1963)*

[13] WILLIAMS, R. *PhD Thesis, University of Tasmania (1974)*

[14] SAH, C-T., NOYCE, R.N., and SHOCKLEY, W. *Proceedings of the Institute of Radio Engineers (1957)*

[15] GROVE,A.S. and FITZGERALD,D.J. *Solid-State Electronics Vol.9 (1966) 783-806*

[16] ALEXIEV,D. and BUTCHER,K.S.A. *Nuclear Instruments and Methods A317 (1992) 111-115*

Chapter 3

Testing of Simple GaAs Detectors

3.1 Introduction

This chapter outlines the procedures and facilities used to manufacture simple pad detectors at Glasgow and elsewhere. Details of testing of devices are described. Simple detectors have been characterised in terms of their current-voltage characteristics and response to radioactive sources. Materials grown by different processes (Liquid Encapsulated Czochralski (LEC), Vertical Bridgman, Liquid Phase Epitaxy and thermally treated LEC) have been compared in terms of their performance. Some charge collection inefficiency has been found for detectors made on semi-insulating material; this appears to be due to a limited sensitive thickness. The behaviour of this sensitive thickness with bias voltage has been studied. Speed of response of the devices has been examined in view of the fast collection time which will be required for operation at LHC. Radiation hardness results for neutron and gamma irradiation are presented in the next chapter.

3.2 Fabrication of Devices for Test

Detectors made by the Glasgow High Energy Physics Group were fabricated using the facilities of the University of Glasgow Department of Electrical and Electronic Engineering. The simplest device structure consisted of a chip of gallium arsenide a few millimetres square, with an ohmic contact over the whole of one surface, and a circular Schottky contact in the centre of the other surface. Microstrip type detectors were also made at Glasgow.

3.2.1 Choice of Wafer Material and Thickness

Most of the detectors were made of the commonly available LEC-grown material, which is supplied by the manufacturers as a substrate for GaAs integrated circuit fabrication. Undoped, semi-insulating gallium arsenide was used, which according to (2.73) should give a device in which the depletion region extends across the whole detector thickness, even when no external bias voltage is applied. Such material is commonly supplied in the form of circular wafers two, three or four inches in diameter, and of thickness 500 or 600μm, depending on the manufacturer.

At the time when the first detectors were made at Glasgow, the LEC type of material appeared to be the only promising solution for the manufacture of detectors for minimum ionising particles (MIPs). For such particles, the amount of charge deposited by the ionisation process within the volume of the detector is proportional to the detector thickness. The energy required to create an electron-hole pair in GaAs is approximately 4.2 eV, compared to 3.6 eV in silicon [10], and the most probable energy loss of MIPs is 57 keV per hundred μm in gallium arsenide, compared to 28 keV per hundred μm in silicon. Thus, in order to obtain a signal charge from a gallium arsenide device of comparable magnitude to that from a typical, 300μm thick silicon detector, the gallium arsenide device should be 160μm thick. Furthermore, in a collider experiment, it is required that the probability of photons converting to electron-positron pairs be minimised except

within the calorimeter; for this reason also, gallium arsenide detectors would be made thinner than their silicon counterparts, because of their higher radiation length ($X_o = 2.3cm$). Only the LEC and Bridgman growth techniques were able to provide material of thickness in excess of the order of $10\mu m$, although thicker layers of gallium arsenide grown by epitaxial techniques had been reported previously [20], and have been obtained and tested more recently.

3.2.2 Ohmic Contact Deposition and Annealing

Wafers supplied by the manufacturer were first thinned to the required thickness. This was achieved by machine-lapping with $3\mu m$ alumina abrasive. A chemical polish using sodium hypochlorite solution followed.

Before evaporating the ohmic contact, the wafer was successively cleaned in trichloroethane, acetone, and isopropanol, with ultrasonic agitation. Care was taken not to allow any solvent to dry on the surface of the gallium arsenide sample. The final rinse was deionised water, following which the sample was dried under a stream of compressed nitrogen.

After cleaning, the sample was deoxidised in 1:4 hydrochloric acid:water for 30s, to remove the oxide film which forms on the surface of the material in air. It was then loaded into the evaporating plant, which was pumped down before an RF plasma cleaning cycle was carried out, as a further precaution against oxide or contaminants on the material surface.

The ohmic contact was then evaporated onto the surface of the sample; the evaporator used was of the electron beam type, under microcomputer control. The contact was evaporated at a pressure of around $2 \times 10^{-6} mbar$. The recipe for the ohmic contact was: 5nm nickel, 25nm germanium, 43nm gold, 30nm nickel and 50 nm gold, in that order [16]. The contact was then annealed at $360°C$ for a time of 20s. The anneal has the effect of diffusing the germanium into the surface of the gallium arsenide; germanium being a group IV element acts as a

donor by occupation of gallium antisites. Thus, a highly doped n-region is formed below the metal contact, leading to non-rectifying behaviour. The initial nickel layer acts as a wetting agent for the alloyed germanium:gold layer [13]; however nickel diffuses readily into gallium arsenide, whereupon it acts as an acceptor [14]. Thus, the nickel layer used should be as thin as practicable.

3.2.3 Photolithography and Schottky Contact Deposition

The areas of metallization for the Schottky contact were defined by standard photolithographic techniques. Firstly, positive photoresist was spun onto the surface of the gallium arsenide sample; Shipley S1400-31 resist was used. The resist was then baked for 30 minutes at $95°C$ in the case of simple devices. When more complicated structures such as microstrip detectors were made, the resist was baked for 15 minutes, following which it was soaked in chlorobenzene for 15 minutes, and finally baked for a further 15 minutes. The chlorobenzene soak hardens the surface of the resist and leads to better results at the lift-off stage. The resist was exposed to a UV light source through a mask which was transparent in those areas where the Schottky metallisation was required; contact printing was used for most devices, as it was not necessary to align any subsequent metal layers. The exposed resist was developed according to the manufacturer's recommendations, and a deoxidation step was employed as for the ohmic contact, before commencing the evaporation of the Schottky contact.

The recipe of the Schottky contact consisted of 30nm of titanium, followed by 80nm of gold. Gold diffuses readily into the surface of gallium arsenide, and the titanium layer is primarily a barrier to prevent this from occurring. After the Schottky evaporation, the samples underwent lift-off in warm acetone over a water bath; here the acetone dissolves the resist, removing the metal layer from those areas where it is not required. The samples were then cleaned with isopropanol, rinsed with deionised water, and dried under compressed nitrogen. Finished devices were cut from the wafer using a mechanically driven diamond-

tipped scriber in the case of small detectors. Microstrip detectors were cut from the wafer by Micron Semiconductor Ltd., using a diamond saw.

3.2.4 Mounting and Bonding

Finished devices were mounted for testing; for microstrip detectors, custom made printed circuit boards were used, whilst for simple devices the most common mount used was a T05 transistor header. Conductive adhesives were used to locate the devices onto their mounts, simultaneously providing the means of electrical connection to the ohmic contact. Schottky contact connections were made by use of an ultrasonic wedge type wire bonding machine. For the repetitive task of bonding microstrip detectors for beam testing, the work was performed at Rutherford Appleton Laboratory, using an automated bonder.

3.3 LEC Detector Test Results

3.3.1 Current-Voltage Characteristics

The devices in Batch 27 and Batch 28 were typical of detectors made at Glasgow, on semi insulating LEC material supplied by MCP Wafer Technology Ltd. The wafers were thinned to a nominal thickness of $200\mu m$ in the Department of Electrical and Electronic Engineering, and subsequently measured to be $150 \pm 5\mu m$ thick. The diameter of the circular Schottky contacts was measured to be 1.1mm.

The properties of the gallium arsenide wafers used, as measured by the manufacturer, are shown in table 1. From the quoted values, the expected depletion voltage of these detectors would be less than the built-in voltage of the Schottky contact. The electron mobility in this material is improved over that used by Kobayashi and Takayanagi in 1966 [19], indicating the improvement in crystal growth techniques over the intervening period.

Table 3.1: Characteristics of MCP SI GaAs Wafers

Diameter $[mm]$	50.9
Orientation	$< 100 >$
Dopant	none
Wafer flatness $[\mu m]$	< 3
Wafer thickness $[\mu m]$	$500 + / - 25$
Mass $[g]$	5.37
Resistivity $[\Omega cm]$	$7.5 \times 10^7 - 1.2 \times 10^8$
Mobility $[cm^2V^{-1}s^{-1}]$	$6.8 \times 10^3 - 6.6 \times 10^3$
Carrier Concentration $[cm^{-3}]$	$1.2 \times 10^7 - 8.2 \times 10^6$
Etch pit density $[cm^{-2}]$	$2.1 \times 10^4 - 3.0 \times 10^4$

Figs.3.1 and 3.2 show the reverse bias current-voltage characteristics for the batch 27 and 28 samples. These results were taken using a Hewlett-Packard combined voltage source and picoammeter, interfaced to a Macintosh II computer. The output voltage of the supply was scanned from 0 to 100V in steps of 1V, for

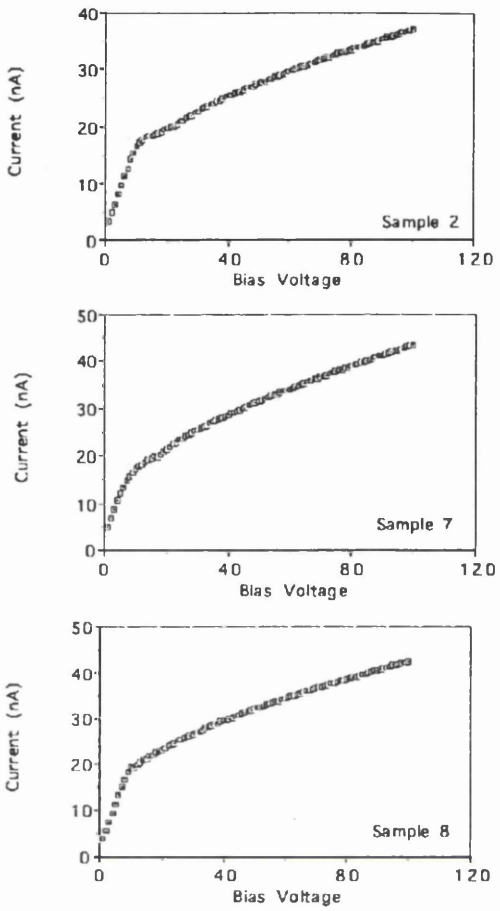

Figure 3.1: **Reverse Bias Currents for Batch 27 Samples**

each of which the current through the device was recorded. The time taken for each voltage step was 0.5s. It can be seen that, at 100V reverse bias at room temperature, the current varies between 43 and 65 nA per square millimetre area of the Schottky contact. The reverse current is uniform amongst the samples of each batch to within 10 percent. Reverse currents of this magnitude are greater than those typically found in silicon detectors by more than two orders of magnitude. In forward bias conditions, the current through the device rose very rapidly with voltage above a threshold of around 10V, for all the Batch 27 and 28 samples tested.

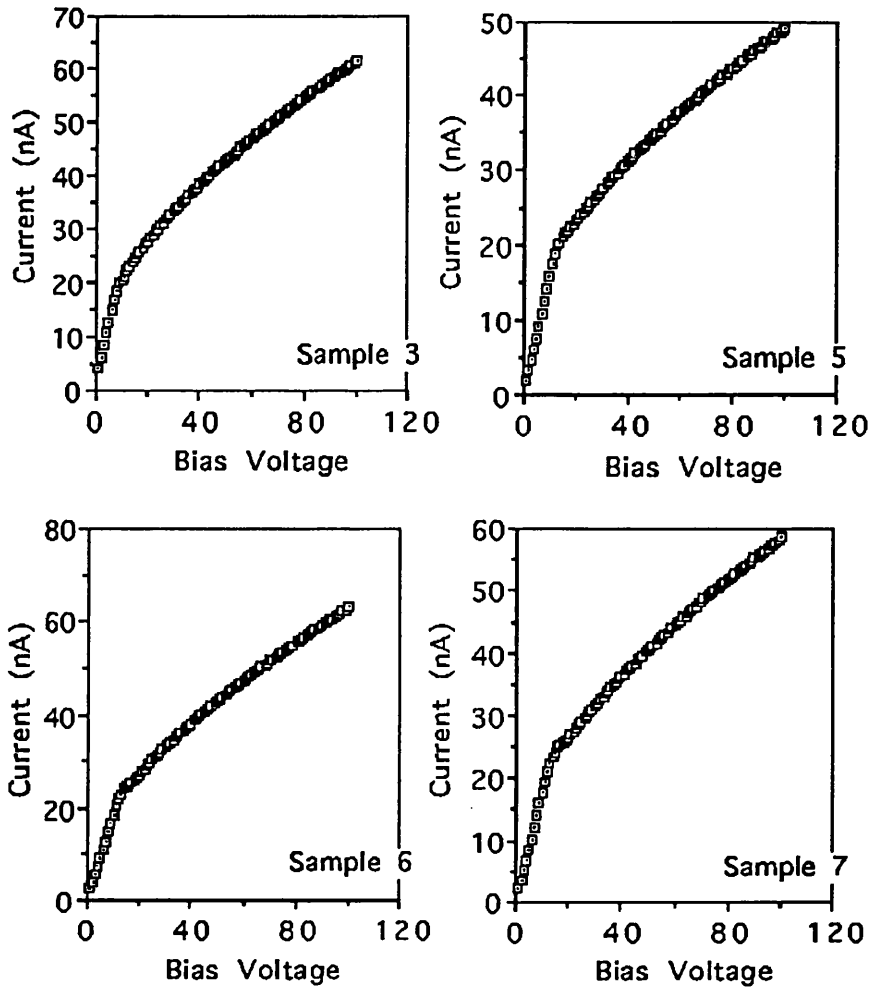

Figure 3.2: **Reverse Bias Currents for Batch 28 Samples**

3.3.2 Leakage Current Sources

In order to obtain information on the source of the leakage currents, one of the devices was mounted on a cold finger of the type commonly used for the operation of germanium detectors at low temperature. A thermocouple was used to monitor the temperature of the test device, whilst the cold finger was cooled using liquid nitrogen, and current versus voltage scans performed as before, at a selection of temperatures varying between that of liquid nitrogen and room temperature.

The generation current from within the depletion region of a reverse biased diode

is given by (2.93), and is proportional to the intrinsic carrier concentration of the material used, which is itself temperature dependent. The same temperature dependence applies to surface leakage currents, as in equation (2.94), if such currents are due to generation. Substituting for n from (2.29) and p from (2.30) into $pn = n_i^2$, this temperature dependence is given by:

$$I_{g-r} \propto n_i = \sqrt{N_c N_v} exp^{-\frac{E_g}{2kT}} \tag{3.1}$$

Surface currents due to conducting channels are expected to show a much smaller exponential temperature coefficient [21]. Current due to thermionic emission over the Schottky barrier might be expected to show an exponential temperature coefficient of similar magnitude to that of generation from equation (2.59), since the barrier height for a gold Schottky contact on gallium arsenide is $\sim 0.8eV$ [23]. However, a calculation showed that such a current would be negligible compared to the leakage current observed experimentally. Thus, a plot of ln(I) versus 1/T would have gradient $-\frac{E_g}{2k}$ if generation-recombination is the dominant source of leakage current. Fig.3.3 shows such a plot, performed for a fixed bias voltage of 50V. Fits are shown to the two linear regions. the first region extends from $20°C$ to around $-3°C$ with gradient $-1.0 \times 10^4 K$, and the second has extends from $-3°C$ to $-35°C$ with gradient $-1.5 \times 10^3 K$.

The former value is consistent with a band gap energy of 1.8+/-0.4 eV, which is close to the accepted value of 1.4eV in gallium arsenide; thus, it seems that generation currents are the source of the high leakage around room temperature. It was further noticed that, for devices of different thickness, the leakage currents were similar amongst devices from the same wafer whilst varying widely from wafer to wafer and were not correlated with thickness. Thus, it seemed probable that the dominant defects responsible for the leakage current are associated with the surface preparation of the detector.

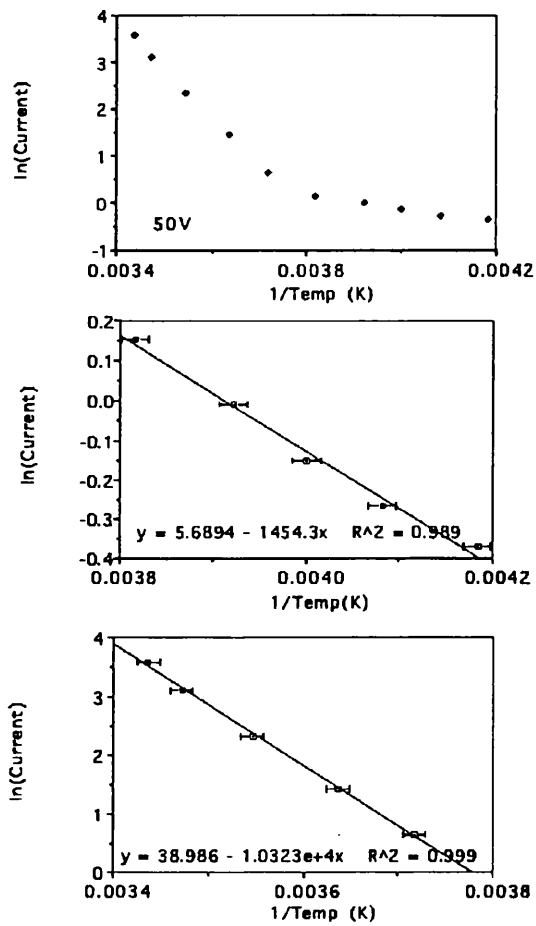

Figure 3.3: **ln(Leakage Current) vs 1/T for Batch 28 Sample 7 Showing Linear Fits.**

Two arrays of circular pads on MCP material were characterised in terms of leakage current; each array consisted of 16 pads of diameter $1mm$ and 16 of diameter $3mm$. For the first array, the mean leakage current was $48.3nA$, whilst that of the large pads was $158.9nA$. For the second array, these figures were $23.6nA$ and $61.6nA$ respectively. In both cases, these scale as the perimeter of the pads rather than the area. This indicates that surface leakage currents dominate [22].

From equations (2.93) and (2.94), it is apparent that the volume generation current should scale in the same manner as the depletion region width, thus showing a $V^{1/2}$ dependence according to equation (2.73). In this case, if

generation in the depletion region were to dominate the leakage current, a graph of $ln(I_L)$ versus $ln(V)$ should exhibit a gradient of $1/2$, significant departure from this value indicating the dominance of surface generation. However, as will be outlined later, the active region depth of detectors fabricated on semi-insulating material does not follow the expected $V^{1/2}$ dependence; consequently results from this type of analysis will not be presented.

3.3.3 Charge Collection for Alpha Sources

The Batch 27 and 28 samples were exposed to a ^{241}Am alpha source; the alphas were incident on the Schottky contact and the device was reverse biased in each case. A charge-sensitive pre-amplifier was used, with a shaping amplifier of time constant $0.5\mu s$. The output of the shaping amplifier was fed to a multichannel analyser, so that pulse-height spectra could be recorded. The device under test and the source were placed inside an evacuated metal container. Figs.3.4 and 3.5 show the charge collected as a function of bias voltage for each device. For alphas of energy 5.45MeV, the total charge liberated by the alphas being stopped in gallium arsenide is 0.21pC, taking the energy required to liberate an electron-hole pair as 4.2eV.

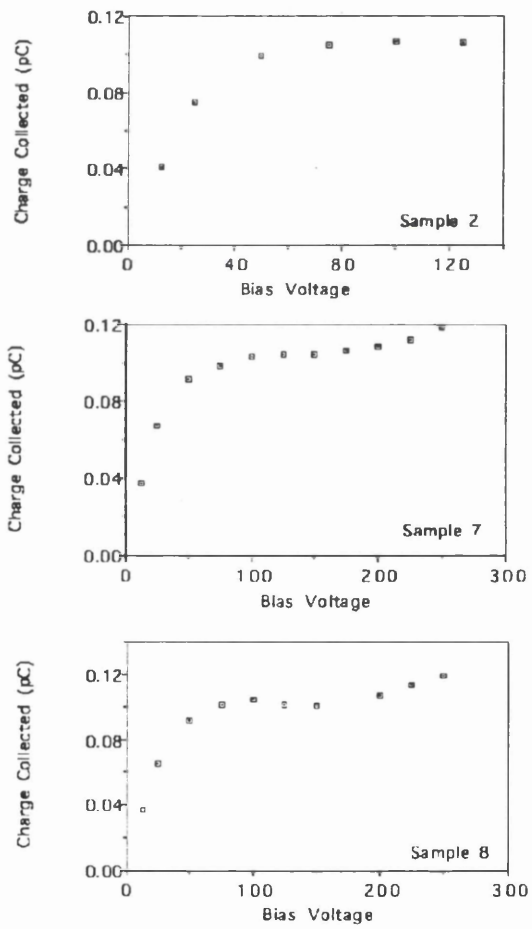

Figure 3.4: Charge Collection for Batch 27 Samples

Batch 28 sample 5 was anomalous, and broke down around 100V, only reaching a charge collection efficiency of around 30 percent. The rest of the samples behaved in a uniform manner, with a plateau of around 50 percent in charge collection efficiency beginning at 100 V. Those devices which would allow a higher bias voltage to be applied without breakdown showed a further increase in charge collection efficiency beginning at around 200 V. The best charge collection efficiency achieved was 60 percent. Breakdown voltages showed a noticeable variation amongst samples of the same batch, varying between 150 and 300 V from device to device.

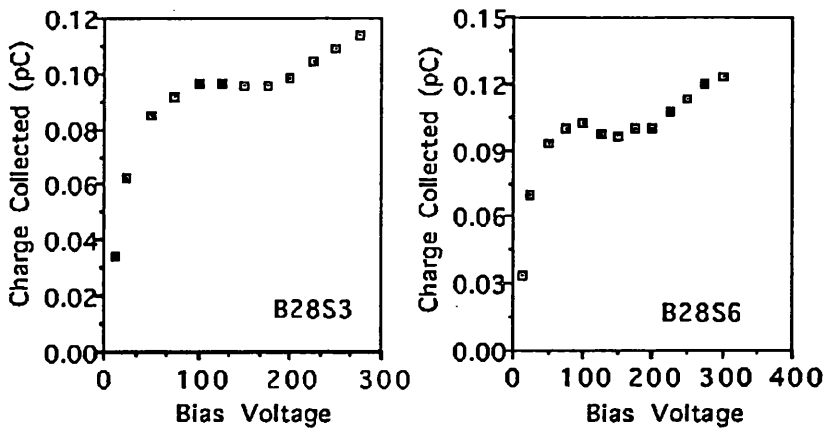

Figure 3.5: **Charge Collection for Batch 28 Samples**

3.4 Trapping and Charge Collection Efficiency

From the test results of many early devices, similar to the Batch 27 and 28 devices, it had been seen that the charge collection efficiency was always less than 100 percent. Tests of $125\mu m$ thick diodes showed charge collection efficiencies of around 47 percent for alphas and 25 percent for minimum ionising betas, at a reverse bias voltage of 100V [10].

In order to investigate the origin of the charge collection inefficiency, the detectors were exposed to a ^{241}Am alpha source incident on the ohmic contact. Due to the

short range of the alphas in gallium arsenide, from Ramo's Theorem [24] it may be considered that an alpha particle incident on the Schottky contact of a detector will give an output pulse due to electrons only, and an alpha particle incident on the ohmic contact will give a pulse due to holes only. In this manner, the relative contributions of charge carriers of either sign to the total pulse could be evaluated. Since it is known that the hole trapping length in most semiconductors is two orders of magnitude smaller than the electron trapping length, it was reasonable to expect a difference in charge collection efficiency between the two types of carrier.

It was found that an alpha spectrum recorded with the source incident on the ohmic contact held few counts, with a flat distribution up to the maximum channel observed with the source incident on the Schottky contact (Fig.3.6).

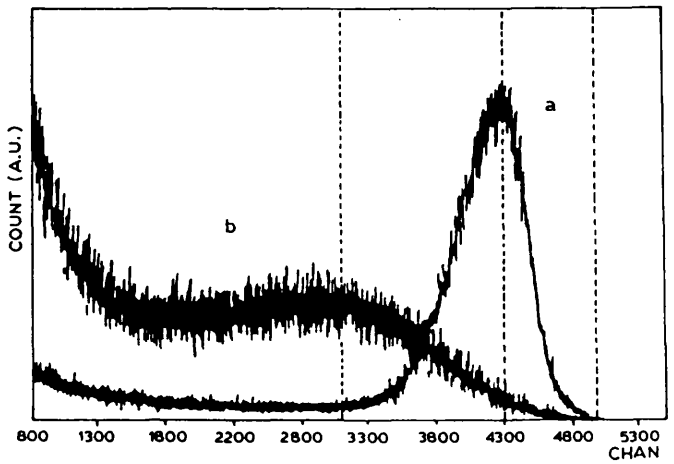

Figure 3.6: **Pulse Height Spectra for an Alpha Source Illuminating (a) the Schottky Contact and (b) the Ohmic Contact. (From [11])**

Clearly, the collection of holes was much less efficient than that of electrons at the field involved. Plotting charge collection efficiency versus bias voltage for the two situations revealed that above a threshold field of around $0.7V/\mu m$, hole collection efficiency increased rapidly to be ultimately of the same order as the electron collection efficiency (Fig.3.7).

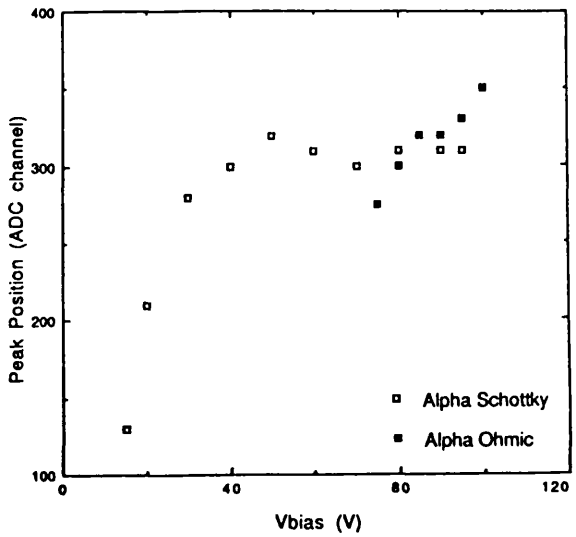

Figure 3.7: **Peak Postion vs. Bias for Alpha Particles Incident on the Schottky and Ohmic Contacts. (From [11])**

It was therefore proposed [10] that the explanation for the poor charge collection efficiency was due to holes liberated in the semiconductor being rapidly trapped as they were swept through the material by the field. This explains the better charge collection efficiency for alphas incident on the Schottky contact than for those incident on the ohmic contact. For the case of the minimum ionising betas, a column of ionisation throughout the thickness of the device would give a pulse the charge of which would be one half due to electrons and one half due to holes, if the detector were perfect. If all the holes were trapped before drifting significantly, then the charge collection for betas would be less than that for alphas, as had been observed. High enough fields might allow hole collection by stimulating the release of trapped carriers.

A simple calculation was performed, which assumed that the number of electrons contributing to the charge pulse decreased exponentially with distance travelled, due to trapping phenomena, according to:

$$n(x) \quad = \quad n(0)\ exp^{-\frac{x}{\lambda}} \tag{3.2}$$

where λ is the electron trapping length.

The field in the detector was taken to be constant throughout its depth, the built-in field due to the Schottky contact being negligible in comparison to that due to the applied bias voltage. This would lead to a constant carrier drift velocity everywhere within the device. Hole collection efficiency was assumed to be zero. The electron attenuation length for the detectors tested was calculated for each bias voltage using the charge collection data for alphas, and the attenuation length so obtained used to predict the expected charge collection efficiency for betas. It was found that the measured charge collection efficiency for betas was consistently less than that calculated, although by a factor of less than 2. Furthermore, the model predicted a rate of rise of charge collection efficiency with applied bias which was less than that obtained empirically. The first result might be explained by the existence of a non-uniform field leading to poorer charge collection in some regions of the device than in others, whilst the second might be explained by hole collection being large enough to be non-negligible, and increasing with the applied field.

Confirmation of the alpha particle results was obtained using a variable energy proton beam from the Van de Graaf accelerator at the University of Florence. For a $125\mu m$ thick device, the maximum charge collection efficiency achieved before breakdown was 70 percent for 2 MeV protons incident on the Schottky contact, and 43 percent for 2 MeV protons incident on the ohmic contact (Fig.3.8). The range of 2 MeV protons in gallium arsenide is approximately $30\mu m$ [2]. However, protons of energy 3 MeV gave a charge collection efficiency of 76 percent when incident on the Schottky contact, and 82 percent when incident on the ohmic; their range is $60\mu m$, close to the centre of the detector thickness. The charge collection found is greater than would be expected from the trapping model above.

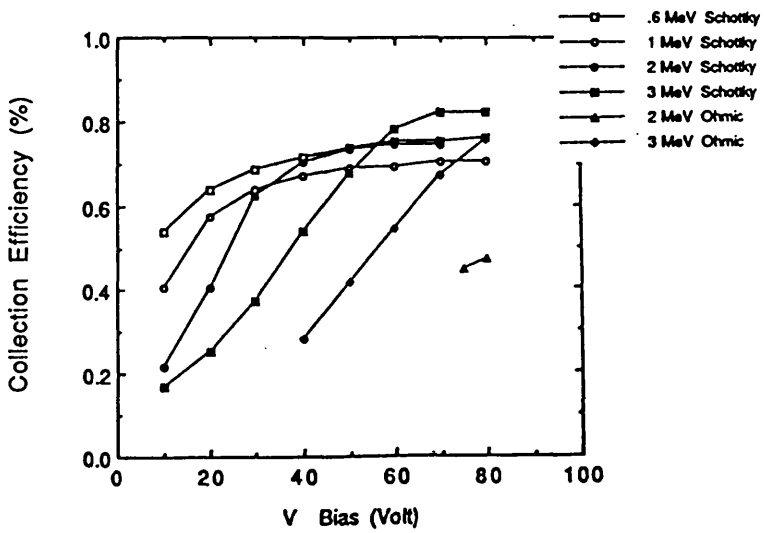

Figure 3.8: Charge Collection Efficiency vs. Bias for Protons Incident on the Schottky and Ohmic Contacts. (From [11])

3.5 Charge Collection Efficiency for Different Materials

It was expected that different types of gallium arsenide material might have different charge collection properties, in view of the variation of defect type and concentration with the growth technique used. The charge collection efficiency for alpha particles was examined as a function of applied bias volts for devices made on materials other than the standard LEC material used previously.

Batch 38 devices were made on a sample of material grown by the Low Pressure Vapour Phase Epitaxy (LP-VPE) process, by Dr. R. Beccard, of the Technical University of Aachen [3]. The substrate was chromium-doped semi-insulating gallium arsenide, the epitaxial layer being $50\mu m$ thick, with a free carrier concentration of the order of $10^{14}cm^{-3}$. The electron mobility was reported as being $6 \times 10^4 cm^2 V^{-1} s^{-1}$ at liquid nitrogen temperature.

Batch 57 samples were made on a Vertical Bridgman grown wafer, from Crystal Specialties International. This was undoped, semi-insulating material. The Ver-

tical Bridgman process uses a travelling furnace for zone refining of the material, rather than pulling a crystal from the melt, as with the LEC process. The former involves lower temperature gradients, and hence gives a lower dislocation density. VB material is also likely to contain higher quantities of silicon contaminant than LEC material. Carbon must be added to provide charge compensation for the silicon if semi-insulating material is required [5]. The overall compensation within the material depends on the relative quantities of carbon shallow acceptors, silicon shallow donors, and EL2 deep donors. The electron mobility reported by the manufacturer was somewhat lower than that reported by MCP Wafer Technology, at $5700 cm^2 V^{-1} s^{-1}$; this indicated that the VB material was more heavily compensated. The wafers were thinned to $200 \mu m$.

The Batch 58 samples were made on a semi-insulating wafer supplied by MCP Wafer Technology, which had been grown by the LEC technique but had been subjected to a non-standard post growth heat treatment [6], in which the ingot had been heated to $1100^o C$ and then allowed to cool in air to room temperature. The wafers from this ingot were characterised by the photoluminescence (PL) technique, being found to give an unusually bright and uniform PL map across the wafer area. Bright PL mappings are indicative of a long minority carrier lifetime within the material [9], and it was hoped that this might improve the charge collection efficiency of detectors made on this type of material. It was also reported that a further effect of the rapid quench was to increase the dislocation density in the material by over two orders of magnitude. The concentration of the EL2 defect was unchanged. The wafer was thinned to $200 \mu m$ before deposition of the contacts.

Figs.3.10 and 3.12 show charge collection efficiency versus bias for alpha particles for all the samples tested, by batch. Their reverse bias current-voltage characteristics for bias voltages of 0-100V are shown in Figs.3.9 and 3.11.

The Batch 57, Vertical Bridgman devices show rather lower reverse bias leakage

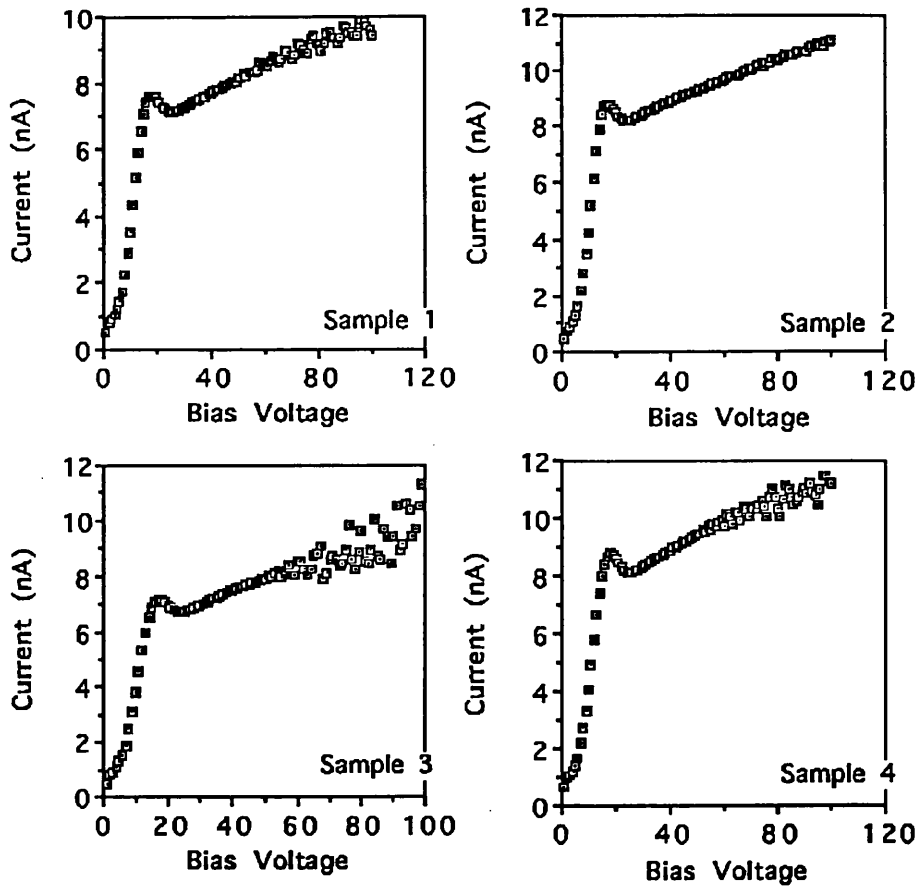

Figure 3.9: **Reverse Bias Currents for Batch 57 Samples**

currents than is usual with LEC material, but three of the samples tested showed evidence of low frequency oscillations in the leakage current occurring above 50V, as had been reported previously for the same type of material [7]. Resolution for alpha particles was poor. The rise of charge collection efficiency with bias was slower than that seen in the Batch 27 and 28 results shown earlier, with three of the samples only reaching 30 percent charge collection efficiency before breakdown, which typically occurred at voltages between 75V and 175V, lower than those of the LEC devices. However, it was found that the sample which had not shown current oscillations below 100V during the current-voltage measurement would withstand a bias of 400V before breakdown, yielding a maximum charge collection efficiency of 53 percent.

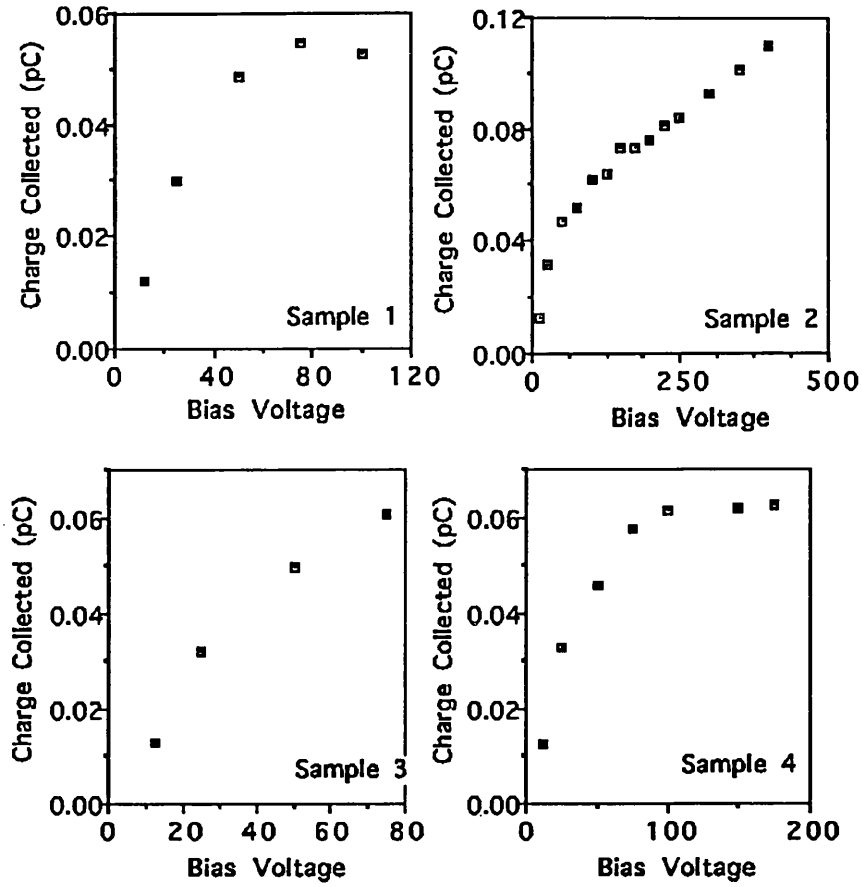

Figure 3.10: **Charge Collection for Batch 57 Samples**

The Batch 58, specially annealed LEC, samples showed reverse leakage currents of similar magnitude to the standard LEC material from the same manufacturer. Charge collection efficiency for alphas shows a similar rate of increase with applied bias to that of the standard material, with a plateau beginning around 100V, at 60 percent efficiency. A further slow increase in charge collection was observed above 250V, the best achieved being 76 percent at 550V. Breakdown voltage varied between 150V and 550V for the samples tested, and seemed to be rather higher in general than that of standard LEC material.

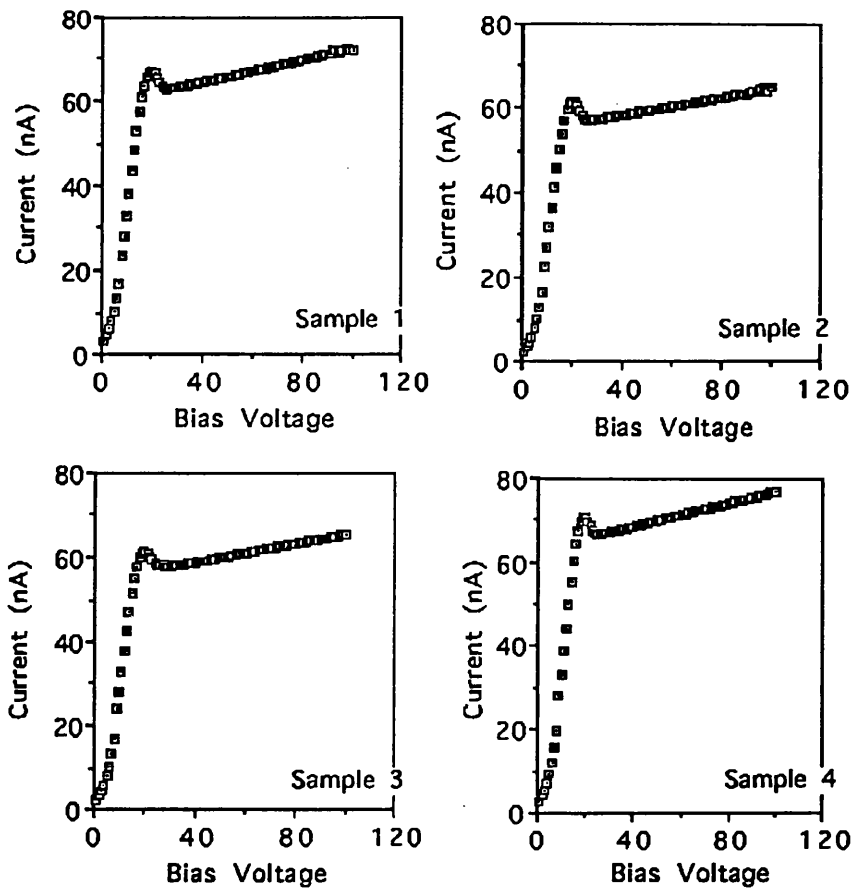

Figure 3.11: Reverse Bias Currents for Batch 58 Samples

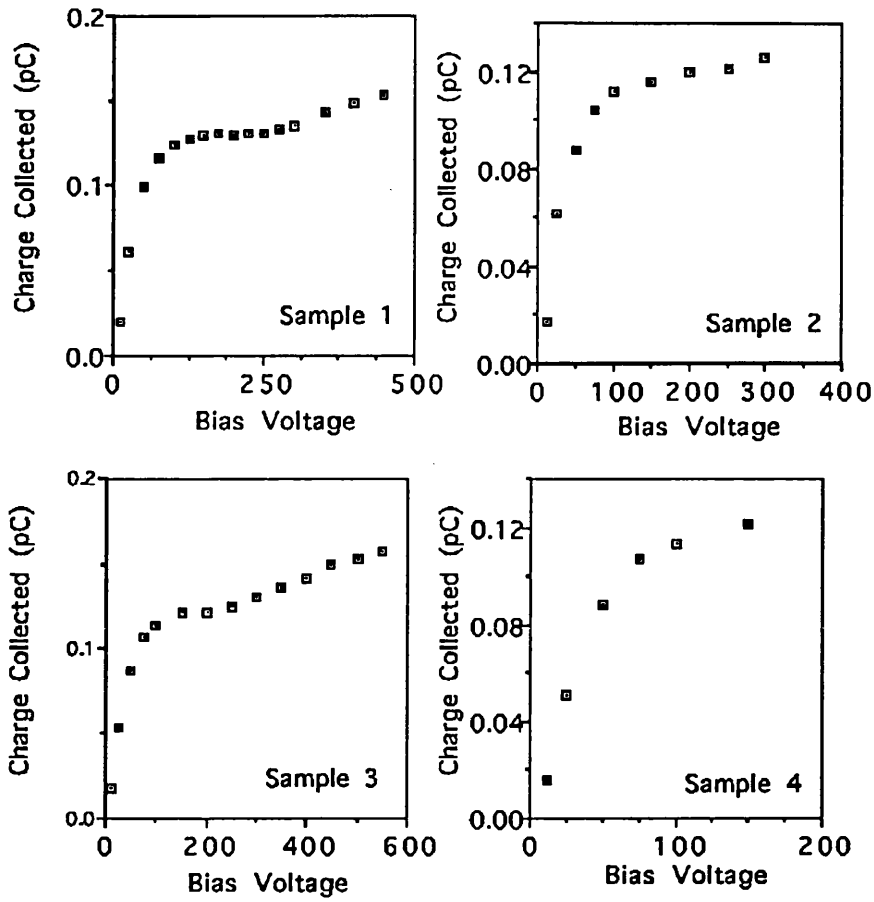

Figure 3.12: **Charge Collection for Batch 58 Samples**

The Batch 38, LP-VPE, sample showed a lower leakage current than LEC material, and gave a more rapid rise of charge collection efficiency with applied voltage. Charge collection reached a plateau above 100V of 100 percent efficiency. A variable-energy X-ray source was used to provide confirmation of the collection efficiency; the performance for low-energy X-rays was found to be very good, with 20keV Ag K-shell X-rays being well resolved from the noise pedestal at room temperature. Graphs of leakage current and charge collection variation with voltage are shown in Fig.3.13, as is an X-ray spectrum.

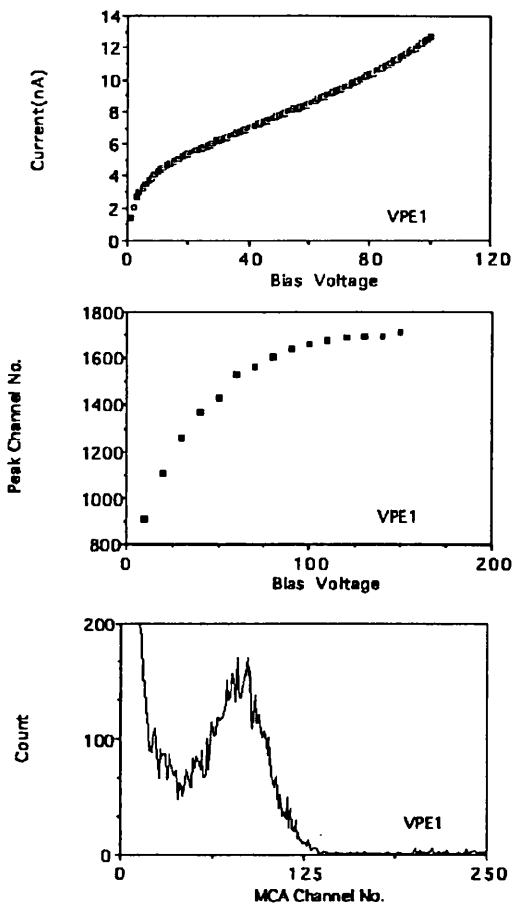

Figure 3.13: **VPE Sample Test Results: a) Reverse Current b) Charge Collection for Alphas c) Ag K-shell X-ray Spectrum**

3.6 Active Region Depth and Charge Collection Efficiency

An alternative explanation of the charge collection efficiencies observed with alpha and beta sources, proposed by McGregor [25], is that the field within the material is very non-uniform, due to ionisation of deep level donors, in particular the EL2 centre. In LEC semi-insulating gallium arsenide, the dominant defect is the EL2, which is associated with an arsenic atom occupying a gallium antisite [5]. The dominant contaminant is carbon, which behaves as a shallow acceptor by occupying an arsenic antisite. The semi-insulating behaviour is obtained by

growing the crystal in such a way that the carbon and EL2 concentrations will cause equal amounts of doping of opposite types. At room temperature, a typical carbon concentration of $10^{14}cm^{-3}$ will be compensated by $10^{16}cm^{-3}$ EL2s. A compensated material will have a very high resistivity, but the greater the impurity concentrations involved, the poorer will be the carrier mobility. Assuming $10^{16}cm^{-3}$ EL2 centres and $10^{14}cm^{-3}$ carbon shallow acceptors , Poisson's equation within the material becomes:

$$\frac{\partial^2 V}{\partial x^2} = \frac{e}{\epsilon_0}\left(N_d^+ - N_a^- - n_o\right) \tag{3.3}$$

where N_d^+ and N_a^- represent the number of ionised donor and acceptor impurities, respectively, and n_o is the intrinsic carrier concentration of the material, due to thermal promotion of electrons to the conduction band.

At room temperature, the acceptors lie sufficiently close to the valence band to be considered fully ionised. The intrinsic carrier concentration is $1.79 \times 10^6 cm^{-3}$, and may be neglected. The number of electrons on the EL2 centres will be given by:

$$n_{EL2} = N_{EL2} \cdot \frac{1}{1 + \frac{1}{2}exp\left(\frac{E_d - E_f}{kT}\right)} \tag{3.4}$$

Thus, the number of ionised EL2 centres will be:

$$N_d^+ = N_{EL2} \cdot \left(1 - \frac{1}{1 + \frac{1}{2}exp\left(\frac{E_d - E_f}{kT}\right)}\right) \tag{3.5}$$

Now, far from the Schottky contact, the Fermi level will lie mid-way between the valence and conduction bands. The EL2 level lies at 0.8eV below the conduction band edge; thus the number of ionised EL2 centres will tend towards zero. Close

to the Schottky contact, band bending will bring the level of the EL2s above the Fermi level; they will become ionised (Fig.3.14). Then the effective doping

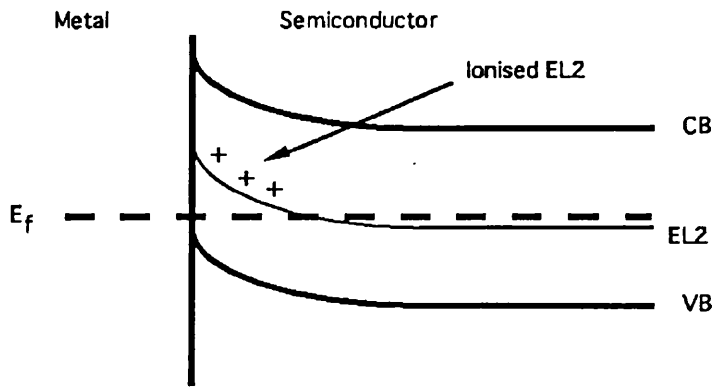

Figure 3.14: **Ionisation of EL2s Close to a Schottky Contact.**

density beneath the Schottky contact will approach the density of the EL2 centre, and there will exist two regions of field, a high field region close to the Schottky contact, and a low field region further away. Only in the high field region will carrier recombination be suppressed adequately, and so there will exist a limited depth across which the device is sensitive. The depth of this region would be expected to behave as if the material were moderately n-doped.

If it were assumed that charge trapping did not play any role in causing the observed deficit in charge collection efficiency, a detector in which the field behaved in this fashion would be expected to give 100 percent charge collection efficiency for alphas or low energy protons incident upon the Schottky contact. Virtually no charge would be collected for such particles incident on the ohmic contact, up to an applied bias large enough to cause the high field region to reach the back of the device; then the charge collection efficiency would be rise rapidly to 100 percent. Minimum ionising particles would give a collection efficiency equal to the ratio of the high field region depth to the overall device thickness. This model gives a good qualitative explanation of the results from irradiation with variable energy protons, assuming that the balance of the charge collection

efficiency between 80 and 100 percent can be accounted for by charge trapping and recombination. However, for the high field region to extend across the entire thickness of a $100\mu m$ thick device, at that voltage observed to cause a rapid increase of charge collection for alphas incident on the ohmic contact, suggests an effective doping concentration of 10^{13} to $10^{14} cm^{-3}$. This is lower than that expected from the EL2 centres alone; an unforeseen compensation mechanism may be involved.

3.7 Measurement of the Active Region Depth

3.7.1 Capacitance-Voltage Probing

From equations 2.73 and 2.76, it can be seen that an ideal p-n or Schottky junction behaves as a parallel plate capacitor whose cross sectional area is that of the junction, and the distance between whose plates is the depletion region width. Various commercial machines are available for the C-V profiling of junctions, but the principle of operation is the same for all. A constant bias voltage is first applied across the junction; a small alternating voltage is then superimposed on top of this. The resultant alternating current through the device allows determination of its capacitance. The depletion depth of the junction at any given voltage is then simply given by $W = (A\epsilon_0\epsilon_r)/C$.

Care must be taken in the use of this technique for semi-insulating gallium arsenide, however. Here, the defect levels lying just below the Fermi level will be populated and depopulated by the alternating probe voltage. If the probing frequency is too high, the emission time of the levels will be too long to allow their state of population to follow the probing voltage. A low frequency should therefore be used for this type of measurement.

Measurements of this type have been performed on gallium arsenide detectors; at high frequency the capacitance is constant with bias voltage and equal to

that value which would be calculated by treating the device as a parallel plate capacitor of plate separation equal to the physical thickness of the device. At low frequency, the capacitance is found to decrease with increasing bias voltage, as would be expected for a depletion region widening. For one particular device, made by Alenia S.p.A. using semi-insulating gallium arsenide manufactured by Sumitomo, the active thickness has been reported as $125\mu m$ at 200V applied across a $190\mu m$ device [1], in contrast to the full depletion expected from the trapping model. It was found that the increase of active thickness with applied bias was linear, rather than the expected $V^{1/2}$ dependence; this may be compared with the measurements on LEC material in [25], where a V^n dependence was found with n slightly greater than one.

3.7.2 Probing with a Scanning Electron Microscope

Further investigation of the sensitive region depth has been carried out by use of a scanning electron microscope (SEM). Devices were cleaved through their contacts, it having been found that their behaviour was not adversely affected by doing so. They were then placed so that their cleaved edges could be scanned by the beam, biased and connected to a charge-sensitive amplification system and multichannel analyser as for standard measurements of charge collection efficiency. The diameter of the beam spot was $0.05\mu m$, so it was possible to cause ionisation at different distances across the device thickness. Using this method, it was confirmed that, at fields less than $1V/\mu m$, only part of the thickness of the device was sensitive. The sensitive region width increased with increasing bias voltage. However, this method only deposits energy close to the surface of the device, due to the low energy of the electrons (10keV); it is hoped to repeat the same investigation using a proton microprobe, which will allow a greater penetration.

The use of a SEM also allowed the formation of an image of the detector by the voltage contrast technique. Here, the intensity of the image increases with

potential of the object. A visual map of the field inside devices was obtained, the regions of highest field appearing bright, and the regions of lowest field appearing dark. The bright region was found to extend only part of the way through the detector thickness, its width increasing with applied bias.

It was found [1] that this method gave a larger value for the device sensitive depth than did the capacitance measurement, being $155\mu m$ for the device and conditions outlined above. MIPs gave a charge collection efficiency consistent with the capacitance measurement across the range of bias 0-200V. Again, a linear rise of active region width with applied bias voltage was found.

3.7.3 Counting Rate for Gamma Rays

The value of the attenuation coefficient for 60 KeV gamma rays in gallium arsenide has been reported as approximately $900\mu m$ [1]. Then, if a known flux of gamma rays is incident upon a detector, the rate of counting the gammas may be considered to be proportional to the active thickness of the device. Implicit in this is the assumption that the change in the number of gallium or arsenic K-shell X-ray escapes as the sensitive region changes size is not great enough to affect the results. This type of measurement has been performed for several samples of LEC material; the experimental set-up was identical to that used to record the charge collection efficiency of detectors for gamma ray sources, but the number of counts in the photopeak per unit time was recorded for each bias voltage. Due to the lower energy edge of the peak overlapping the noise pedestal, the total number of counts in the peak was taken as twice the number recorded above the channel of maximum height.

Results were again consistent with a linear dependence of depth on bias. A $300\mu m$ thick silicon detector made by Micron Semiconductor Ltd. was tested using this technique. It was found that the count-rate increased as $V^{1/2}$ up to the expected depletion depth of the device, at which point a plateau began; evidently

the silicon device behaved exactly as predicted by theory.

3.8 Active Region Depth of Different Materials

In view of the results indicating that the dominant cause of loss of charge collection in semi-insulating materials is due to a limited active thickness, the method of gamma counting was used to compare the standard LEC material with VB material and thermally treated LEC material, in order to see if any material was superior in terms of sensitive region depth. Different types of material might have compensation occurring amongst different deep level centres, leading to different effective doping concentrations in the high field region. An ^{241}Am source was used, which emitted gamma rays of 60 keV. Charge collection efficiency was also recorded. Out of the devices in each batch, that with the highest breakdown voltage was selected for probing with gamma rays.

The charge collection efficiency of Batch 27 Sample 7 is shown against bias voltage in Fig.3.15. A linear rise is seen, in contrast to the results obtained with alpha particles. The best charge collection efficiency achieved was 81 percent at a

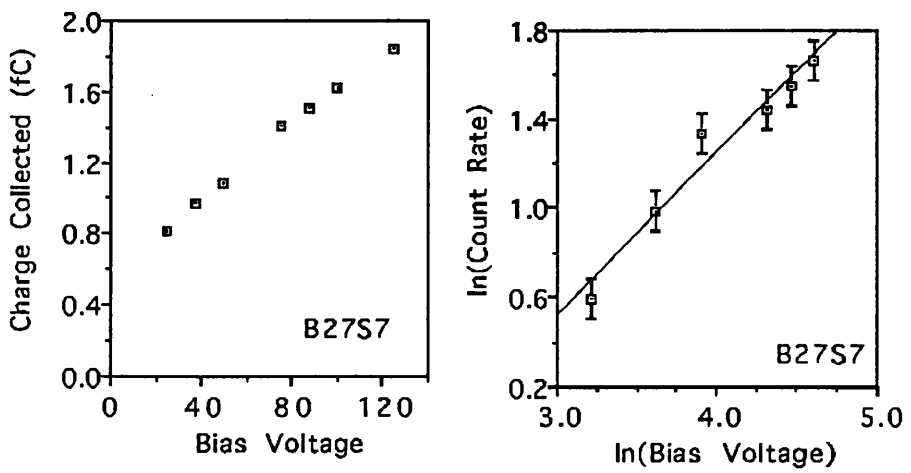

Figure 3.15: **Charge Collection for 60 keV Gamma Rays and Active Region Thickness Dependence on Bias for Batch 27 Sample 7**

voltage of 125V. A log-log plot of count rate versus bias (Fig.3.15) yielded a

voltage dependence of $V^{0.7\pm0.2}$.

The charge collection efficiency of Batch 28 Sample 3 is shown against bias voltage in Fig.3.16. Again, the rise seems to be linear and in agreement with the result from Batch 27. The best charge collection efficiency was 70 percent at 100V. Fig.3.16 shows that the count rate depends on $V^{0.8\pm0.2}$.

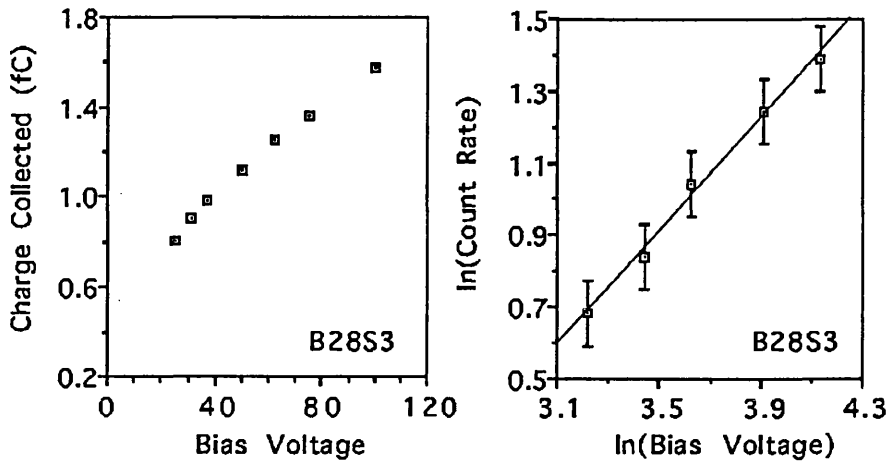

Figure 3.16: **Charge Collection for 60 keV Gamma Rays and Active Region Thickness Dependence on Bias for Batch 28 Sample 3**

Batch 57 Sample 2 (VB material) gave a charge collection efficiency which rose almost linearly with bias voltage (Fig.3.17); 48 percent efficiency was obtained at 125V. The count rate was found to depend on $V^{0.7\pm0.2}$, as shown in Fig.3.17. Batch 58 Sample 1 (Thermally treated LEC material) exhibited a charge collection efficiency which rose linearly with bias initially, to around 100V and then tailed off to give a maximum value of 97 percent at 300V bias (Fig.3.18). The count rate varied as $V^{0.8\pm0.2}$ (Fig.3.18).

By keeping the source to detector distance constant, it was possible to compare the active thicknesses of the detector types, taking into account the larger contact area of the Batch 58 devices. The count rate per unit contact area of the Batch 58 devices appeared to be slightly greater that of the rest around 100V; however the effect was little more than could be accounted for by experimental errors. The

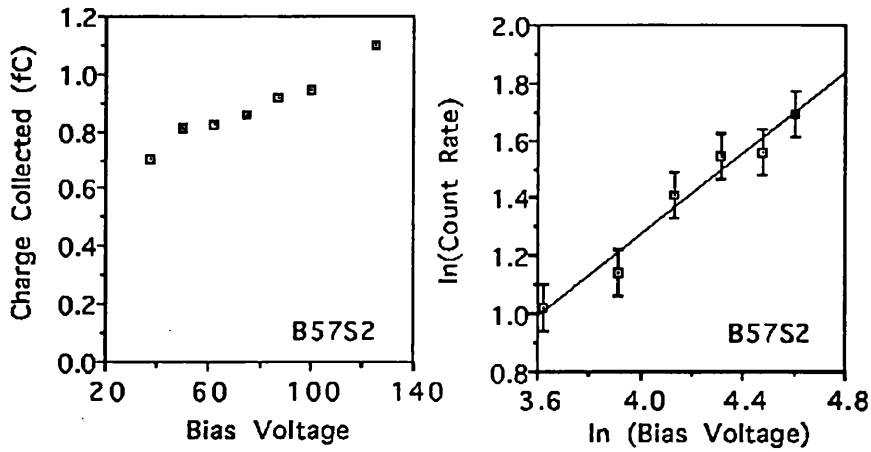

Figure 3.17: Charge Collection for 60 keV Gamma Rays and Active Region Thickness Dependence on Bias for Batch 57 Sample 2

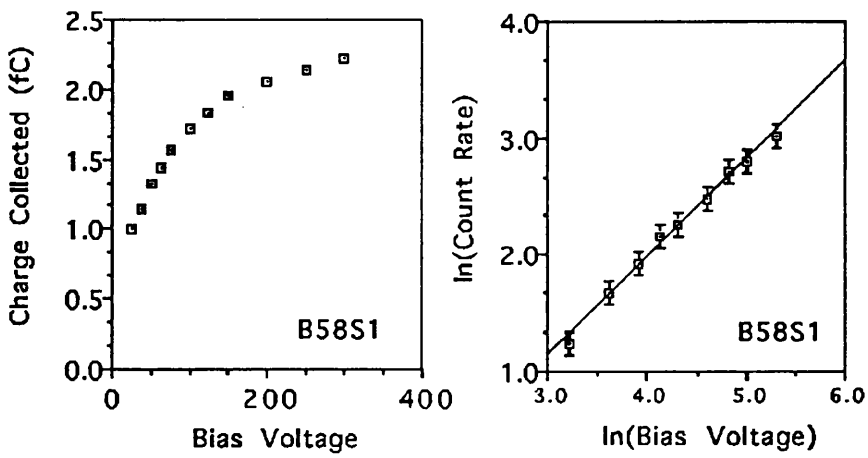

Figure 3.18: Charge Collection for 60 keV Gamma Rays and Active Region Thickness Dependence on Bias for Batch 58 Sample 1

maximum rate achieved for Batch 58 Sample 1 was higher than that achieved for the samples in the other batches, due to the higher voltage which it withstood before breakdown.

3.9 Devices from Other Institutions

Devices from other institutions have been tested in Glasgow. Those made by Alenia S.p.A. and by the Australian Nuclear Science and Technology Organisation (ANSTO) yielded particularly interesting results.

3.9.1 ANSTO Detectors

The ANSTO samples were made from a Liquid Phase Epitaxial layer grown on a heavily n-doped substrate. The ohmic contact was an aluminium layer, and the Schottky contact was gold, of diameter 2.2mm and deposited onto the freshly etched, unpolished, epitaxial surface. The free carrier concentration of the material was around $10^{14} cm^{-3}$, as reported by the supplier [4].

The leakage current of the device ANSTO 2.3 is shown in Fig.3.19; at 6.5nA at 100V reverse bias, this was almost an order of magnitude lower than that which is usual for LEC material. There appears to be a discontinuity at 14V. A log-log plot of current versus voltage showed two distinct, linear regions. The first, from zero to 14V, has a gradient of 0.4; theory predicts that the leakage current should increase as $V^{0.5}$ if generation current within the bulk dominates. Above 14V, the gradient of the plot increases to give a linear variation of current with bias. It can be seen, then, that the leakage current is dominated by surface effects at room temperature, a finding which has been reported for other ANSTO diodes tested by the makers [8]. For devices operated at room temperature, then, the leakage current might be reduced further by passivation.

The charge collection efficiency for alpha particles (Fig.3.20) was found to increase more rapidly with bias than has been found for LEC devices, reaching a plateau

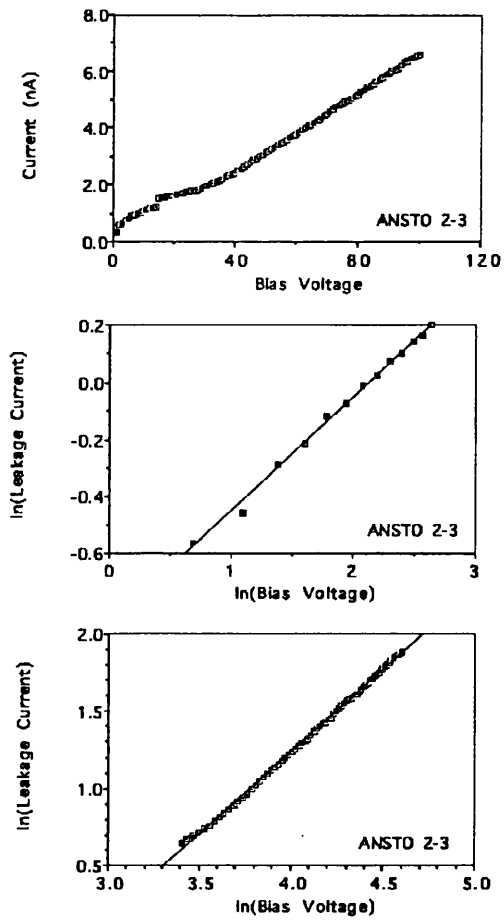

Figure 3.19: **Reverse Bias Current for ANSTO Detector. Upper: Overall Centre: Log-log Plot to 14 V Lower: Log-log Plot Above 14 V**

above 75V. It was necessary to perform this measurement in air, as the header on which the device was mounted was not compatible with the connectors on the vacuum vessel normally used. Thus, the exhibited charge collection efficiency of 90 percent represents collection of 100 percent of the charge liberated in the detector itself. From 20V upwards, the charge collection efficiency for 60keV gamma rays was 100 percent.

A log-log plot (Fig.3.21) of count rate versus bias for 60keV gammas gave a rate dependence on $V^{0.38\pm0.15}$; the device, being made of relatively defect-free material, behaved in a manner consistent with that predicted by the standard theory.

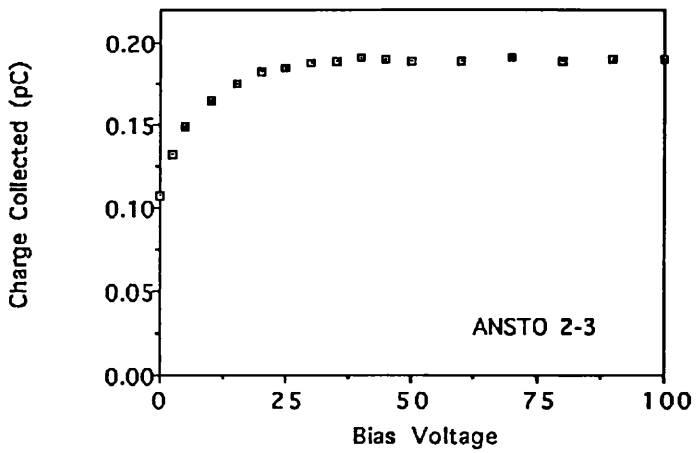

Figure 3.20: **ANSTO Detector Charge Collection for Alpha Particles.**

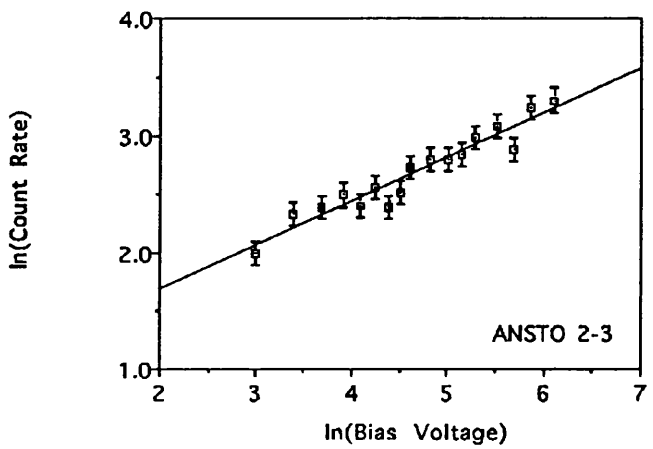

Figure 3.21: **ANSTO Detector Sensitive Depth Dependence on Voltage.**

3.9.2 Alenia Detectors

The Alenia detectors were made on Sumitomo LEC material. Alenia Sample 3 was 186 microns thick, and had four devices on one chip. The current-voltage characteristics of the detectors are shown in Fig.3.22; at 100V reverse bias, the average leakage current per unit contact area was $30nA/mm^2$, which is similar in magnitude to other LEC devices tested.

The charge collection efficiency (Fig.3.23) was found to rise slightly faster with

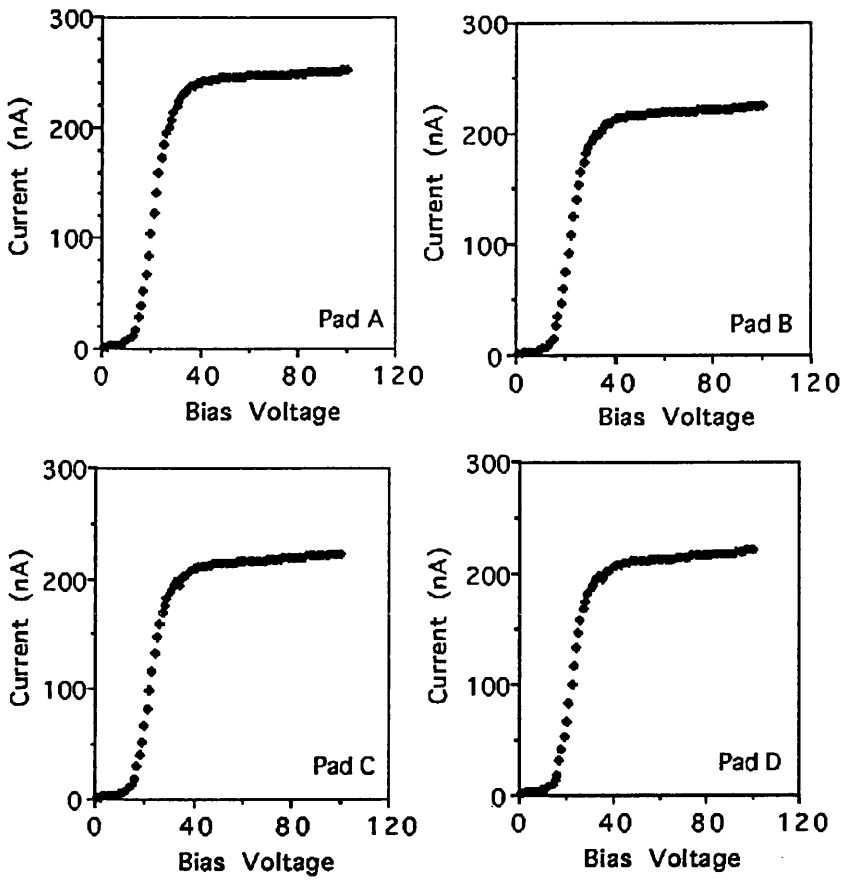

Figure 3.22: **Reverse Bias Currents for Alenia Detectors.**

applied bias volts than was usual for LEC devices, reaching a plateau of 77 percent from 100V to breakdown. Breakdown for three of the detectors occurred around 175V, whilst the fourth withstood nearly 300V. The devices were packaged in such a manner that it was possible to irradiate the back contact with alphas; spectra were recorded, but the charge collection efficiency was only 1 percent.

The device with the highest breakdown was selected for characterisation with 60keV gamma rays. The rise of charge collection was almost linear with applied voltage, reaching a maximum of 84 percent at 150V bias (Fig.3.24). The rise of gamma counting rate was found to follow $V^{1.2\pm0.2}$, close to the relationship for other LEC devices (Fig.3.25).

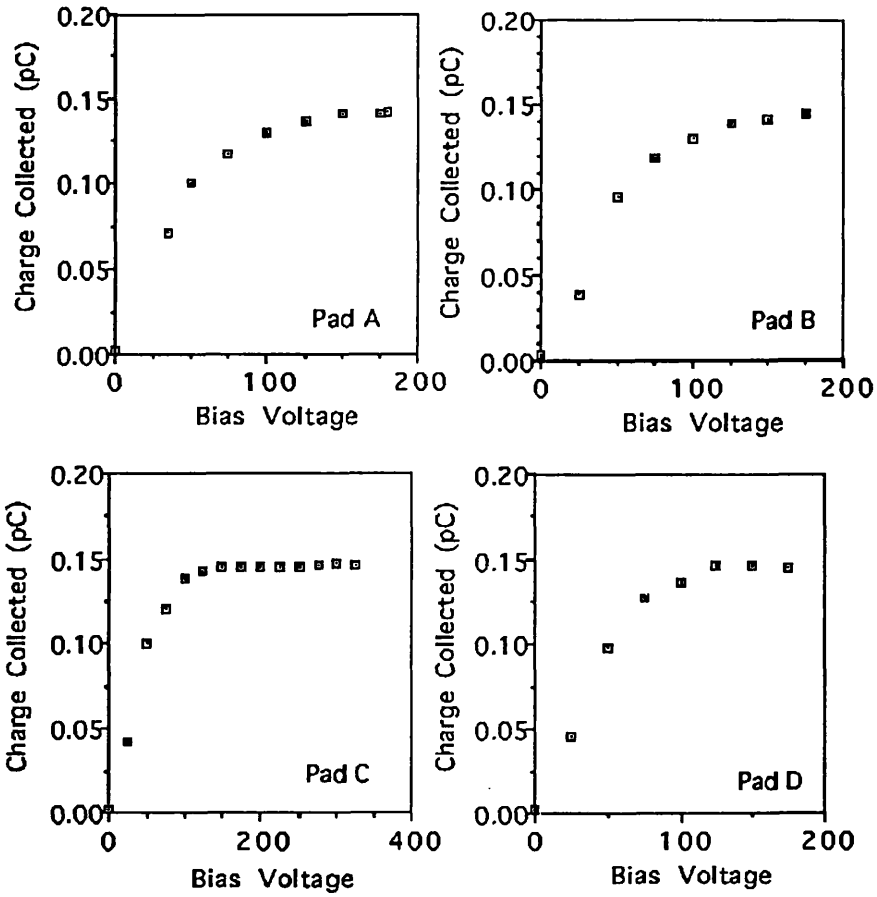

Figure 3.23: Alpha Particle Charge Collection for Alenia Detectors.

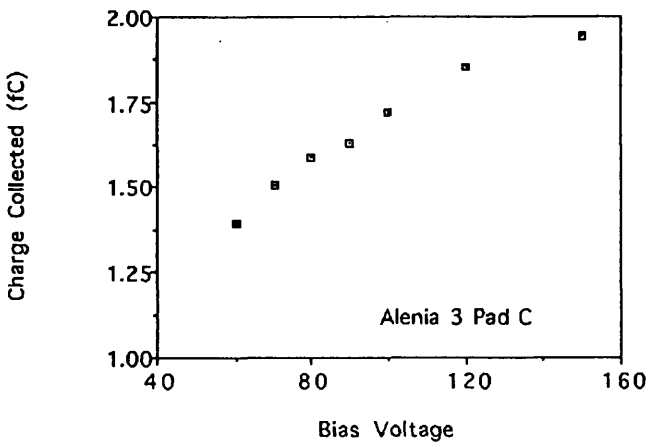

Figure 3.24: 60 keV Gamma Charge Collection for Alenia Detector.

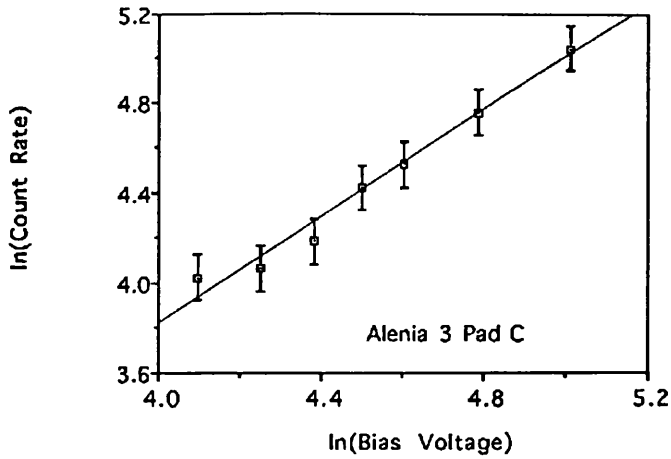

Figure 3.25: **Active Region Thickness Dependence on Voltage for Alenia Detector.**

3.10 Schottky-Schottky Detectors

For the standard type of contacts, used on the majority of detectors tested, the Schottky contact requires simpler processing than the ohmic contact, which must be annealed. The ohmic contact, in fact, does have associated with it a potential barrier, albeit one narrow enough to allow charge carriers to pass through by tunnelling. This leads to a current-voltage characteristic for the ohmic contact which is symmetric with the sense of the applied voltage. Devices were made with Schottky contacts on both faces, in the expectation that, since one contact is forward biased and one reverse biased, the overall behaviour of the detector should be similar to that of a Schottky-ohmic device, but quicker and easier to manufacture.

The first Schottky-Schottky devices were made on Wacker LEC material, one side being polished at the factory, the other at CERN [17]. Current-voltage characteristics were asymmetric, leakage current being better when the factory-polished face was acting as the rectifying junction. Charge collection efficiency was 35%, for alpha irradiation of the factory polished contact, and 15% for the CERN-polished contact. Both sides behaved well for the detection of beta

MIPs, charge collection efficiency reaching 62%. The asymmetries in the device behaviour were attributed to the effect of the surface preparation.

Commercial Schottky-Schottky devices have been made by Alenia. These work as detectors for bias of either sense, the charge collection efficiency increasing linearly with volage up to 80%. Devices were made 80, 200, and 300 microns thick; charge collection efficiency increased with voltage more rapidly the thinner the detector, up to breakdown. Breakdown occurred around 1V/micron, regardless of thickness.

3.11 Speed of Response

The speed of response of simple detectors 125 microns thick has been studied [11]. Devices were excited using 80ps laser pulses at the LENS Laboratory of the University of Florence, and the current pulses recorded using a 6GHz oscilloscope (Fig.3.27). Current pulses from protons and alpha particles were studied using a 500MHz oscilloscope (Fig.3.26). The pulses appear to have two components; a fast initial pulse being followed by a longer tail. Holes will play a greater part in the current transport for the case of protons, but details of the pulse are not well resolved because of the slower oscilloscope.

In view of what is known of the field distribution within LEC devices, the mechanism of pulse formation is likely to be quite complex. The effective doping concentration in the material will lead to very high fields close to the Schottky contact, which will be sufficient to promote electrons to the higher valley in the conduction band of gallium arsenide. There they will have higher effective mass and lower mobility. Thus, moving away from the Schottky contact, the drift velocity of the electrons will increase up to the maximum in (Fig.2.4), then decrease linearly and following the field distribution. Any model of pulse formation would also have to take account of the two regions of field predicted and the fact that carrier trapping might also play a part.

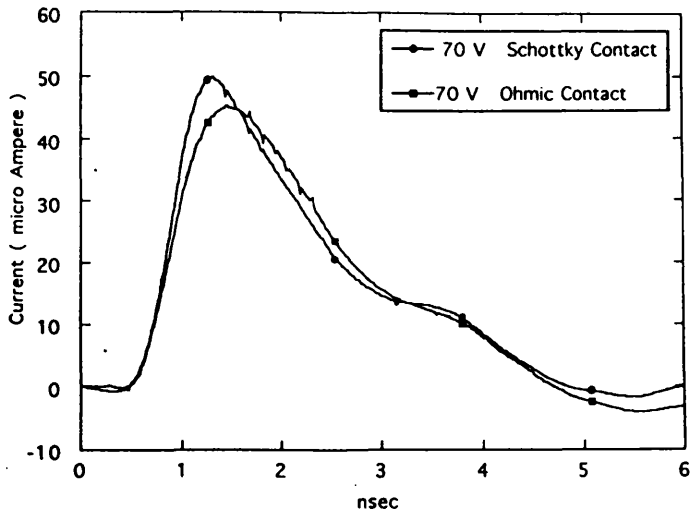

Figure 3.26: **500 MHz 'Scope Traces for 3 MeV Protons Incident on the Schottky and Ohmic Contacts of a GaAs Pad Detector (From [11])**

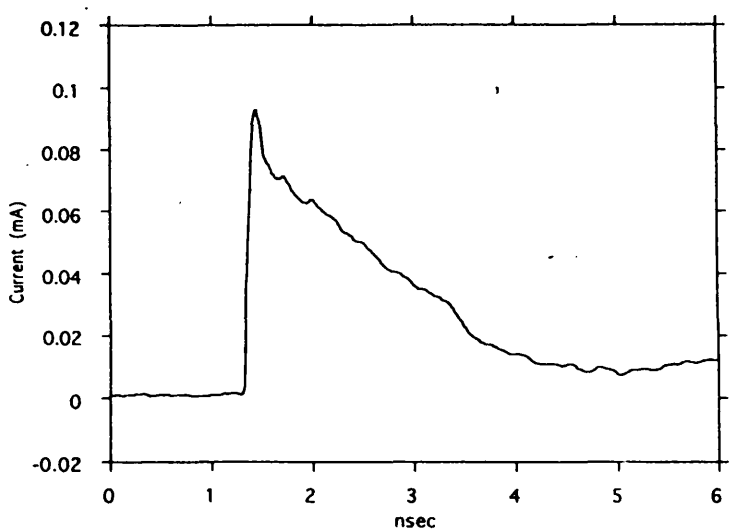

Figure 3.27: **6 GHz 'Scope Trace for Laser Excitation of a GaAs Pad Detector at LENS (From [11])**

3.12 Conclusions

Simple pad detectors have been fabricated on LEC semi-insulating substrate material, and have been tested with radioactive sources. The good separation of the signal peak from the noise pedestal for $60keV$ gamma rays indicates that microstrip devices for use at LHC should be more than adequate in terms of signal to noise ratio, despite higher leakage currents than silicon, and lower charge collection efficiencies.

Leakage currents appear to be due to generation centres at the surface of the devices; such generation centres may be due to surface damage below the Shottky contact, since the magnitude of the current appears to be affected by the quality of the surface polish. Passivation might be expected to reduce these surface currents. Charge collection efficiency for sources is also affected by the surface polish.

Charge collection efficiency is less than 100% due to a dead region in the detectors. This is due to field-dependence of the effective donor concentration in the SI material. The behaviour of the active region width with applied bias voltage departs from the $V^{1/2}$ dependence predicted by theory. LEC material annealed in order to improve its carrier lifetime did not appear to behave significantly better for application as a detector than standard material. Charge collection was sufficiently fast for use at LHC.

Semi-insulating material grown by the Vertical Bridgman process has been evaluated as a detector material, but the majority of samples tested have exhibited breakdown at significantly lower fields than LEC material.

The performance of epitaxially-grown devices is very good, with practically full charge collection efficiency and an active region thickness which exhibits a behaviour consistent with theory. Leakage currents are low, and are dominated by surface currents, indicating that they might be improved further by the use of

passivation. The signal peak for $20keV$ X-rays was well separated from the noise pedestal in spectra from epitaxial detectors at room temperature.

As yet, the LPE material is not available in large areas and has carrier concentrations which are higher than those desirable for detector construction. The VPE material is available only in layers which are thinner than those required. Thus LEC material, depsite its limitations, is the most likely candidate at present for use in the detection of MIPs.

References

[1] D'AURIA,S.,BERTIN,R. and DEL PAPA,C *Private Communication*

[2] BIERSACK,J.P. and ZIEGLER,J.F. *Transport and Ranges of Ions in Matter*

[3] GRUTER,K. et al. *J. Crystal Growth 94 (1989) 607*

[4] ALEXIEV,D. *Private Communication*

[5] KREMER,R.E. et al. *Journal of Materials Research Vol.5,No.7,July 1990*

[6] BROZEL,M.R. et al. *Proc. 5th. Conf. Semi-Insulating III-V Mats., Malmo, Sweden, pub. IOP,(1988),31*

[7] NORTHROP,D.C. et al. *Solid State Electronics Vol.7,No.17, 1964*

[8] ALEXIEV,D. and BUTCHER,K.S.A. *Nuclear Instruments and Methods A317 (1992)*

[9] BROZEL,M.R. *GaAs Detectors and Electronics for HEP (World Scientific,1992)*

[10] BERTIN,R. et al. *Nuclear Instruments and Methods A294 (1990)*

[11] BEAUMONT,S. et al. *Nuclear Instruments and Methods A322 (1992)*

[12] BEAUMONT,S. et al. *Nuclear Instruments and Methods A321 (1992)*

[13] RIDEOUT,V.L. *Solid State Electronics, Vol. 18, 541-550 (1975)*

[14] BRASLAU,N. *Synposium on Interfaces and Contacts, Boston, MA (1982)*

[15] EDWARDS,M. *GaAs Detectors and Electronics for HEP (World Scientific,1992)*

[16] MATHESON,J. *GaAs Detectors and Electronics for HEP (World Scientific,1992)*

[17] D'AURIA,S., *Private Communication*

[18] BERTIN,R. *Private Communication*

[19] KOBAYASHI,T. and TAKAYANAGI,S. *Nuclear Instruments and Methods 44 (1966)*

[20] EBERHARDT,J.E.,RYAN,R.D., and TAVENDALE,A.J. *Nuclear Instruments and Methods 94 (1971)*

[21] GIBBONS,P.E. and HOWES J.H. *IEEE Trans. Nucl. Sci. Vol.NS-19 No.3 (1972)*

[22] MARSH,J.H. *Private Communication*

[23] SZE,S.M. *Physics of Semiconductor Devices (Wiley)*

[24] RAMO,S. *Proceedings of the Institute of Radio Engineers, 27, 584 (1939)*

[25] McGREGOR,D. et al. *IEEE Transactions on Nuclear Science, in press.*

Chapter 4

Radiation Damage in Detectors

4.1 Damage Mechanisms in Silicon Detectors

The interaction of incident particles with the semiconductor material of which a particle detector is made leads to ionisation in the first instance; this is desirable as it gives rise to the charge collected and allows particle detection, although in devices other than particle detectors this type of ionisation may be undesirable. Deleterious processes in detectors are of a longer term nature and fall into two types. These are long-term ionisation effects and displacement effects [1].

Displacement effects are due to collisions between incident particles and the atoms of the semiconductor material; such collisions may impart enough energy to an atom to displace it from its lattice site, forming point defects. Point defects are typically produced by high energy photon or electron irradiation. Displaced target atoms may then collide with other atoms in the crystal, forming clusters of disorder in the structure of the material. Such damage clusters are produced by nuclear interactions of nucleons. Detailed damage mechanisms are affected by the presence of dopant or impurity atoms. Point defects have associated with them levels in the forbidden band which can act as generation-recombination centres or can change the effective donor concentration in the device. Damage clusters have associated with them many closely spaced levels in the forbidden band. After

damage has occurred in the material, defects undergo thermal diffusion; this may result in a spontaneous amelioration of the damage, known as annealing. Subsequently, only the thermally stable defects remain. Gallium arsenide has been found to be more radiation hard than silicon due to the larger mass of the target atoms and rapid recombination of vacancy-interstitial pairs on the gallium sublattice [2].

Long-term ionisation effects are due to the trapping of ionisation charges in insulating layers. Such layers may contain large concentrations of trapping levels; electron-hole pairs due to an incident ionising particle will tend to recombine, to drift out of the insulator under an applied field, or to be trapped. Charges trapped on shallow levels are thermally excited from them until they either leave the insulator or are trapped on deep levels. The wide band gap associated with insulators makes release of charges trapped on deep levels unlikely. Thus, charges can build up within the insulator; if such an insulator is adjacent to the active region of a device, the electric field within that device will be altered and its behaviour may deteriorate. In particular, if the charge within the insulator is sufficient, the field in the adjacent semiconductor may become high enough to cause avalanche breakdown. New levels will also be introduced to the semiconductor band gap at the semiconductor-insulator interface.

One of the most important long-term ionisation effects for silicon devices is the build up of positive charge due to hole trapping at the interface between the silicon and the passivating silicon dioxide. In the case of gallium arsenide, oxide layers are less frequently used in device construction. A stable oxide cannot be grown on gallium arsenide, so that silicon dioxide or silicon nitride must be used for passivation or insulation. This requires more complex processing than does the growth of oxide layers on silicon wafers.

4.2 Damage Studies on Silicon Detectors

4.2.1 Leakage Current Behaviour

The most immediate effect of irradiation of silicon microstrips has been found to be a linear rise in the reverse leakage current with particle fluence, as defect levels close to the centre of the band gap are created. This rise is represented by the damage constant α, according to:

$$I = I_o + \alpha\phi \tag{4.1}$$

where I_o is the leakage current per unit volume before irradiation, I is the leakage current per unit volume after irradiation and ϕ is the fluence of particles through the device [3]. The damage constant is dependent on the type of particle used for the irradiation, the energy of the particles used, the initial resistivity of the material, and the biasing conditions used. For silicon detectors, the most damaging particles are neutrons, which typically give a damage constant of $1 \times 10^{-16} Acm^{-1}$ [6] (see Fig.4.1). From the graph, it can be seen that beyond a neutron fluence of $\sim 10^{13} cm^{-2}$, the rise in leakage current is faster than would be expected at lower fluences. The reason for this is not clear.

Neutron sources at different institutions use several different nuclear reactions, resulting in different energy spectra. The energy spectrum for neutrons at LHC is expected to peak around 1MeV [13], so that results must be corrected according to the source used. The damage constant α has been shown to have the same energy dependence as the displacement cross-section for silicon [14], as would be expected if the increase in bulk generation current with irradiation is primarily due to displacements from the lattice. The displacement cross-section has thus been used to provide a scaling parameter for the energy dependence of the leakage current.

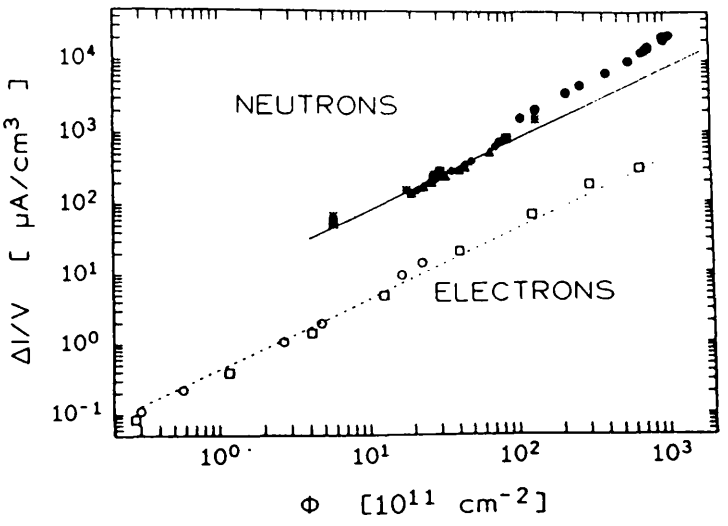

Figure 4.1: **Increase of Reverse Bias Current at total Depletion vs. Fluence for** $6.2MeV$ **Neutrons and** $1.8MeV$ **Electrons (Corrected for Self-Annealing) From [5]**

As has been mentioned, after irradiation has taken place, the degradation of the device may recover to some extent, over a period of days. In order to be able to predict device behaviour at LHC, where detectors will be irradiated during beam time and will undergo annealing in the periods where there is no beam, the long term annealing behaviour of the leakage current has been studied [14]. Irradiations have been performed using sources giving neutron fluxes $\sim 10^7 cm^{-2}s^{-1}$, which allow short exposure times to be used, minimising the effect of self-annealing during the exposure. The long term evolution of the device leakage currents has been monitored after such irradiations, and their decrease parametrized according to:

$$\frac{\Delta I(t)}{\Delta I(0)} = \sum_{i=1}^{5} A_i \,.\, exp^{-t/\tau_i} \tag{4.2}$$

where $\Delta I(0)$ is the increase in leakage current per unit volume in the absence of annealing, $\Delta I(t)$ is the observed increase in leakage current per unit volume at time t following irradiation and represents the effect of several separate processes,

each resulting in an exponential decay of the leakage current increase with time. The amplitudes A_i and time constants τ_i were chosen to give the best achievable fit to the data and are given, for example, in [6],[5] and [9]. This equation has then been used to correct calculated values of α for the effect of annealing (Fig.4.2).

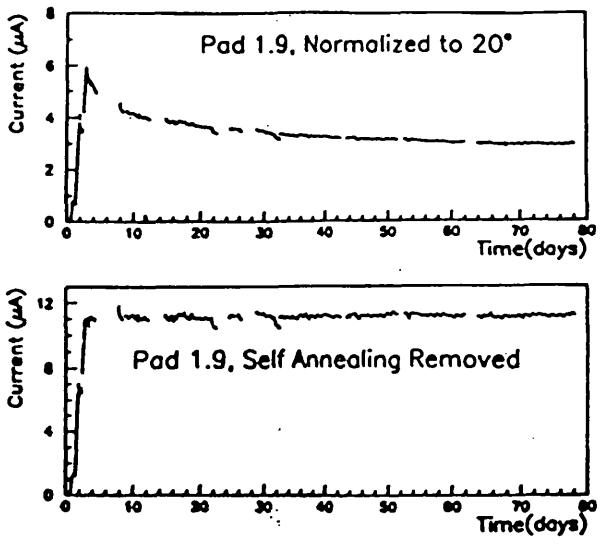

Figure 4.2: **Leakage Current During and After Irradiation Showing Correction for Self-Annealing (From [6])**

4.2.2 Doping Density Behaviour

A further effect of irradiation is to change the effective doping concentration in the material. This has been modelled in terms of two processes [5]. Assuming an initially n-type material, the first process is the removal of active phosphorus donors. The rate of removal will be proportional to the number of active donors N_d present:

$$\frac{dN_d}{d\phi} = -c \cdot N_d(\phi) \tag{4.3}$$

where c is a constant. The second process is the creation of the stable divacancy defect, which acts as an acceptor. The number of such defects created N_{ve} will rise linearly with fluence:

$$\frac{dN_{vv}}{d\phi} = b \tag{4.4}$$

where b is a constant. Thus, the overall effective doping concentration after a fluence ϕ will be given by:

$$N_{eff}(\phi) = N_{do}\, exp^{-c\phi} - N_{ao} - b\phi \tag{4.5}$$

where N_{do} and N_{ao} are the unirradiated donor and acceptor concentrations, respectively. The constants have been determined in several studies; values of $3.5 \times 10^{-13} cm^{-2}$ for c and $0.08 cm^{-1}$ for b are representative [5]. As the donor concentration decreases, the voltage required to deplete the detectors decreases, until the material reaches type inversion. At this point, the effective doping concentration has changed sufficiently that the material becomes p-type and depletion starts from the opposite side of the device (see Fig.4.3). This has been found to occur at a fluence of $\simeq 2 \times 10^{12} cm^{-2}$ [5],[8]. Thereafter, further irradiation causes the material to become more heavily p-type; the depletion voltage increases until breakdown occurs before depletion, at which point the device is no longer useable.

Type inversion has been studied in detail by several groups, who have obtained the effective doping concentration from the depletion voltage of the device, according to equation (2.73). The depletion voltage itself was extracted experimentally by measuring the minimum detector capacitance. That the side from which depletion begins changes from the junction side to the back side after type inversion has been verified in [1], where an inverted detector was biased to less than its depletion voltage and illuminated with an alpha source. The field within the device was sufficient to separate efficiently the charges due to the alphas only on the side of the device from which depletion began, allowing identification of that side. A similar demonstration was performed in [16], where an infra-red LED was used

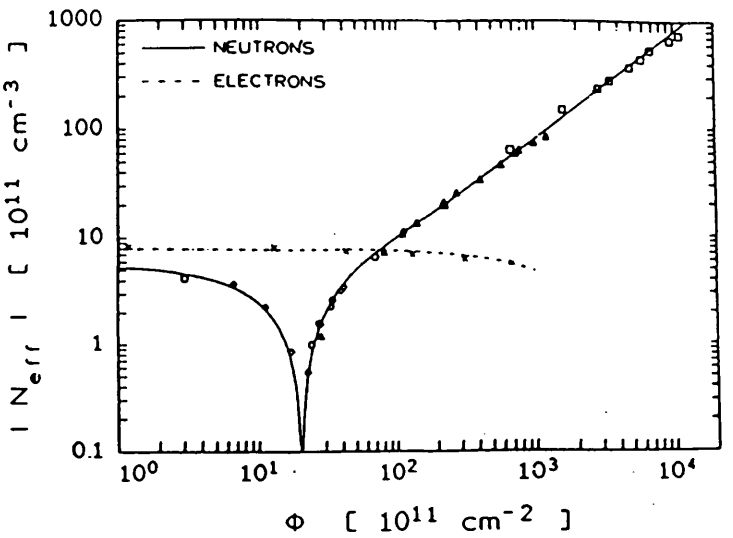

Figure 4.3: **Effective Dopant Concentration vs. Fluence for Neutrons and Electrons Corrected for Self Annealing (From [5])**

which had a penetration depth of $\sim 30\mu m$ into the silicon.

The effective doping concentration and the side from which depletion begins have also been deduced from current pulse shape measurements [9]. An alpha source was used to deposit charge at the surface of the detector, and the evolution of the hole current with time recorded. In the absence of trapping phenomena, the current through the device will be simply the number of carriers multiplied by their velocity, multiplied by the electronic charge. The carrier velocity is related to the field at any point within the device by equation 2.36 and the field itself will depend on the effective doping concentration. The effective doping concentration was calculated according to:

$$N_{eff} = \frac{\epsilon_o \epsilon_r}{q\mu_h(t_2 - t_1)} \cdot ln\frac{i(t_2)}{i(t_1)} \tag{4.6}$$

where t_1 and t_2 are two points in time during the plateau of the current pulse. The sign of the gradient of the current pulse gives the direction of the field within the device and thus the side from which depletion begins. This expression follows

directly from equation (2.105).

As with the time evolution of the leakage current, the effective doping concentration has been found to undergo annealing with time. The resulting decrease of acceptor concentration with time has been parametrized [11] by use of:

$$\frac{\Delta N_{eff}(t)}{\Delta N_{eff}(0)} = \sum_{i=1}^{6} A_i \, . \, exp^{-t/\tau_i} \tag{4.7}$$

in an analogous manner to the parametrization of the leakage current annealing (Fig.4.4). However, it has been observed in some instances [16],[1] that, after the initial annealing, the depletion voltage of the device begins to rise. This process appears to begin a few weeks after the irradiation and the depletion voltage then continues to rise for several months (Fig.4.5). It is possible that the effect is due to the recombination of vacancies; over a long time-scale, stable divacancies are formed which act as acceptors.

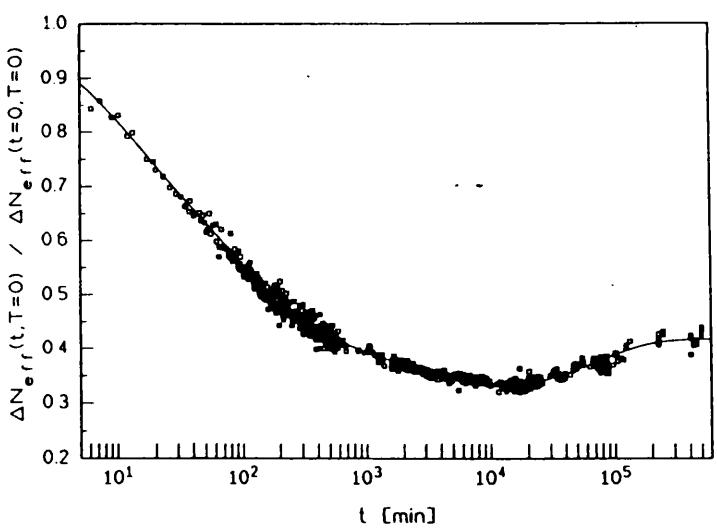

Figure 4.4: **Room Temperature Annealing of Relative Dopant Concentration After Neutron Damage (from [5])**

In addition to the effects of uniform irradiation on the doping concentration of devices, it has been found [3] that for a detector subjected to non-uniform

irradiation across its area, the resultant changes in doping concentration produce a non-uniform electric field within the device, which leads to systematic errors in the determination of particle trajectories.

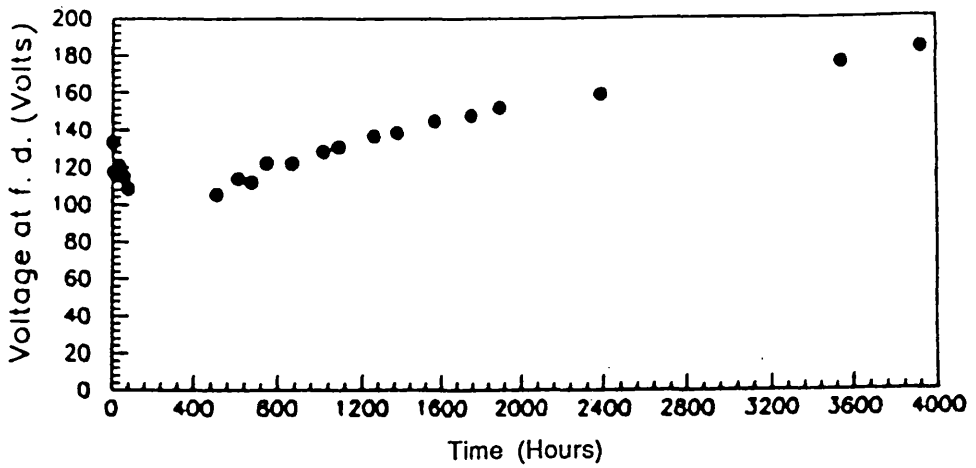

Figure 4.5: Depletion Voltage vs. Time After Neutron Irradiation (From [9])

4.2.3 Charge Trapping

High levels of irradiation may also lead to an increase in charge trapping. A proportion of the charge liberated in the device by an incident ionising particle may be trapped on defect levels. This may be permanent, or the charge may subsequently be released. Charge collection efficiency is reduced [11],[5],[1] and charge collection time is increased [1]. The degradation of the material is characterised in terms of the decrease in carrier lifetimes according to:

$$\frac{1}{\tau_e} = \gamma_e \cdot \Phi \quad \text{and} \quad \frac{1}{\tau_h} = \gamma_h \cdot \Phi \tag{4.8}$$

where the constants γ may be obtained experimentally by using alpha particles on each side of a detector to separate the electron and hole contributions. The

charge collection deficit is then measured and the calculated transit time of each carrier used to yield the carrier lifetimes. After a neutron fluence of $10^{14}cm^{-2}$, the charge collection efficiency of a detector for relativistic electrons has been measured [1] to be $\sim 70\%$ for an integration time of $10ns$. The effects of carrier trapping may be lessened by applying a higher bias voltage across the detector, where the breakdown voltage of the device will allow this.

4.2.4 Irradiation of Integrated Components

Structures such as MOS capacitors and polysilicon resistors which are often integrated onto the detector itself have been irradiated. Coupling capacitors have been neutron irradiated [10] and photon irradiated [17], and have been found not to change significantly in their behaviour. Polysilicon bias resistors have been shown to be stable under neutron irradiation, but have been found to exhibit an increase in their resistance of around 15% at $0.2MRad$ gamma irradiation. This increase is due to the introduction of fixed charges into the oxide below and above the resistors; this causes a partial depletion of the polysilicon. Above $0.2MRad$, the resistor values remained stable. The change in the resistor values is not in itself a problem; however if adjacent bias resistors were to exhibit sufficiently different resistances, the potential difference between strips might become enough to break down the interstrip resistance of a detector, resulting in the shorting of strips together. This interstrip resistance is in any case lessened and breakdown thus made more likely by neutron irradiation. Even with identical bias resistors, differences between the leakage currents of adjacent strips could cause similar interstrip potential differences. These effects would clearly be exacerbated for non-uniform irradiation conditions.

4.3 Detector Survival at LHC

The dose levels and neutron fluences expected in the various components of the ATLAS detector are shown in the table below [12]. A comparison of the neutron fluences with and without the use of a moderator is included.

Table 4.1: Peak Doses and Neutron Fluences per Year (Assuming $10^7 s$ Running per Year at $10^{34} cm^{-2} s^{-1}$ Luminosity)

Component	Dose (kGy)	Fluence (cm^{-2}) with moderator	Fluence (cm^{-2}) no moderator
SITV	28	6.0×10^{12}	2.5×10^{13}
SIT	1.6	1.9×10^{12}	1.9×10^{13}
End Cap TRDs	4.0	3.4×10^{12}	2.8×10^{13}
Barrel EM Cal	0.4	6.8×10^{12}	1.7×10^{13}
Barrel Hadron Cal	0.02	1.0×10^{12}	1.4×10^{12}
End Cap EM Cal	21	8.2×10^{13}	9.1×10^{13}
End Cap Had Cal	4.0	4.0×10^{13}	5.1×10^{13}
Forward Cal	830	1.1×10^{15}	

It can be seen that the tracking devices receiving the highest levels of damage are those in the SITV. Without the moderator, typical silicon detectors in this area would be expected to undergo type inversion after approximately one month of running at full luminosity, and be reaching the end of their life within four years. With a moderator to reduce the flux of albedo neutrons reaching the central cavity, the detectors might be expected to invert after a few months' running. The flux of charged particles increases approximately as $1/r^2$ towards the beampipe, as well as becoming larger with distance towards the forward region. For gallium arsenide wheels in the forward region,as outlined in the introduction, the flux of charged particles might be expected to exceed $10^{14} cm^{-2}$, based on results presented in [18], in addition to neutron fluences of $\sim 10^{13} cm^{-2} y^{-1}$. The charged particle flux will be non-uniform radially across the surface of the wheels, exacerbating the problems due to the radiation damage.

It is expected that cooling will be provided for all the silicon detectors; since

their leakage current varies exponentially with temperature, cooling will increase the signal to noise ratio of the devices during irradiation. Further, as leakage currents increase, it will be necessary to remove the heat generated within the detector. The cooling systems required will increase the mechanical complexity of the detector and also the amount of scattering material within the central cavity.

In an attempt to prolong the lifetime of detectors in the SITV, the inner layer of the vertex detector will consist of pixel detectors. The smaller the element size for a detector, the greater its signal to noise ratio due to the smaller leakage current, and hence the higher the leakage current per unit area may become after irradiation without its associated shot noise swamping the signal. However, for this strategy to succeed, it must be assumed that the detectors will withstand a sufficiently high bias voltage to become depleted, which will require the use of guard rings and similar techniques in an effort to prevent breakdown. The use of small pixels to increase the post-irradiation signal to noise ratio in this way will also lead to a requirement for more readout electronics to serve the increased number of individual detector elements. This in turn will place greater demands on the mechanical support structures and on the cooling system in particular, since the readout electronics tend to dissipate more heat than the detectors themselves.

It is intended that the detectors will be operated with cooling during data-taking periods of 100 days each. This will minimise the effect of leakage currents during running; however studies of detectors operated at $-20^{o}C$ and at $20^{o}C$ [8] have shown that annealing processes are slowed to a negligible level at low temperature. Thus, at low temperature, the performance of the silicon will become degraded more quickly. In order to make use of self-annealing, the detector will remain at room temperature during those times in which data taking is not taking place, which are expected to total 265 days per year. The evolution of depletion voltage and leakage current for such a scenario is shown in Fig.4.6 and Fig.4.7. The depletion voltage would not, however, be expected to behave in this way if there

was significant long-term reverse annealing. In this case, the resulting rise in depletion voltage could severely shorten the lifetime of the detectors. Reverse annealing is not as yet well understood, and will require further investigation.

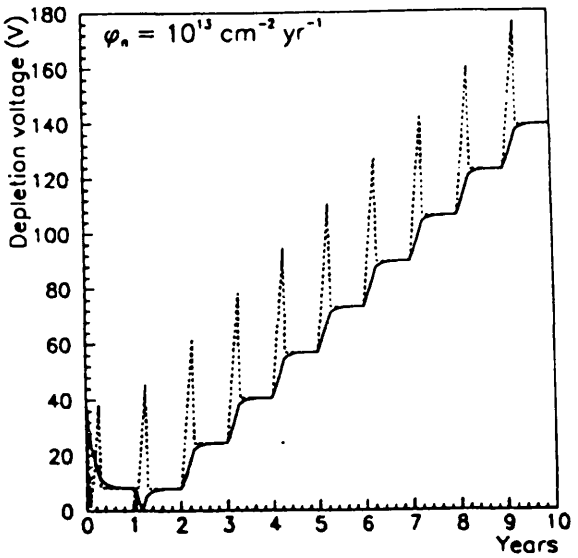

Figure 4.6: Predicted Depletion Voltage for 10yr. LHC Operation. Solid line-irradiation and annealing at $+20°C$. Dotted line-irradiation at $-20°C$ and annealing at $+20°C$. (from [8])

Thus, the present state of the art in silicon detectors is presented with a difficult technical problem if such devices are to be used in those areas of LHC detectors where radiation levels are highest. The response of such devices to neutrons is now well understood, but further work is planned by several groups on the response to charged particles. More work is also required in order to understand the reverse annealing process, which appears to have taken place in some studies but not in others. There is also reason to believe that synergistic effects may occur between neutron and charged particle irradiation, which might lead to higher rates of damage than expected. Finally, in a real situation, non-uniform irradiation across devices would lead to a greater degradation in performance than have the uniform irradiations used in most studies. As a precaution, the vertex detector has been

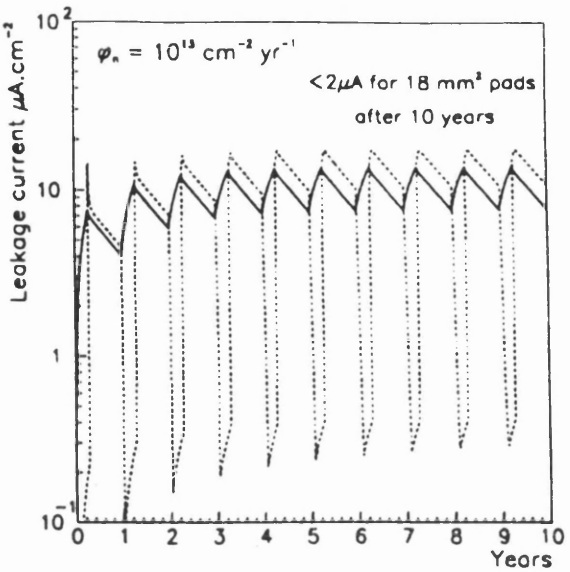

Figure 4.7: **Predicted Leakage Current as for the Previous Figure. (from [8])**

designed for easy removal or replacement. In the forward region of the ATLAS detector, the proposed gallium arsenide detector wheels will receive similar doses and neutron fluxes to the vertex detector; in addition, the charged particle dose will be non-uniform. Gallium arsenide tracking detectors must therefore exhibit adequate performance after radiation exposures of $10 MRad$ gamma or a neutron fluence of $10^{14} cm^{-2}$ if they are to play a significant part at LHC.

4.4 Radiation Hardness of GaAs Detectors

4.4.1 Glasgow Detectors

The primary reason for the study of gallium arsenide detectors being the expectation of greater radiation hardness than silicon, devices have been exposed to 20 MRad gamma irradiation, using ^{60}Co gamma rays at the Scottish Universities Research and Reactor Centre, and up to 2×10^{15} neutrons per cm^2 at the ISIS facility of Rutherford Appleton Laboratory. The energy spectrum of fast neutrons at ISIS is approximately that expected for the LHC [4]. Results for simple pad-type structures are presented here, whilst results for microstrip devices will be presented in the next chapter.

The gamma-irradiated devices showed little change, either in leakage current or in charge collection efficiency; pulse height spectra for alpha particles of a Batch 28 sample are shown (Fig.4.8). These were devices of the same type as described in the previous chapter, and were exposed to $20MRad$ at SURRC.

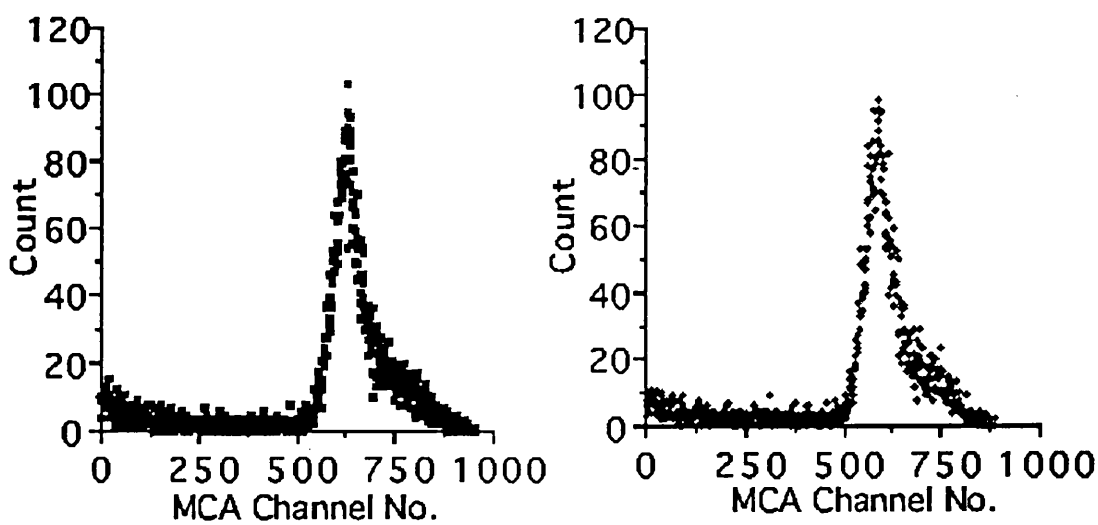

Figure 4.8: **Alpha Spectra from B28S4 Before (left) and After (right) Irradiation.**

As has been seen, the dominant effect in the reduction of the signal to noise ratio

by irradiation of silicon detectors is the rapid increase of reverse bias current, the linear increase in current per unit device volume per unit fluence being denoted by the damage coefficient, α. The reverse bias current-voltage characteristics of two standard Glasgow simple pad detectors are shown in Fig.4.9, before and after neutron irradiation. The device B21S2 was exposed to a neutron fluence of $9.7 \times 10^{14} cm^{-2}$, whilst B20S6 received $1.9 \times 10^{15} cm^{-2}$. In both cases, the increase in leakage current is very small compared to that which would be expected from silicon devices.

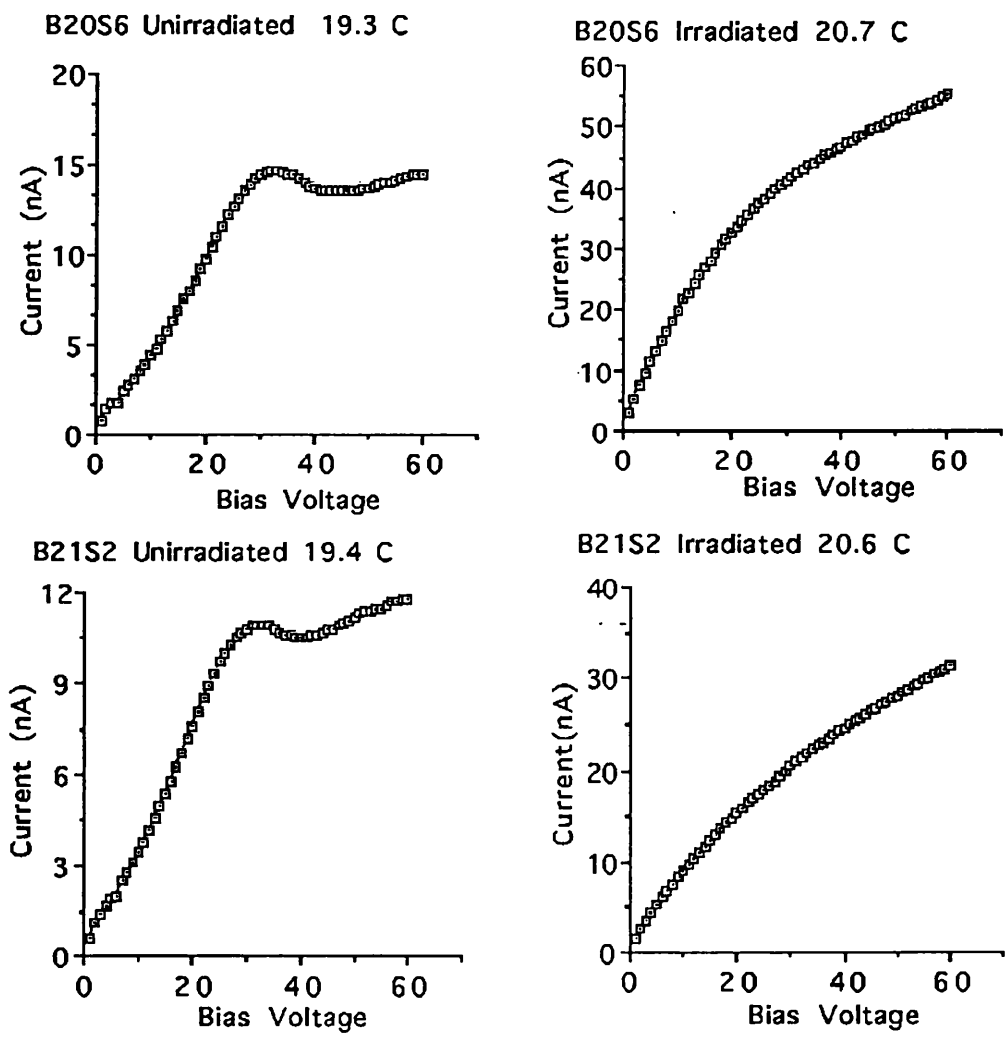

Figure 4.9: Leakage Currents of B20S6 and B21S1 Before (left) and After (right) Irradiation.

Alpha particle pulse height spectra for the device B21S2 before and after irradiation are shown in Fig.4.10; clearly the charge collection efficiency has fallen.

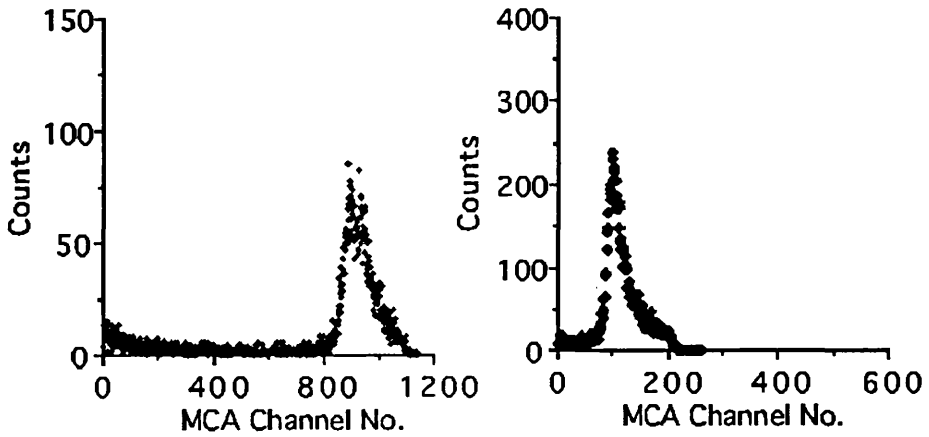

Figure 4.10: **Alpha Spectra from B21S2 Before (left) and After (right) Irradiation.**

The dominant effect in the degradation of gallium arsenide detectors by neutron irradiation appears to be such a fall in charge collection efficiency, in contrast to that which has been seen for silicon devices. The alpha particle pulse height is shown versus neutron fluence is shown in Fig.4.11 for a series of Glasgow simple devices of the same type irradiated at RAL [7].

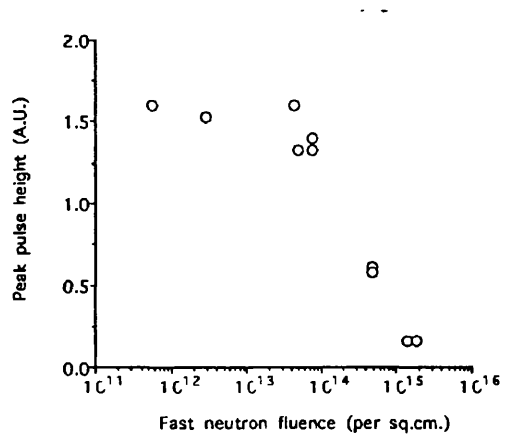

Figure 4.11: **Charge Collection for Alphas vs. Fast Neutron Fluence**

It can be seen that the charge collection efficiency begins to fall above a neutron fluence of $10^{14} cm^{-2}$, where the fluence figure refers to neutrons with energy above 10keV, which are believed to be the most damaging to semiconductor crystals. Despite the drop in charge collection efficiency, the peak separation from the pedestal for minimum ionising particles is still very good, as shown in Fig.4.12, in which pulse height spectra before and after irradiation are shown for a simple device exposed to minimum ionising betas from a ^{106}Ru source.

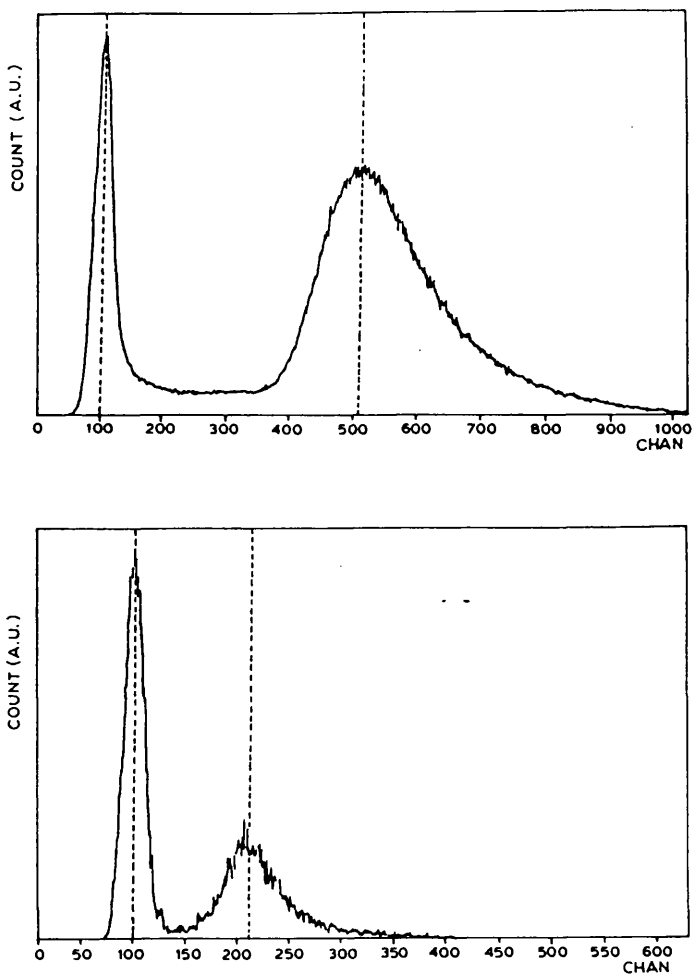

Figure 4.12: **MIP Spectra from Simple Device Before and After Irradiation (From 7).**

This indicates that a full detection efficiency would be achieved for gallium

arsenide devices used in tracking applications at future collider experiments, even after such a neutron fluence. Results for beam testing of Glasgow-fabricated gallium arsenide microstrip detectors are shown in the next chapter.

4.4.2 Alenia Detectors

The devices made by Alenia SpA and tested in the previous chapter exhibited a particularly good performance, especially in terms of charge collection efficiency, which reached 77% for alphas and 84% for gammas, for a $187\mu m$ thick device. It is believed that this is due to the criteria used by Alenia to select gallium arsenide wafers for the manufacture of integrated circuits. It is hoped that Alenia microstrip devices will be beam tested in due course.

Two Alenia chips, each bearing four simple detectors, were neutron irradiated at RAL, in order to examine their radiation hardness. The first, $212\mu m$ thick, received a fast neutron fluence of $2.9 \times 10^{13} cm^{-2}$, whilst the second, $305\mu m$ thick, received a fluence of $7.3 \times 10^{13} cm^{-2}$. These two chips are referred to as Alenia 1 and Alenia 2, respectively.

Alenia 1

Reverse bias current-voltage characteristics after irradiation of the four Alenia 1 pads are presented in Fig.4.13. These may be compared to the similar unirradiated sample for which results were presented in the previous chapter. There is little difference in the magnitude or shape of the current-voltage curves for the two sets of samples.

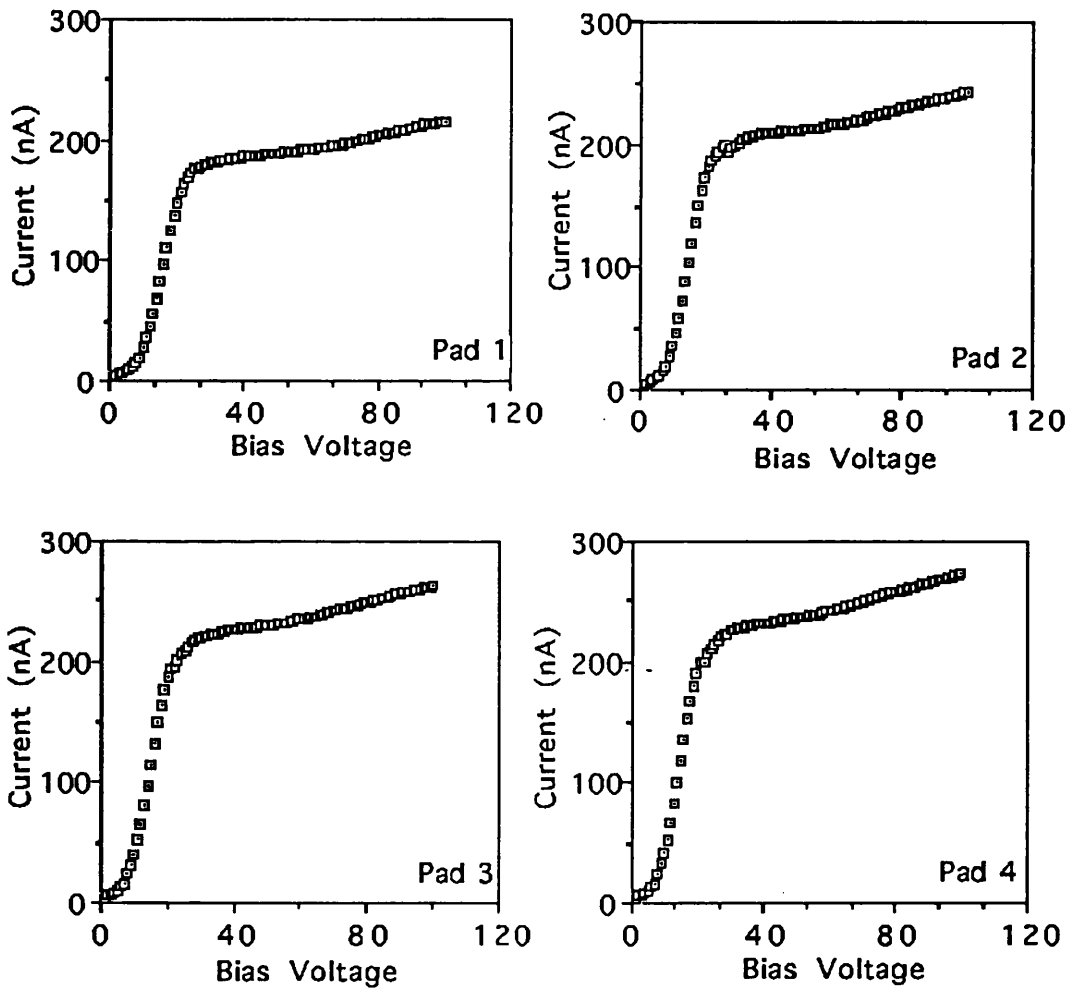

Figure 4.13: Alenia 1 Leakage Currents after Irradiation.

Fig.4.14 shows the charge collection efficiencies of the Alenia 1 pads versus applied bias voltage, for ^{241}Am alpha particles. The charge collection efficiency for the pads reaches 70%. The maximum voltage which could be applied to the devices

appears to have risen.

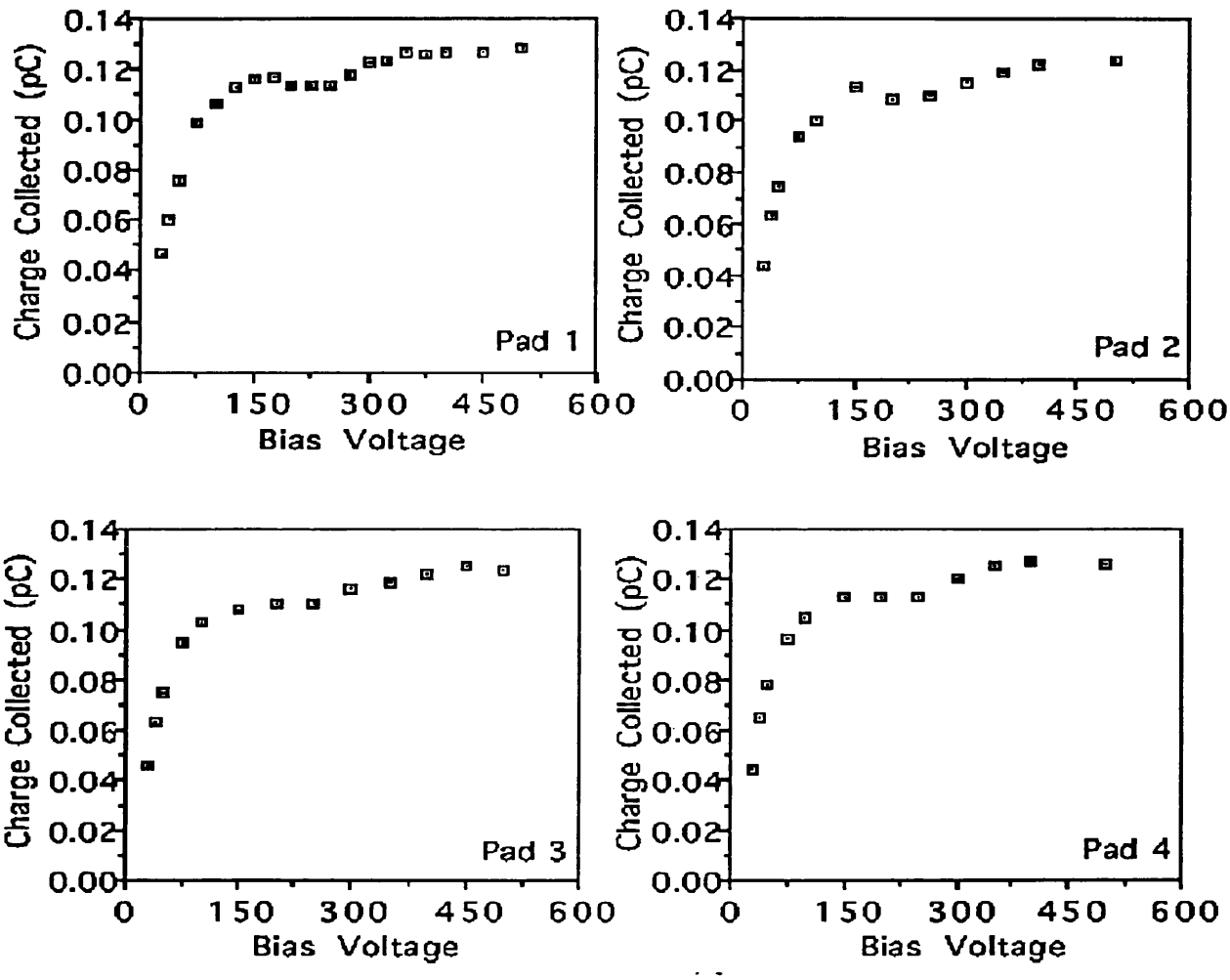

Figure 4.14: **Charge Collection for Alphas from Alenia 1 After Irradiation.**

Fig.4.15 shows the charge collection efficiencies of the Alenia 1 pads versus bias for $60keV$ gammas. The charge collection efficiency reaches 65%. A rate measurement with the same gamma source indicated that the active thickness exhibited a linear rise with voltage, as seen for unirradiated devices on LEC material.

The Alenia devices were also tested post-irradiation with minimum ionising betas. A collimated ^{90}Sr source was used, the detectors being placed between the

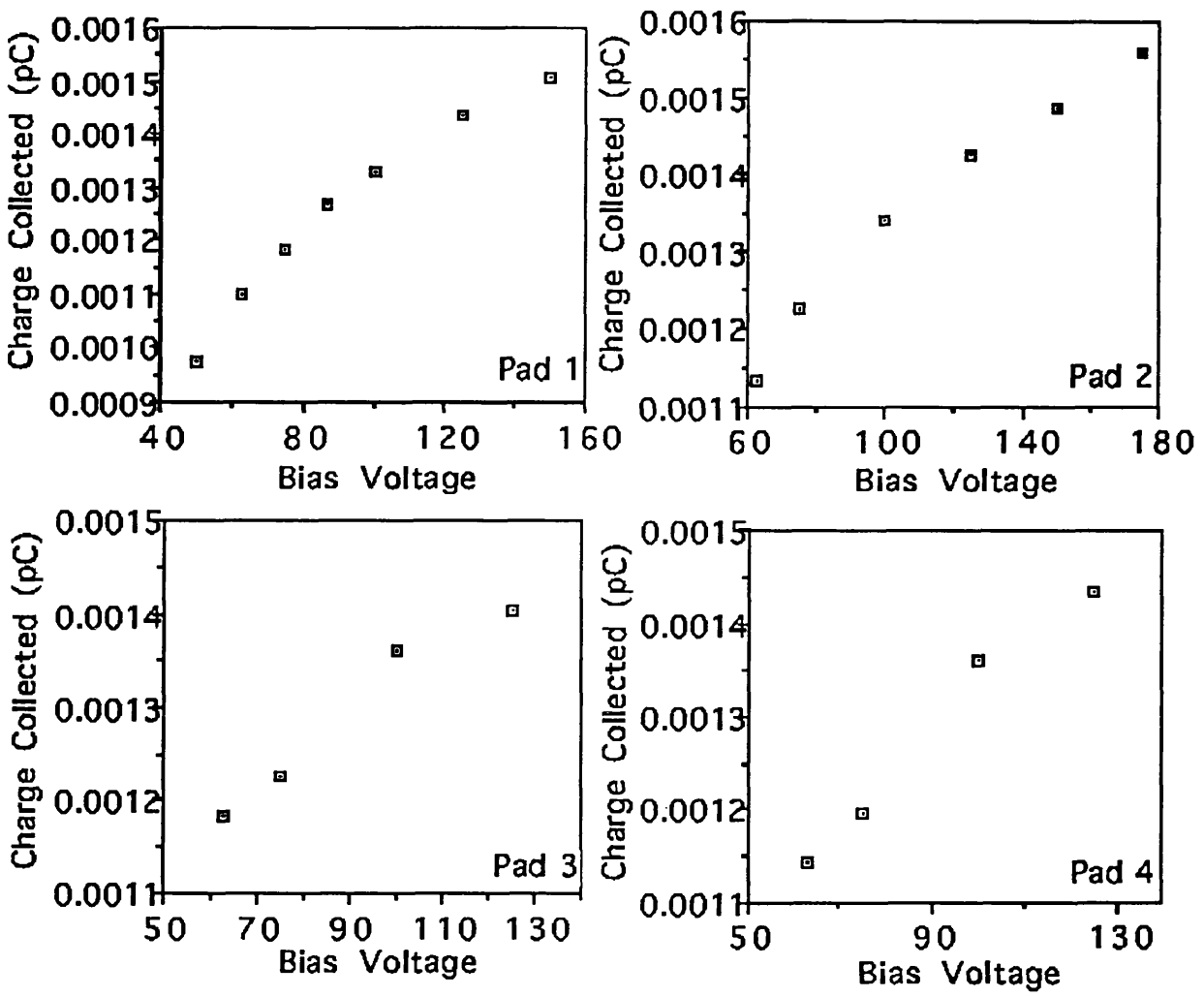

Figure 4.15: **Charge Collection for Gammas from Alenia 1 After Irradiation.**

source and a scintillator. The output signal of a photomultiplier tube coupled to the scintillator was used to trigger a gating pulse, so that signals from the detectors under test were accepted by a multichannel analyser only if they were in coincidence with a signal from the photomultiplier. In this way, only minimum ionising betas were selected from the overall spectrum of the source. A pulser was used to inject a known charge into the preamplifier in order to calibrate the system, and the calibration was checked using a silicon detector.

The noise in the system was examined by injecting charge using the pulser,

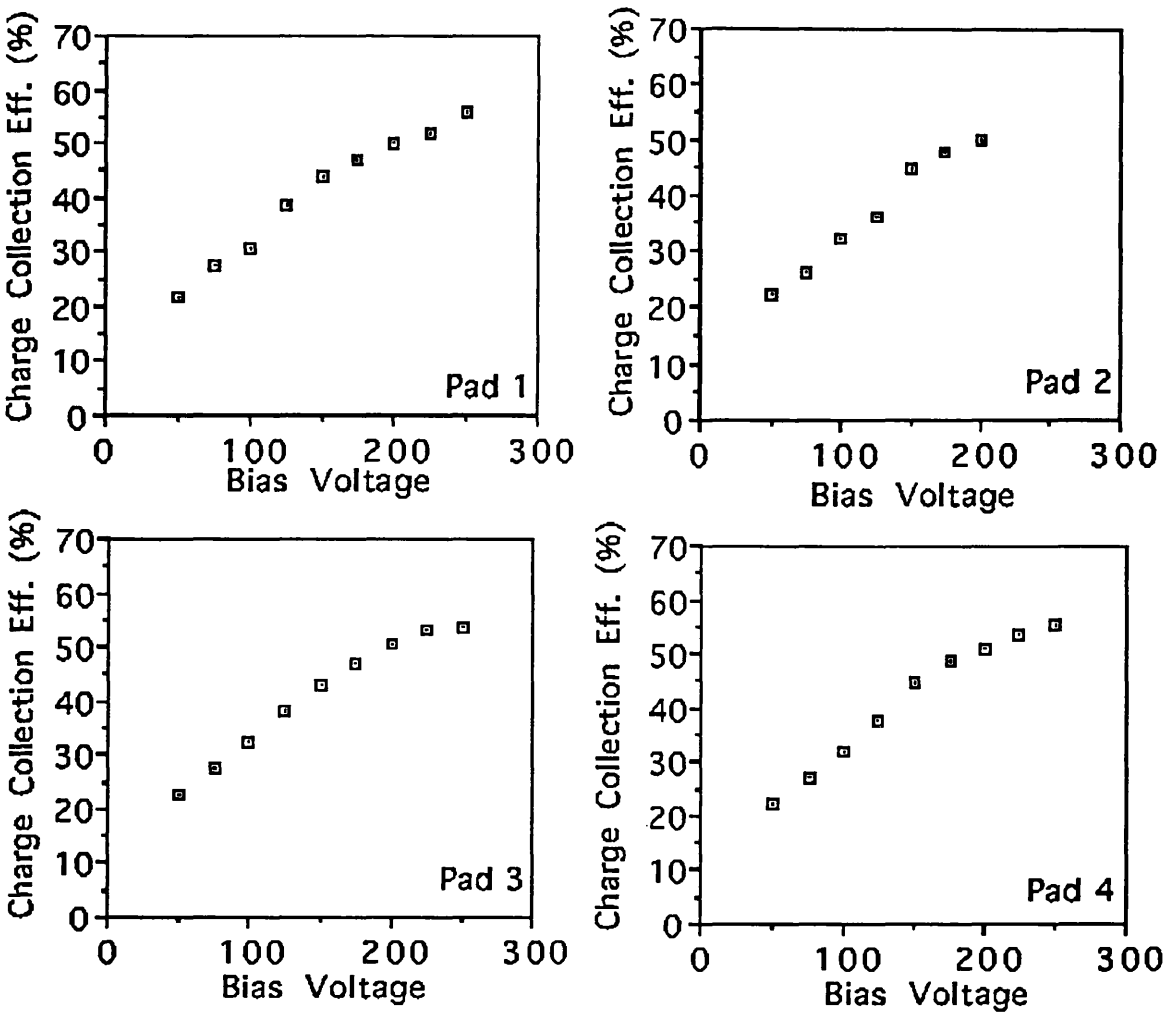

Figure 4.16: **MIP Charge Collection Efficiency for Alenia 1 Pads After Irradiation.**

leaving the detector connected and biased at the same time. The noise was then calculated from the peak full width at half maximum for the pulser MCA spectrum. The noise of the system with no detector connected was recorded in this way, and subtracted in quadrature from the figure obtained with the detector connected, in order to estimate the noise due to the detector alone. This figure was then used in calculating the signal to noise ratio. Measurements at different pulse shaping times yielded an increase of noise charge with shaping time from $0.5\mu s$ to $3.0\mu s$, indicating that the leakage current of the device dominated the

noise figure. The measurements quoted were taken with a shaping time of $0.5\mu s$, which was the lowest available setting on the shaping amplifier used.

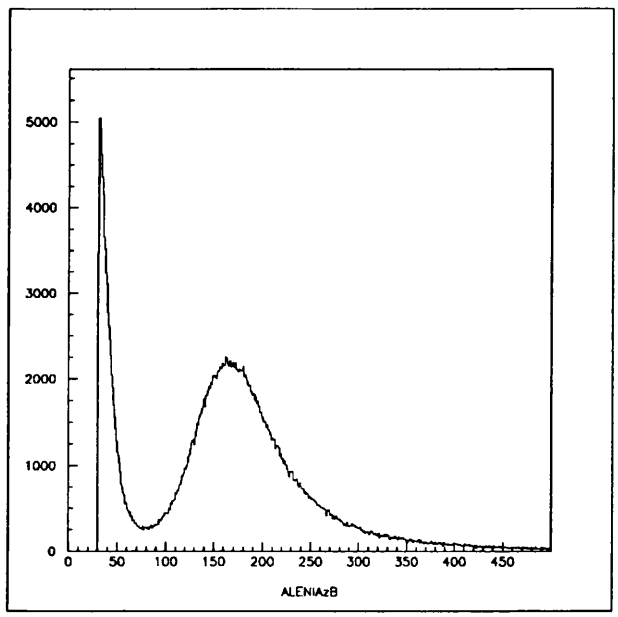

Figure 4.17: **MIP Spectrum from Alenia 1 After Irradiation.**

Charge collection efficiency for minimum ionising betas is shown in Fig.4.16 for the four Alenia 1 pads. Charge collection efficiencies up to 55% were found. The maximum signal to noise ratio was 12:1 for these devices. Pulse height spectra the pads exhibited good peak separation from the pedestal (Fig.4.17).

Alenia 2

Current-voltage characteristics for the Alenia 2 samples are shown in Fig.4.18. Although the leakage current is similar in magnitude to the unirradiated samples, the shape of the curve is not the same. This was also seen for the Glasgow devices, but it is not understood why it is the case. Pad 1 of the four pads on this chip was not tested due to breakage of its wire bond.

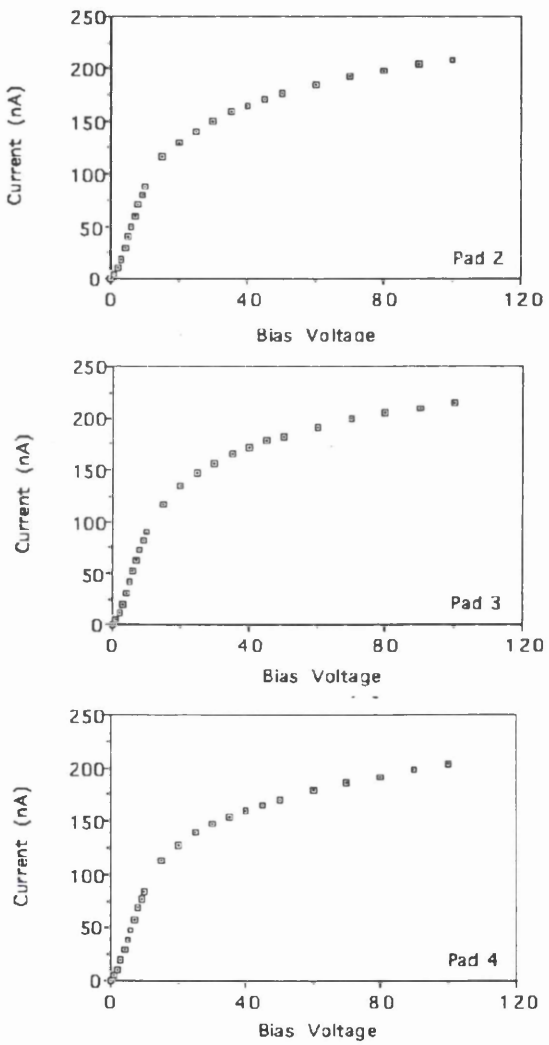

Figure 4.18: **Leakage Currents of Alenia 2 Pads After Irradiation.**

Charge collection efficiencies for minimum ionising betas obtained with the Alenia 2 samples are shown in Fig.4.19. The highest collection efficiency achieved was

34%, although a direct comparison with the Alenia 1 samples and with the unirradiated samples is difficult due to the fact that the Alenia 2 samples were appreciably thicker. The signal to noise ratio of the Alenia 2 devices reached 11:1 at room temperature, and the minimum ionising peak was still well separated from the pedestal (Fig.4.20).

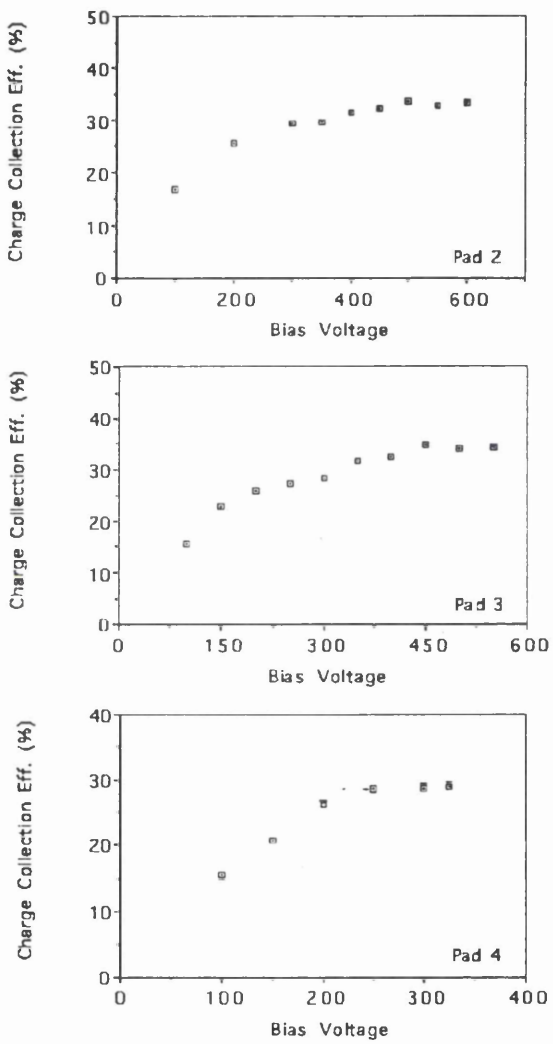

Figure 4.19: **Charge Collection for MIPs from Alenia 2 Pads After Irradiation.**

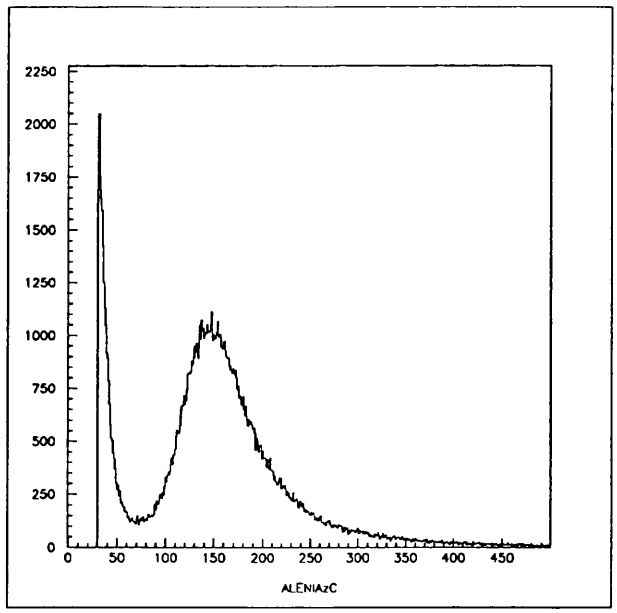

Figure 4.20: **MIP Spectrum from Alenia 2 After Irradiation.**

4.5 Conclusion

The Glasgow detectors were still useable after a neutron fluence in excess of $7 \times 10^{14} cm^{-2}$, despite a drop in charge collection efficiency. The Alenia detectors exposed to a neutron fluence of $2.9 \times 10^{13} cm^{-2}$ exhibited a good performance for MIPs, despite the appearance of a reduction in the charge collection efficiency of the devices for $5.5 MeV$ alphas and for $60 keV$ gammas. The Alenia detectors exposed to a neutron fluence of $7.3 \times 10^{13} cm^{-2}$ appear to have deteriorated more rapidly than the Glasgow devices; however, the performance of these devices before irradiation is not known, so that further work will be needed for a definite evaluation. In any case, a good signal to noise ratio was still exhibited by the detectors without the necessity for cooling to supress high leakage currents as is the case for silicon.

The effect of the type of starting material on radiation hardness should be investigated in order to obtain the best possible performance. In particular, the radiation hardness of liquid phase epitaxial material would be worth examining, in view of the very good performance of this type of material before irradiation. More work remains to be done, but it would appear that gallium arsenide is, as hoped, worth investigating as an alternative for silicon in the manufacture of radiation hard detectors.

References

[1] VAN LINT,V.A.J. *Nuclear Instruments and Methods A253(1987) 453-459*

[2] MESSENGER,G.C. and ASH,M.S. *The Effects of Radiation on Electronic Systems (VNR)*

[3] DIETL,H et al *Nuclear Instruments and Methods A253(1987) 460-466*

[4] EDWARDS,M. *GaAs Detectors and Electronics for HEP (World Scientific,1992)*

[5] FRETWURST,E. et al *Nuclear Instruments and Methods A326 (1993) 357-364*

[6] ANGHINOLFI,F.et al *Nuclear Instruments and Methods A326 (1993) 365-372*

[7] BEAUMONT,S. et al. *Nuclear Instruments and Methods A322 (1992)*

[8] ANGHINOLFI,F.et al *Nuclear Physics B32(1993) 250-259*

[9] LEMEILLEUR,F.et al *Nuclear Physics B32(1993) 415-424*

[10] EDWARDS,M.et al *Nuclear Instruments and Methods A310 (1991) 283-286*

[11] WUNSTORF,R.et al *5th Pisa Meeting on Advanced Detectors (1991)*

[12] ATLAS Collaboration *CERN/LHCC/92-4*

[13] STEVENSON,G.R. and Russ, J.S. *Nuclear Physics B23A(1991) 356-362*

[14] WUNSTORF,R.et al *Nuclear Physics B23A(1991) 324-332*

[15] ATLAS Collaboration *CERN/LHCC/93-24*

[16] PITZL,D.et al *Santa Cruz Institute for Particle Physics SCIPP 91/05 (1991)*

[17] PITZL,D.et al *Nuclear Physics B23A(1991) 340-346*

[18] MOUTHUY,T. *ATLAS Collaboration Internal Note 2/9/93*

Chapter 5

Tests on Microstrip Devices

5.1 Introduction

This chapter describes the testing of microstrip detectors, most of which has been carried out at CERN, using beams of minimum ionising pions. Following successful operation of early pad detectors, it was decided to attempt the fabrication of devices with spatial resolution. The results presented here are for thick ($\sim 500\mu m$) devices, although microstrip detectors $200\mu m$ thick have been made more recently [4]. The high resistivity of semi-insulating gallium arsenide might be expected to lead to smaller charge-sharing between strips than is the case for silicon, so that devices with different strip widths and pitches have been tested. Radiation hardness is of paramount importance at LHC, so that microstrip devices have also been irradiated. A commercially made microstrip detector was obtained from Telettra SpA; this used silicon nitride for surface passivation. The performance of the device was evaluated after irradiation in order to examine any effects of the passivation on radiation hardness. Uniformity of response over the detector area was also examined. A double-sided gallium arsenide detector has been fabricated and tested; double-sided silicon devices require special processing, as outlined in Chapter 1, in order to reduce cross-talk between the ohmic strips. It was hoped that the high resistivity of gallium arsenide and the avoidance of passivation would render special processing unnecessary.

5.2 Small Glasgow-Fabricated Microstrips

The small Glasgow microstrip devices were made on MCP material, $500\mu m$ thick. They each had 32 Schottky strips, $300\mu m$ wide and $15mm$ long. The gap between the strips was $30\mu m$. The standard process for contact evaporations at Glasgow was used, with the back side of the devices being covered with a full-area ohmic contact. The masks for photolithography were supplied by Micron Semiconductor Ltd. Small microstrips were characterised in the laboratory and tested in a beam of $70Gev$ pions at the CERN SPS.

5.2.1 Laboratory Testing

The device SB3 was characterised in terms of its leakage current, noise performance and charge collection efficiency for alpha particles.

The reverse bias leakage is shown in Fig.5.1; this is a mean value for all the strips, which were quite uniform in behaviour. The region between $100V$ and $250V$ reverse bias shows a leakage current close to $35nA/mm^{-2}$. For this measurement, the strips on either side of the strip under test were held at the same potential to avoid surface currents.

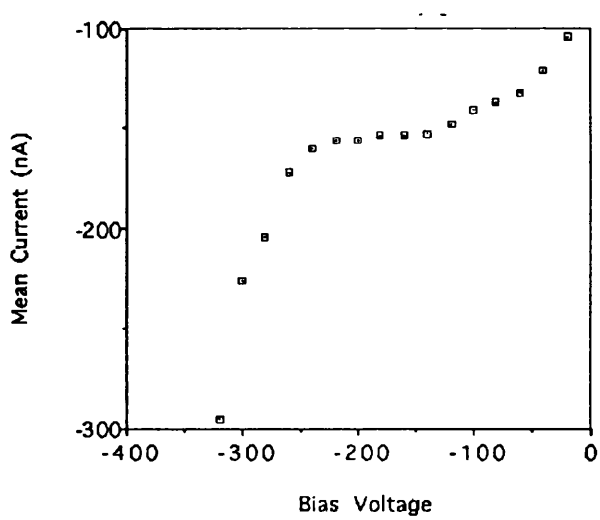

Figure 5.1: Reverse Bias Current-Voltage Characteristic

The behaviour of charge collection efficiency for alpha particles with voltage is shown in Fig.5.2. This was carried out using a standard system for spectroscopic measurements, consisting of a charge preamplifier, shaping amplifier and multi-channel analyser. The system was calibrated in terms of the number of electrons injected into the preamplifier per MCA channel by using a pulser to inject a test charge through a reference capacitor. A Charge collection efficiency of $\sim 30\%$ was found at bias voltages above $100V$, for a pulse shaping time of $0.5\mu s$. The charge collection efficiency was found to increase with longer shaping times. Problems were experienced at the highest biases used with current fluctuations through the device and with the alpha peak separating into two or more distinct components.

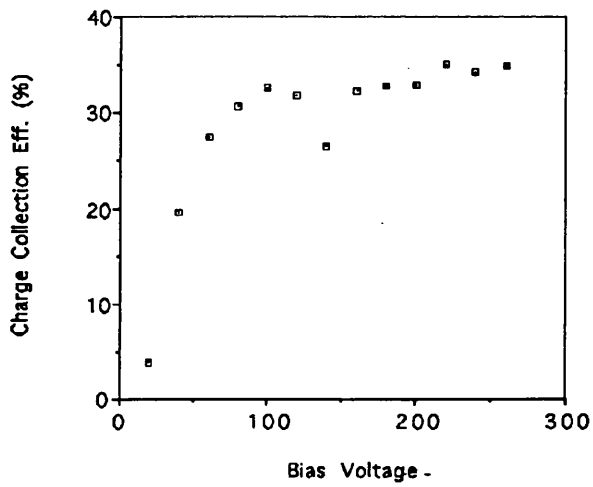

Figure 5.2: Charge Collection Efficiency for Alphas

The equivalent noise charge (ENC) behaviour of the device with voltage is shown in Fig.5.3. A pulser was used to inject charge onto a readout channel with the detector set up as for charge collection efficiency measurements. As the bias voltage on the detector was increased, the level of noise in the system also increased, leading to broadening of the pulser spectrum observed on the MCA. The ENC was calculated from the peak full width at half maximum of the pulser spectrum and the calibration of the system. The ENC can be seen from the graph to have remained fairly constant until the device began to break down around

$240V$ reverse bias. The longer the amplifier shaping time used, the lower the voltage at which the noise began to rise, indicating that the leakage current of the device was the dominant noise source.

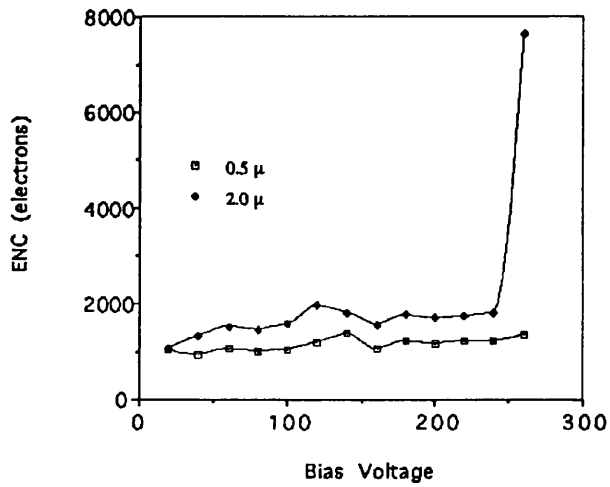

Figure 5.3: ENC vs Voltage ($0.5\mu s$ and $2.0\mu s$ shaping times)

5.2.2 Beam Testing

Small microstrips of this type were tested in a beam of $70GeV$ pions at the CERN Super Proton Synchrotron (SPS). A diagram of the system used is shown (Fig.5.4). The devices under test were arranged in a detector telescope housed in a box which was clad in copper to eliminate electromagnetic interference from external sources. The telescope itself consisted of four detector planes, 32 channels from each plane being connected to a readout system. AMPLEX chips [2] were used for readout, which consist of a charge sensitive preamplifier and shaping amplifier for each channel, with associated multiplexing electronics. The first two detector planes were silicon microstrip devices with their strips orthogonal to each other. These were $300\mu m$ thick, with a pitch of $100\mu m$ and were used to define the incoming beam. The third and fourth planes held gallium arsenide devices under test. Upstream of the box were two crossed scintillators and downstream was one scintillator; these were coupled to photomultiplier tubes, the outputs of

which were used in coincidence to provide a trigger for the readout system. Fine alignment of the box with the beam was achieved using a motorised x-y stage operated from the counting room.

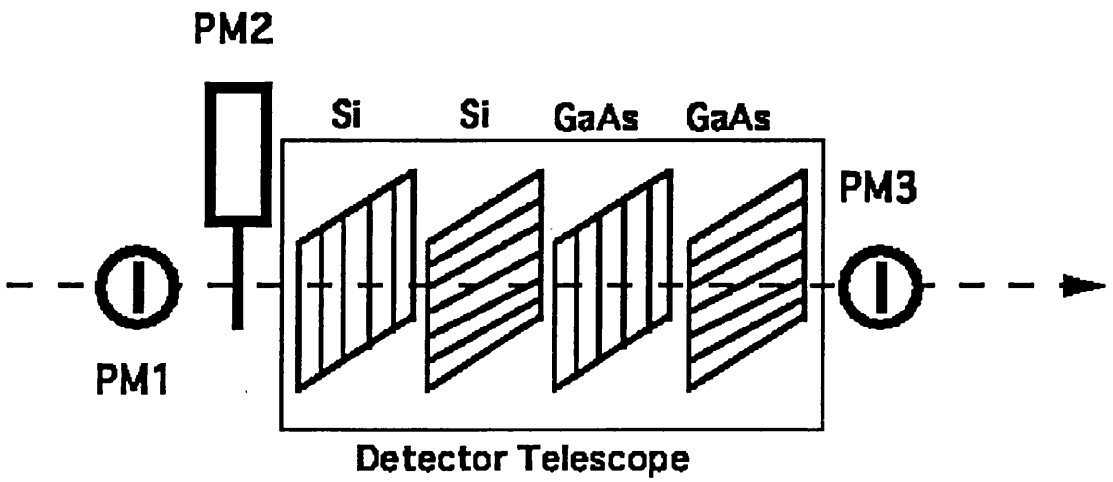

Figure 5.4: Test Beam Setup (Schematic)

For each trigger signal, all the channels in the telescope were read out sequentially, their contents digitised using a fast ADC and stored on a buffer. The number of events per burst was counted using a scaler, which was preset to veto further triggers when the maximum number of events which could be stored on the buffer was reached. In the interburst time, the buffer was read out and its contents stored on disk using a Macintosh computer running MacDaq software [3]. The data were transferred to a Vax computer for offline analysis. The system was calibrated by using a pulser and reference capacitor to inject charge onto an AMPLEX input.

5.2.3 Data Analysis

For each data run, with events triggered by the passage of particles, a short run ($\simeq$ 2500 events) was taken under the same conditions, but without beam and triggered continuously using a pulser. This allowed a noise spectrum for each channel to be built up, which was fitted offline with a Gaussian distribution of RMS σ by means of software [1] calling the CERN Program Library fitting routine HFITGA. The pedestal mean and RMS values obtained by fitting the noise spectra were used in the subsequent data analysis of the runs with beam in order to remove offsets on the channels and to allow cuts to be made for the rejection of fake hits in the detectors.

A voltage scan was performed with a small Glasgow microstrip under test, a pedestal and a data run being performed at each voltage. These runs were analysed to examine detection efficiency, signal to noise ratio, charge collection efficiency and noise. A hit on any strip was accepted if the pulse height was greater than 2.56σ for that strip. For each event, the largest pulse height in each plane was selected. The overall efficiency of the gallium arsenide device was calculated according to:

$$\mathcal{E}_{GaAs} = \frac{No.\ of\ events\ with\ hits\ in\ Si1\ +\ Si2\ +\ GaAs}{No.\ of\ events\ with\ hits\ in\ Si1\ +\ Si2} \qquad (5.1)$$

A histogram was filled, using the HBOOK program, of hit strip number of the gallium arsenide device versus hit strip number of the parallel silicon device, in order to find the spatial correlation between the strips of the two (Fig.5.5a). This allowed calculation of the expected strip number for a hit in the gallium arsenide detector from the hit position in the silicon device.

For each event with a good hit in both silicon detectors, the silicon detector with its strips parallel to the gallium arsenide device was then used to apply a spatial cut to the gallium arsenide data, hits being rejected if they did not fall within

[1] written by S.D'Auria, C.Buttar and M.Dogru

two strips of the expected position. For gallium arsenide hits in all strips passing this spatial cut, detection efficiency was calculated and a pulse height spectrum was accumulated. The resulting Landau distribution was fitted using the PAW program, using a Gaussian distribution to find the most probable pulse height (Fig.5.5b).

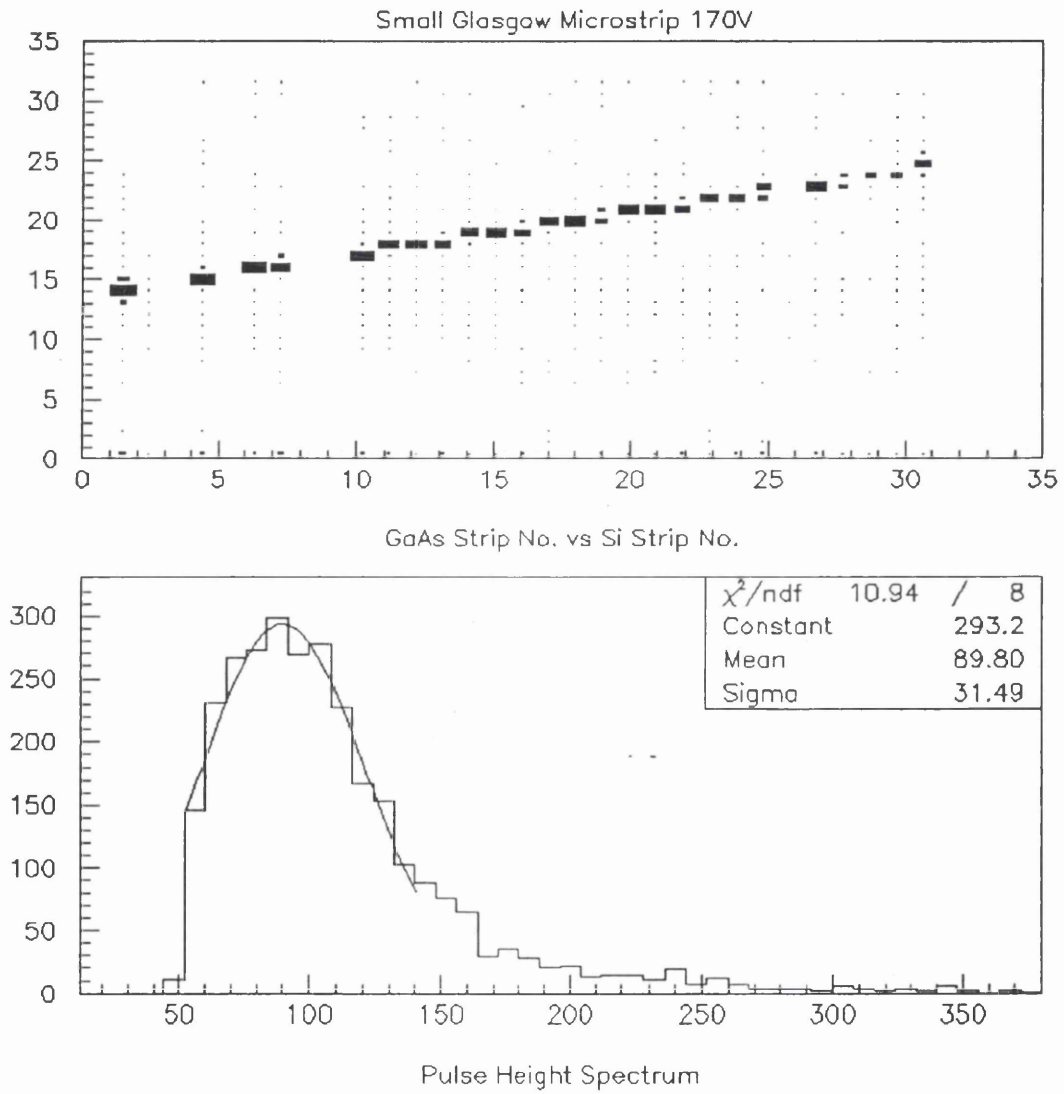

Figure 5.5: **a) Spatial Correlation Between Si and GaAs Detectors b) Pulse Height Spectrum**

The signal to noise ratio of the detector was taken to be the most probable pulse height divided by the pedestal σ averaged over all the strips. A faulty readout channel with unusually small σ was not included in the calculations. The calibration obtained during the beam testing was used to give the ENC of the device from the average pedestal σ and the charge collection efficiency from the most probable pulse height. Errors were estimated for each run by dividing it up into consecutive sections, each analysed separately. The standard deviation of the calculated quantities was thus obtained. The error on the noise charge was taken to be the standard deviation of the noise charges on all good channels. This was also the dominant error in the signal to noise figures.

The results for a small Glasgow microstrip are shown in Fig.5.6. The maximum detection efficiency achieved was 96.2% for unmatched hits and 92.3% for matched hits. Signal to noise ratio reached 5.4 : 1 and charge collection efficiency 13.2%, at $200V$ reverse bias. The charge collection efficiency rise with bias is close to linear. A small increase of noise level with bias was found. The device performance was limited by the voltage which could be applied without breakdown.

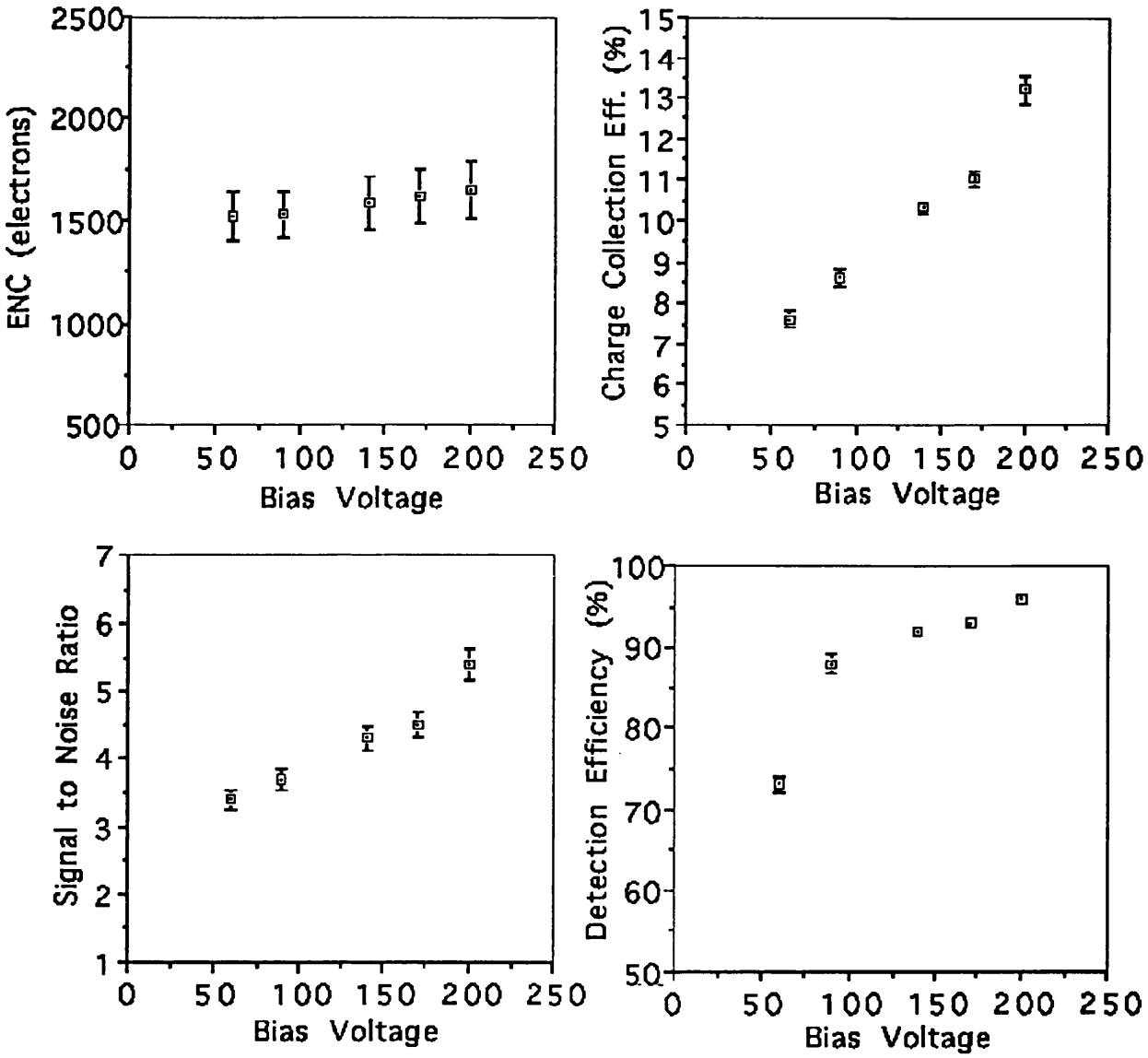

Figure 5.6: Test Beam Results for Small Glasgow Microstrip

5.3 SITP-type Glasgow Microstrip

5.3.1 Pre-Irradiation

These devices were made on MCP material, $600\mu m$ thick, according to a design for silicon microstrip detectors from the SITP collaboration, using masks supplied by Micron Semiconductor Ltd. They had 64 strips, each $275\mu m$ wide, at a pitch of $375\mu m$ and $24mm$ long. Beam testing was performed for a device of this type at the SPS, using $70GeV$ pions.

The beam test arrangement was slightly different for this device, with the two silicon detectors having their strips parallel to each other, to allow for more precise determination of the gallium arsenide strip through which any incident particle had passed. This required slightly different analysis software, but the calculations of the device behaviour remained the same as before. A voltage scan was performed, and overall detection efficiency reached 98% at $400V$. A signal to noise ratio of 8.6 : 1 was found, with a charge collection efficiency of 16%. Results are shown in Fig.5.7. Fig.5.8 shows results for a second device of the same type, characterised in the same way. The behaviour of the two devices is within $\sim$ 10% of each other.

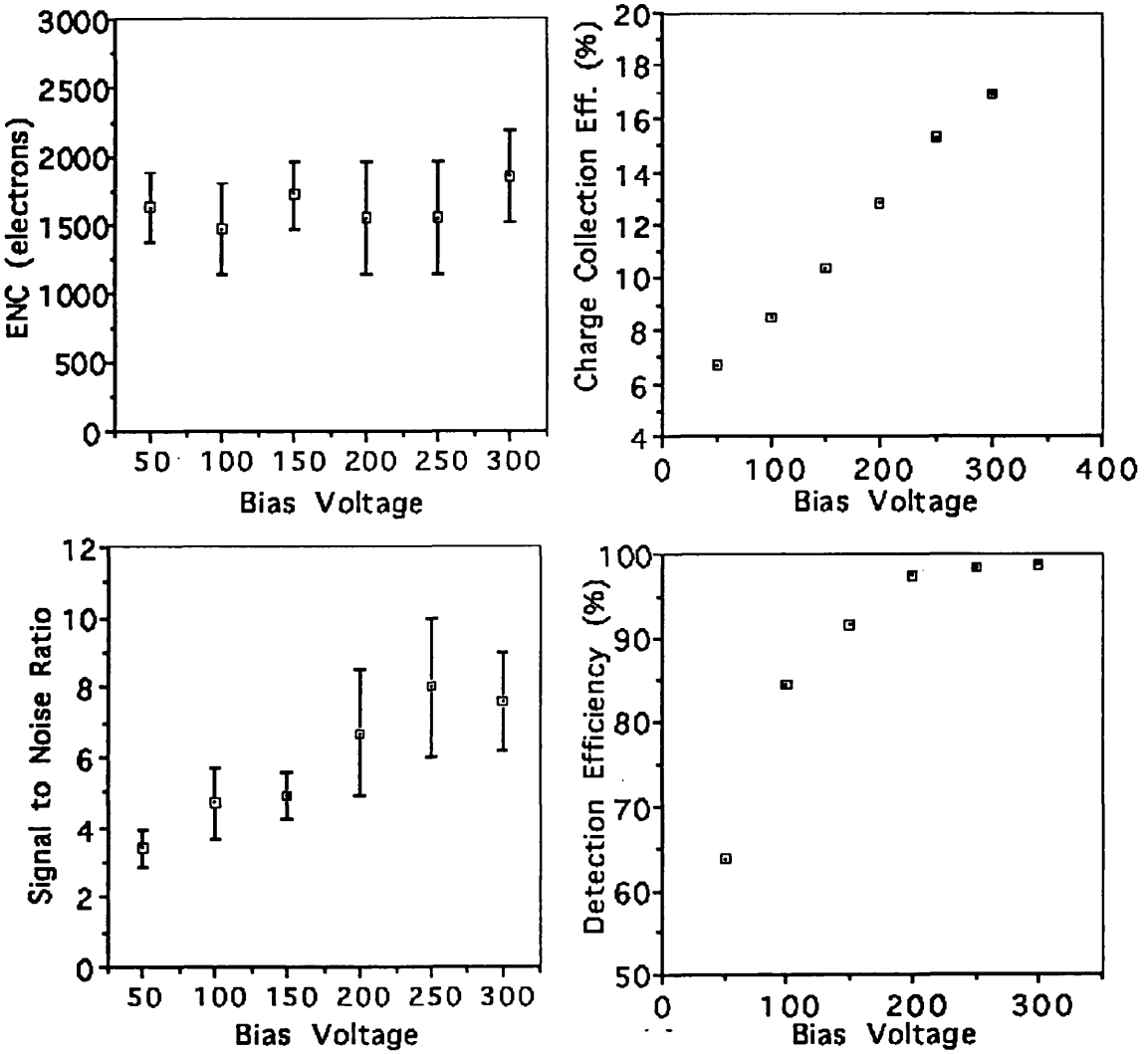

Figure 5.7: SITP1 Beam Test Results

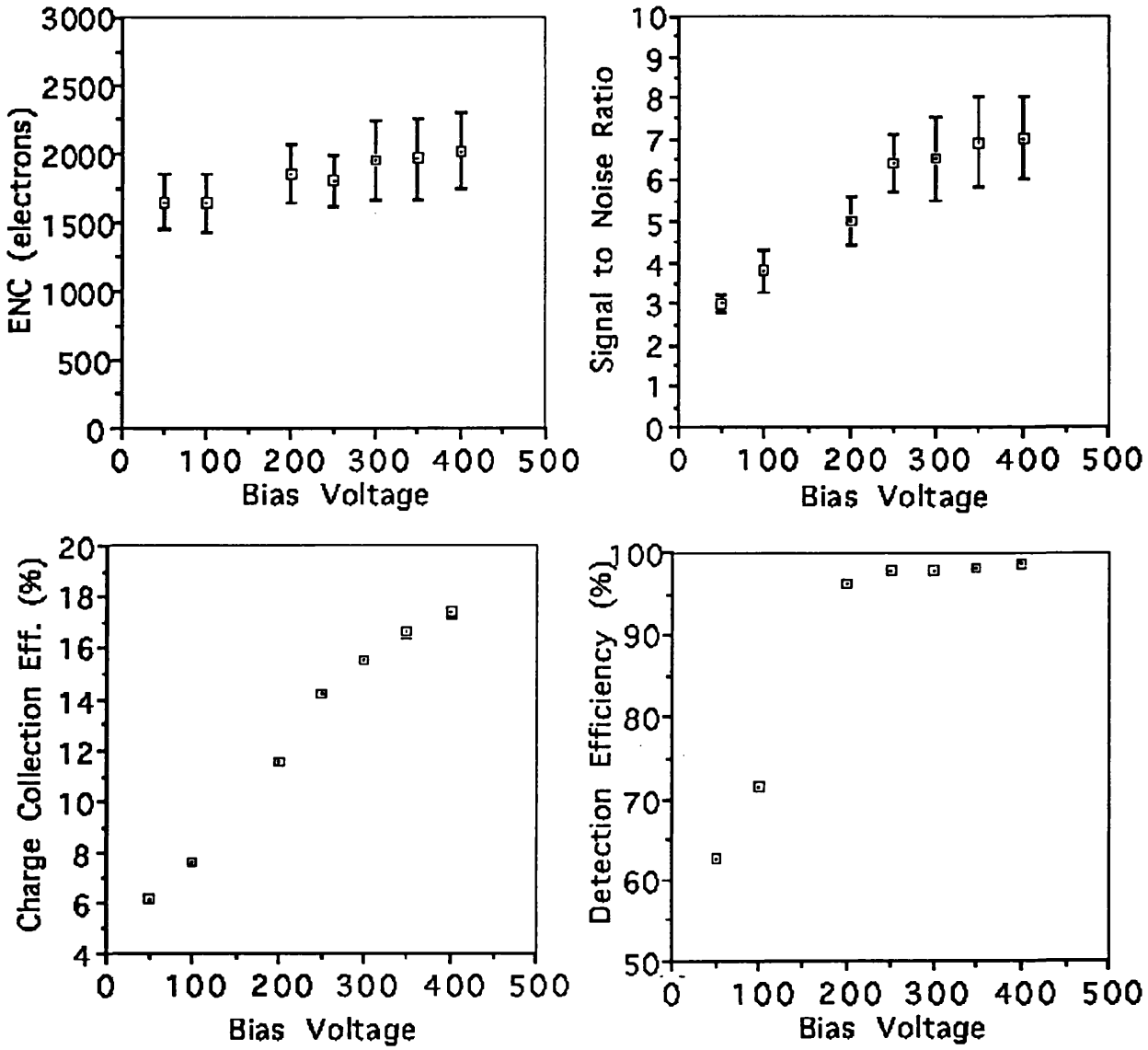

Figure 5.8: **SITP2 Beam Test Results**

5.3.2 Post-Irradiation

The device whose behaviour is shown in Fig.5.8 was exposed to a fluence of 10^{14} neutrons per cm^2 at the RAL ISIS facility, and re-tested in a beam of 7 GeV minimum ionising pions at the CERN Proton Synchrotron (PS). The behaviour after irradiation is shown in Fig.5.9. An increase in noise at the level of a few percent is apparent, although it should be noted that no correction has been made for the effect of temperature. The charge collection efficiency has fallen to around 80% of its initial value, resulting in a drop in the signal to noise ratio of a similar magnitude. The detection efficiency of the device remained excellent. Pulse height spectra for this detector before and after irradiation are shown in Fig.5.10 and Fig.5.11. It should be noted that the calbration for Fig.5.10 was 82 electrons per ADC channel, whilst that for Fig.5.11 was 43 electrons per channel.

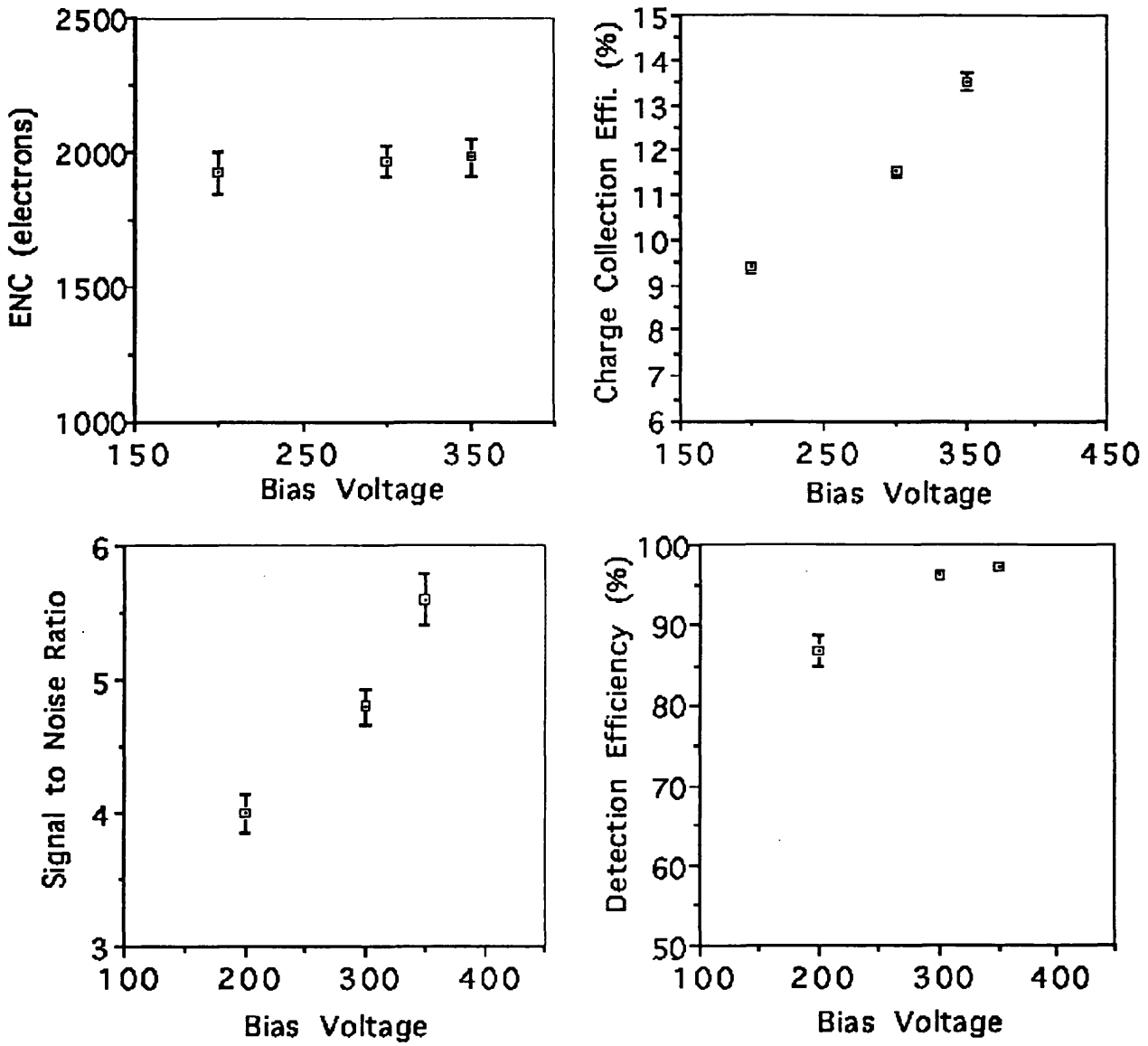

Figure 5.9: Irradiated SITP2 Beam Test Results

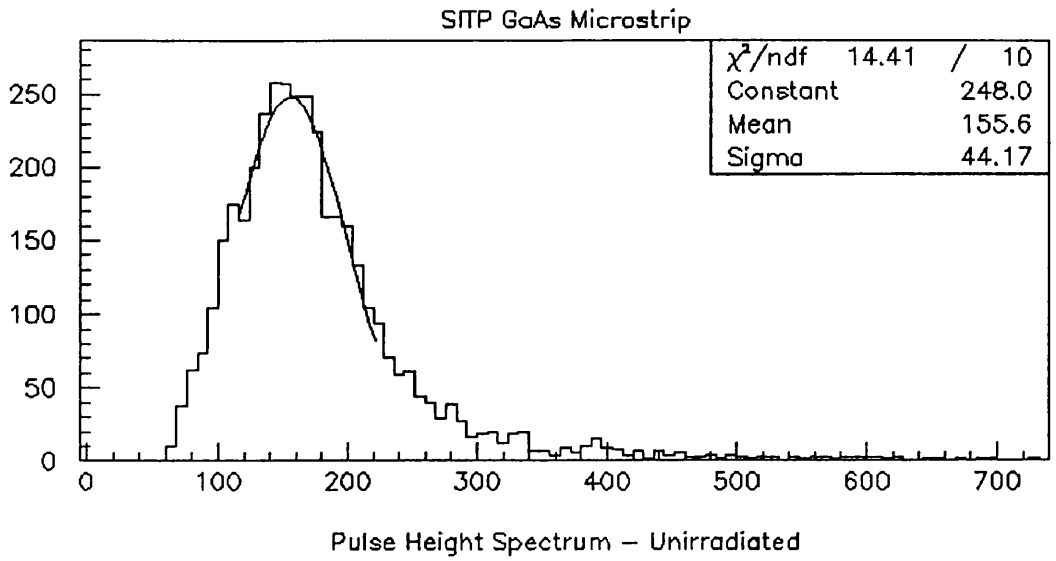

Figure 5.10: **SITP2 Pulse Height Spectrum-Unirradiated** (Calibration of 82 electrons per channel)

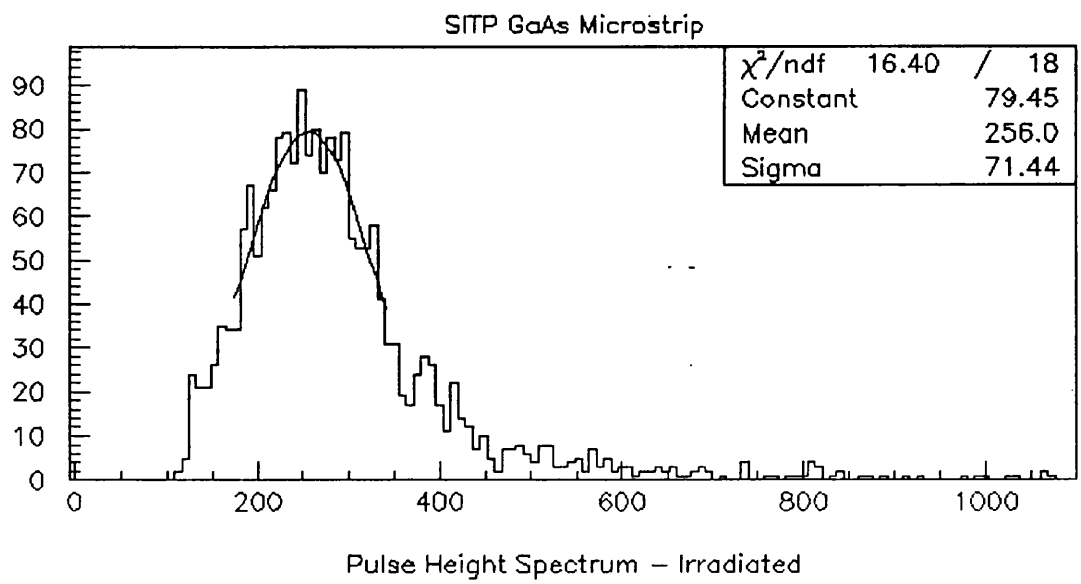

Figure 5.11: **SITP2 Pulse Height Spectrum-Irradiated**

The charge collection efficiency has fallen, but the peak sigma divided by the mean value remains unchanged. (Calibration of 43 electrons per channel)

5.4 The Modena Detectors

These devices were fabricated in the Department of Physics at the University of Modena. The substrate used was semi-insulating LEC-grown gallium arsenide, with resistivity $1 \times 10^7 \Omega cm$ and carrier mobility $5 \times 10^3 cm^2 V^{-1} s^{-1}$. The wafers were 3 inch in diameter and $625 \mu m$ thick. The principal difference in fabrication between the Modena detectors and the Glasgow detectors was the processing of the ohmic contact. During annealing of the standard type of ohmic contact, with an alloyed Au-Ge layer, the two materials form a eutectic mixture, which liquefies and melts the surface of the gallium arsenide substrate. The resulting junction may depart from planarity. The Modena devices used a layer of palladium $80nm$ thick, followed by a layer of silicon $160nm$ thick, deposited using an electron beam evaporator. The contact was annealed in two stages, one at $200°C$ for $30min$ and one at $350°C$ for $30min$. The annealing results in the formation of an n^+ layer of silicon-doped gallium arsenide via two consecutive solid state reactions and thus avoids the morphology problems which may be introduced by liquid phase reactions [4]. The Schottky contacts of the Modena devices consisted of $98nm$ of titanium followed by $500nm$ of gold. Leakage currents of $\sim 4nA/mm^2$ were reported by the manufacturers. The Modena microstrip device had strips $4cm$ long and $200\mu m$ wide, at a pitch of $400\mu m$.

Two Modena devices were tested in a $7GeV$ pion beam at the PS. The detector telescope was set up with both layers of silicon devices having their strips parallel to those of the Modena detector. The second gallium arsenide plane was oriented with strips orthogonal to the three previous planes.

The performance of a Modena detector in the beam is shown in Fig.5.12. The noise performance is similar to that of the Glasgow devices; however it was possible to apply a higher bias voltage to the Modena device. Above $700V$, the noise was found to rise markedly. The charge collection efficiency showed an almost linear increase with bias up to $700V$, but above $700V$ increased

rapidly with further voltage increase. At such high bias voltages, the pulse height spectrum obtained no longer exhibited the expected shape of a Landau distribution (Fig.5.13 and Fig.5.14). The signal to noise ratio behaved in a similar manner to the charge collection efficiency. The maximum charge collection efficiency obtained was 40%, which yielded a signal to noise ratio of 15.5 : 1. Throughout the range of fields applied to the device, it was found to exhibit a lower detection efficiency than the Glasgow devices at the same field, despite exhibiting a higher signal to noise ratio. This was especially noticeable at the smallest fields used. It was proposed that this might be due to a dead region between the strips, which were further apart than those of the Glasgow detectors. A measurement of the sensitive region using an electron microscope as for the simple devices was performed [5] and it was confirmed that this was the case.

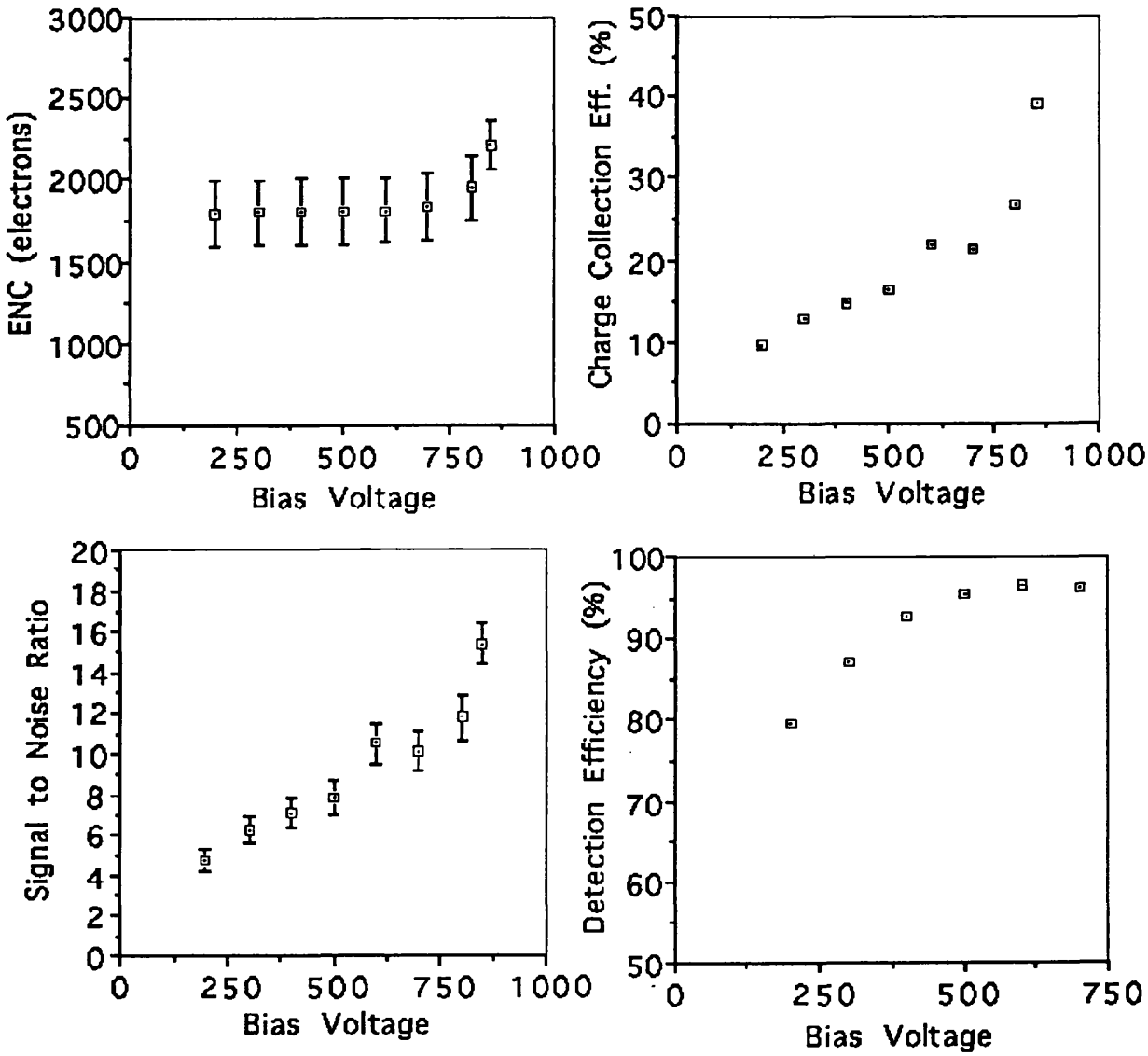

Figure 5.12: Modena Test Beam Results

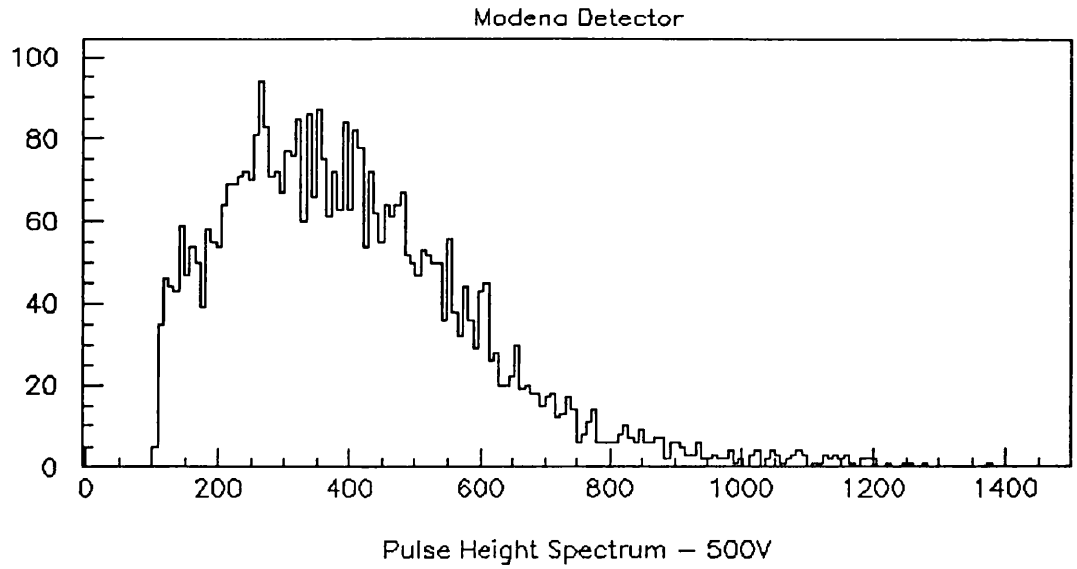

Figure 5.13: **Modena Microstrip - 500V**

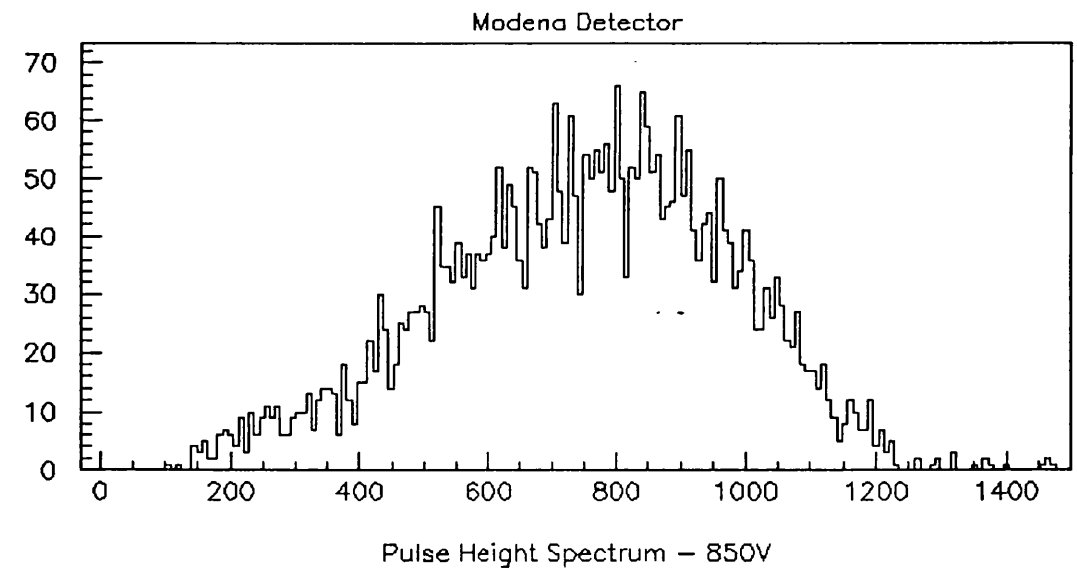

Figure 5.14: **Modena Microstrip - 850V**

5.5 The Telettra Detectors

5.5.1 Pre-Irradiation

These detectors were made by Telettra SpA, using a $450\mu m$ thick semi-insulating LEC-grown substrate. The back contact was a full-area ohmic contact, and the strips were Schottky contacts, $100\mu m$ wide and 25 mm long, at a pitch of $200\mu m$. Silicon nitride passivation was used on the surface of the device on the strip side only. A Telettra device was tested in the beam at the SPS. A run was taken with the maximum possible voltage before breakdown, and the data analysed for overall performance and uniformity [6]. Overall charge collection efficiency was 17% and signal to noise ratio 6.4 : 1 at a bias of $375V$. Sixteen individual strips were examined, and found to have signal to noise ratios within $+/-11\%$ of the mean value. Detection efficiency was found to reach 97% for individual strips, the mean value being less than this due to strips at the edge of the device performing less well than the rest. Variations in charge collection efficiency between strips and along individual strips were within the bounds of the variation of the calibration from channel to channel of the readout electronics. Charge-sharing between strips, which was very small for the Glasgow devices, was found to reach $\sim 3\%$ for the Telettra devices.

5.5.2 Post-Irradiation

A Telettra device was exposed to 10^{14} neutrons per cm^2 at the ISIS facility, and tested in a beam of $7GeV$ pions at the Proton Synchrotron. New software was written to allow examination of the uniformity of the device after irradiation. Runs at different voltages were first analysed in order to examine the overall performance of the detector, following which a run at $350V$ was chosen for analysis in more detail. The telescope arrangement was the same as for the Modena runs, so that the number of hits in any particular strip in the first silicon detector could be used to examine the variation of detection efficiency across the Telettra device. Similarly, detection and charge collection efficiencies along the Telettra

strips were evaluated by using the orthogonal gallium arsenide device to provide a longitudinal coordinate for any hit. Histograms were filled with pulse heights for each Telettra strip and for each section along the length of the strips. These were then fitted using Gaussian distributions to find the most probable pulse height. The signal to noise ratio of each Telettra strip was calculated.

Fig.5.15 shows the overall behaviour of the device as the bias voltage was varied. The noise does not increase appreciably with applied bias in the range shown, and is slightly lower than the previous devices tested. The charge collection efficiency shows a linear rise with applied bias voltage; extrapolating to $375V$ yields a charge collection efficiency of 15.5%, which is $\sim$ 90% of the value before irradiation. The signal to noise ratio shows the same reduction. Detection efficiency remains excellent; the behaviour shown is that for spatially matched hits in an area of the device where all channels worked well.

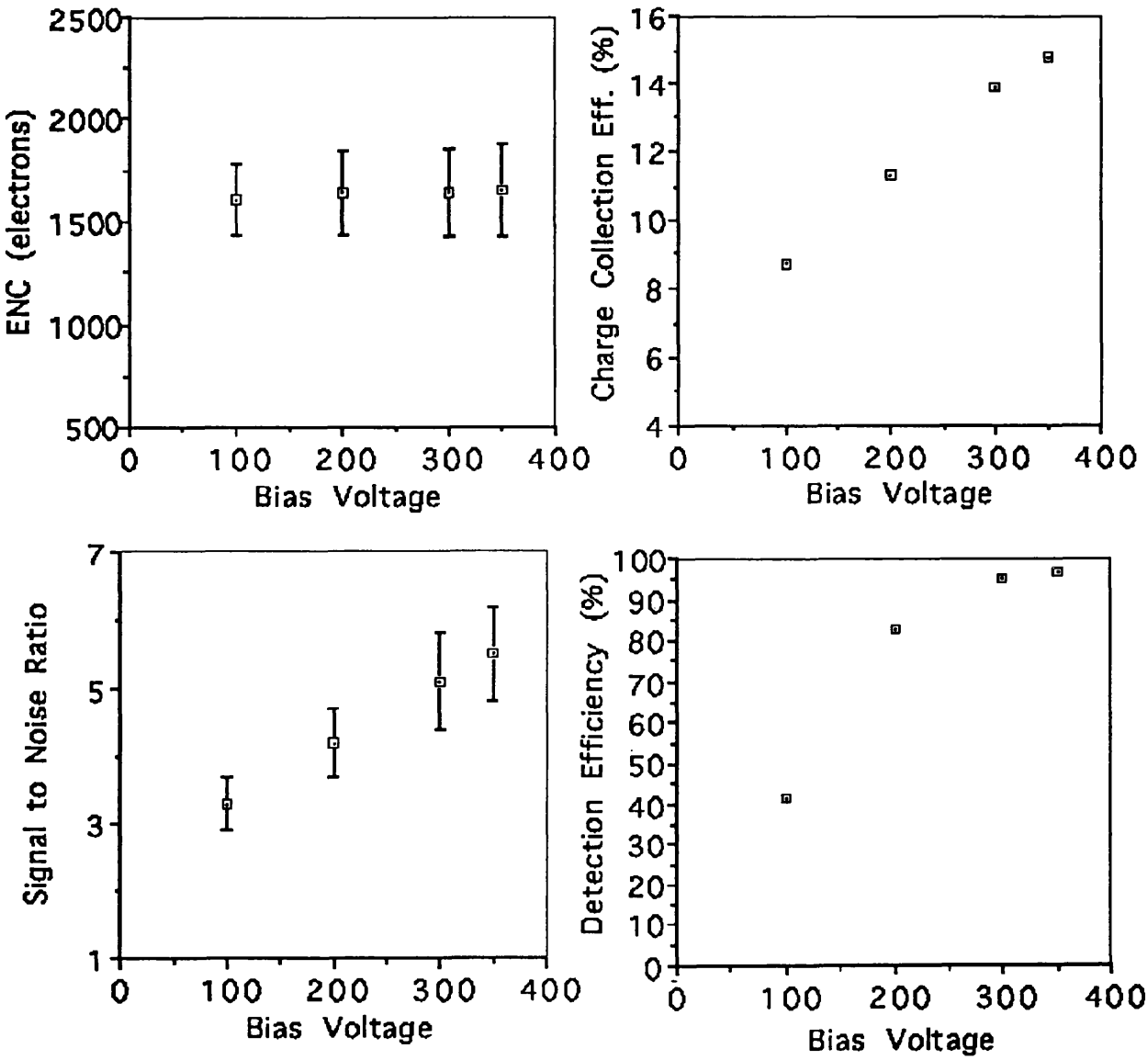

Figure 5.15: Telettra Microstrip Beam Test Results After Irradiation

The variation of the behaviour of the device from strip to strip is shown in Fig.5.16. A small increase in the noise across the detector is seen in Fig.5.16, where the error bars represent the variation of the calibration of the readout electronics from channel to channel. Channel 11 is a dead electronics channel, and strips 29 and 32 are noisy. Sufficient hits were accumulated in strips 18 to 30 during the beam run to allow for the pulse height spectra to be fitted. The charge collection efficiency showed good uniformity for channels which were working well. The noisy channel 29 also exhibited a poor charge collection efficiency, and channel 24 showed no hits; as some charge sharing between strips was present, the adjacent channels 23 and 25 showed an apparent drop in charge collection. The signal to noise variations followed those in charge collection efficiency. Detection efficiency of the Telettra device as a function of the silicon 1 strip number through which the incident particle tracks have passed is shown; good strips show good detection efficiency. The silicon 1 strips 20 and 21 are correlated with the bad Telettra channel 24 and the silicon 1 strips 27 and 28 are correlated with the bad Telettra channel 29, hence the poor detection efficiency at these points.

Variation of the device behaviour along the strips is shown in Fig.5.17. For these graphs, only good channels are included. The gallium arsenide 1 strip number was used to define the distance along the strip. The Modena device was in the "gallium arsenide 1" position for this run, so that each strip corresponded to a distance of $400\mu m$ along the Telettra strips. The uniformity along the strip length of charge collection efficiency and detection efficiency was found to be very good.

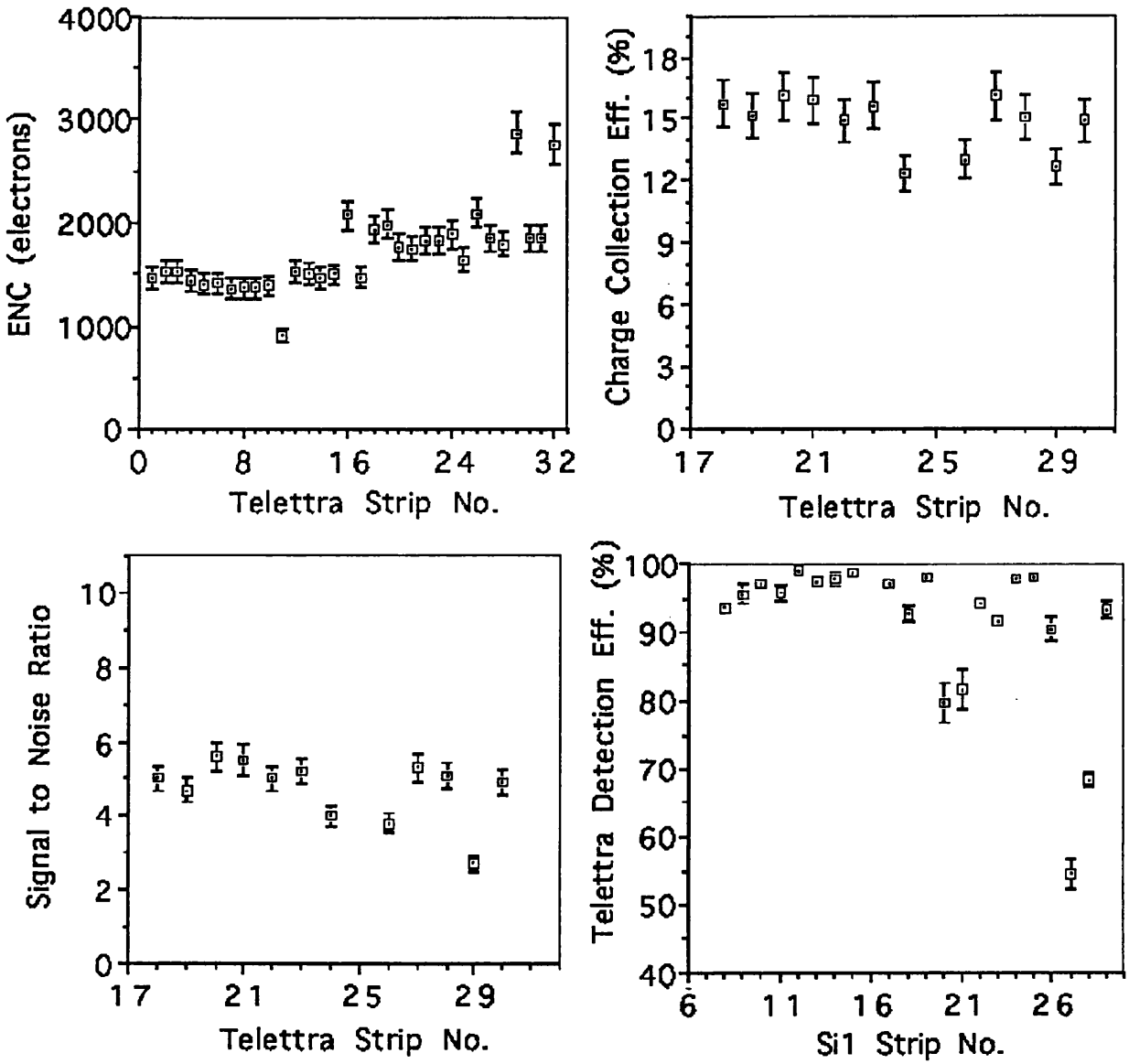

Figure 5.16: Telettra Microstrip Strip-to-Strip Uniformity (350V)

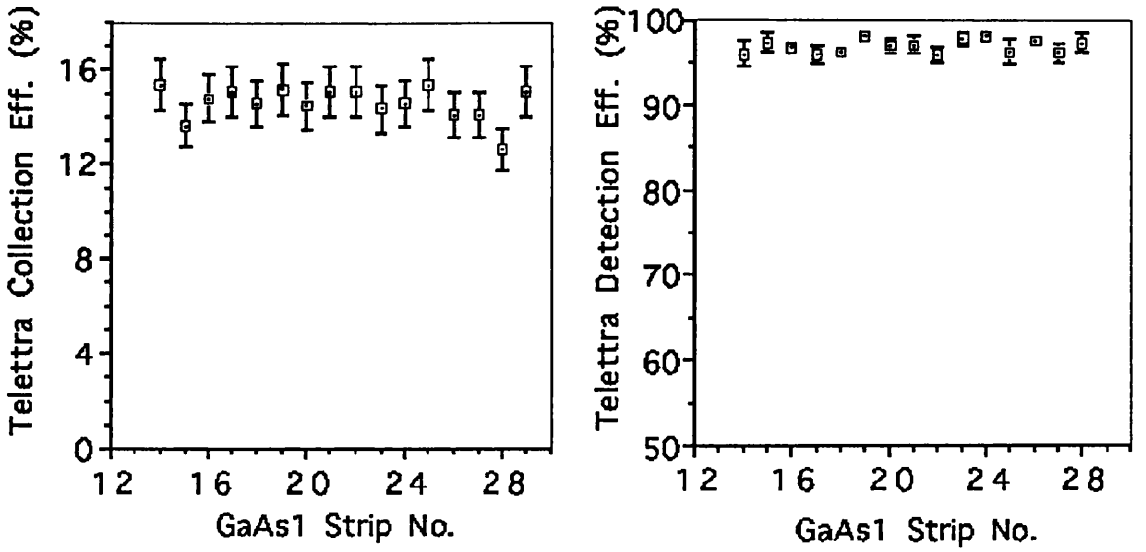

Figure 5.17: **Telettra Microstrip Longitudinal Uniformity** (350V)

5.6 The Double-Sided Detector

After the successful fabrication of double Schottky diodes at CERN, as outlined in the previous Chapter, it was decided to attempt the fabrication of a double sided microstrip device, capable of supplying position information in two directions for each hit. This type of device would reduce the amount of scattering material when used instead of two layers of conventional devices in a detector system at LHC. A double-sided microstrip detector was fabricated at Glasgow on a wafer supplied by MCP Ltd., with Ti:Au strips on both sides, orthogonal to each other. The strips were 275μ wide, at a pitch of 375μ, and the device was 650μ thick.

The device was tested in a beam of 70 GeV pions at the SPS. Data from a run at 400V reverse bias were selected for this data analysis, which used software taking account of charge clusters and using more sophisticated tracking. The detector telescope used two layers of silicon devices with strips parallel, behind which was the GaAs device. The two sides of the device were denoted GaAs1 (cathode side) and GaAs2 (anode side). The GaAs detector was AC-coupled to the readout by means of a network of capacitors, the arrangement for one channel being shown in Fig.5.18; the rest of the readout was DC coupled.

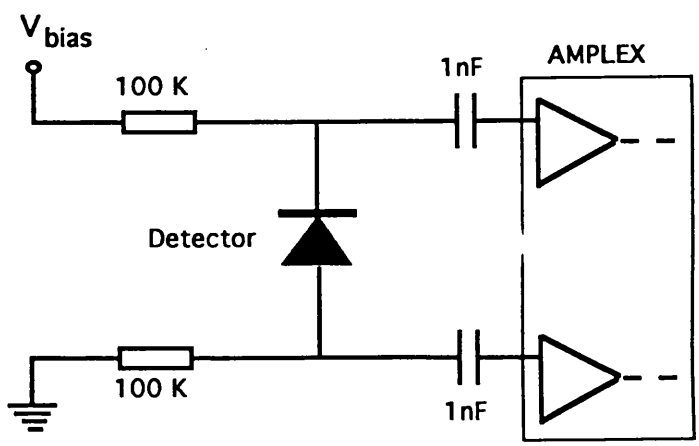

Figure 5.18: **Coupling of the Detector to the Readout Electronics**

Figs.5.19 and 5.20 show spectra from single strips on each side of the device. Peak separation from the pedestal is clearly better on the cathode side.

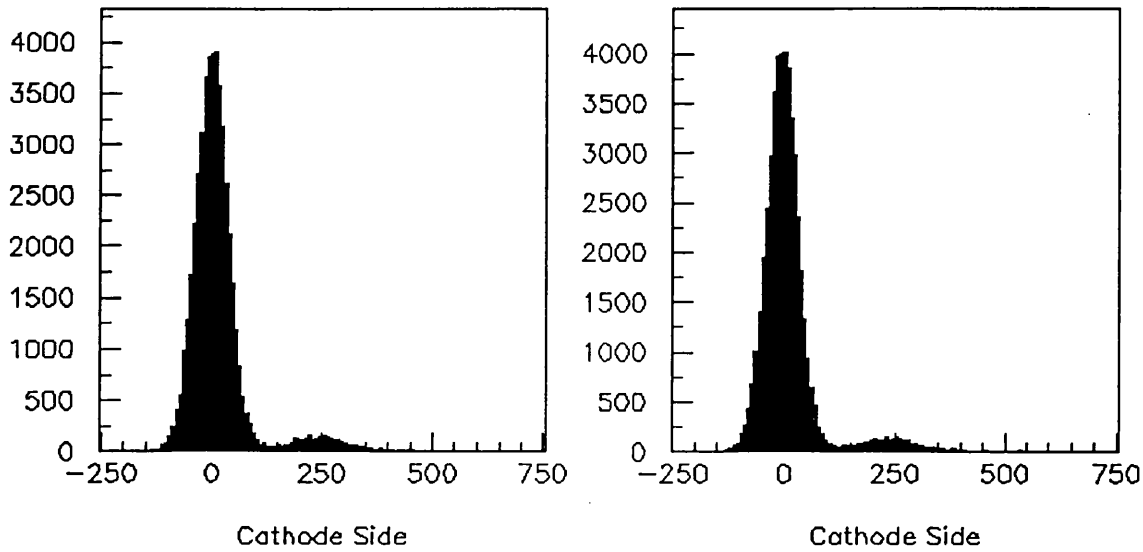

Figure 5.19: **Single-Strip Spectra GaAs1 (Cathode) Side.**

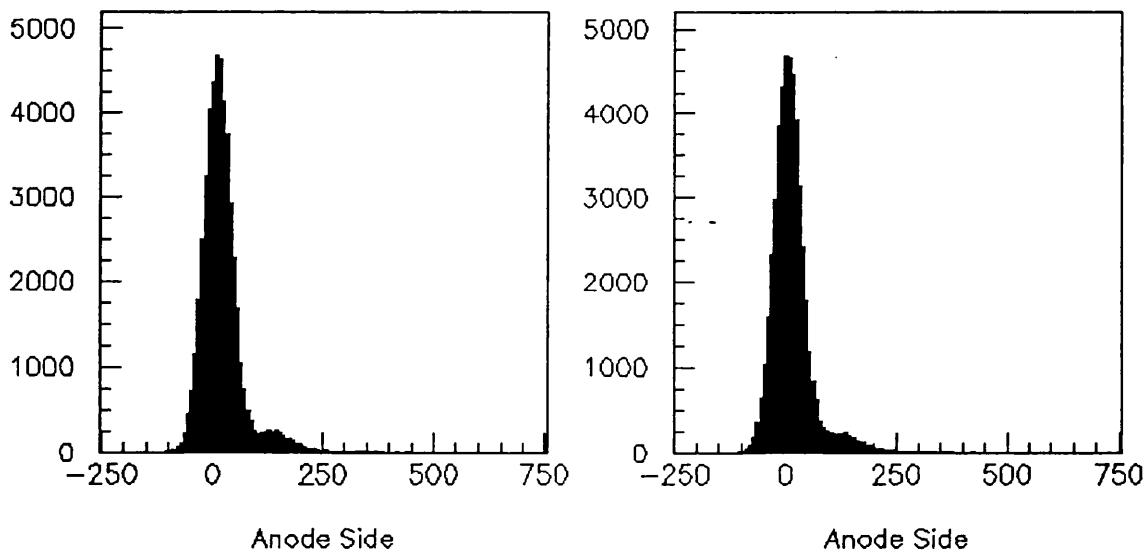

Figure 5.20: **Single-Strip Spectra GaAs2 (Anode) Side.**

Overall pulse height spectra were plotted for tracks as follows. For each event, the channels of each plane were looped through and the total pulse height was found for clusters of all adjacent strips with pulse height greater than 2.56 σ. The

cluster position was then calculated according to:

$$X = \Sigma q_i x_i / \Sigma q_i \tag{5.2}$$

where q_i is the charge on the ith strip, x_i is the distance of the centre of the ith strip from the edge of the detector and the summation is over all strip numbers i in the cluster. The expected position of a hit in the second Si detector was calculated from the hit position in the first. If a cluster was found within plus or minus one strip pitch of the expected position, a track was extrapolated back to the GaAs device.

If a cluster was found in the GaAs strips parallel to the Si strips (GaAs2), it was accepted as being real if its position was within 1.5 times the GaAs strip pitch. A pulse height spectrum of good hits was accumulated, and the upper part of the resulting distribution was fitted with a Gaussian distribution in order to find the most probable ADC channel number (Fig.5.21).

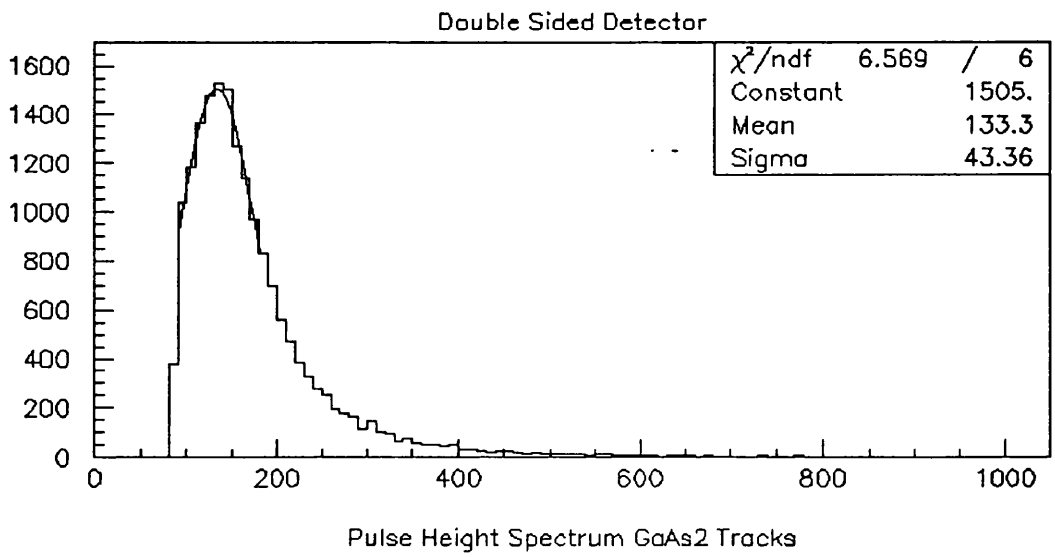

Figure 5.21: **Pulse Height Spectrum GaAs2 (Anode) Side.**

A pulse height spectrum was accumulated for GaAs1, which had strips perpendicular to the Si strips, by demanding only that a track was found in the other

planes and fitted in the same way (Fig 5.22). Data from strips or readout channels which appeared to be bad were ignored; the criterion for a strip to be bad was taken to be that a strip had a pedestal σ of less than 20 channels or greater than 60 channels, a good strip having a σ close to 40 channels.

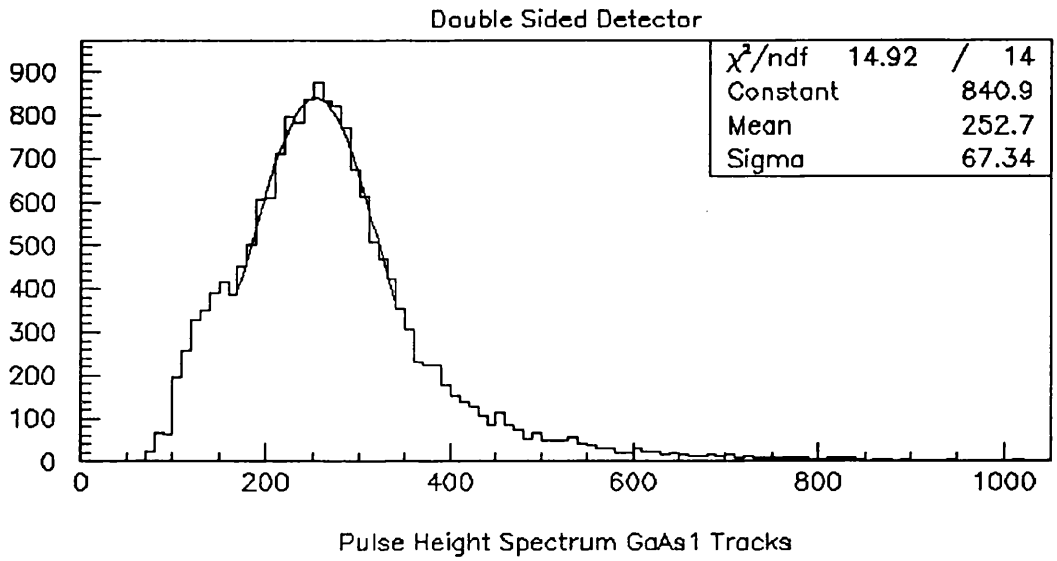

Figure 5.22: **Pulse Height Spectrum GaAs1 (Cathode) Side**

The system was calibrated using the pulse height spectra from the Si devices for events in which a good Si track had been found. This gave a calibration of 71 electrons per ADC channel for Si detectors 300 μ thick, assuming a most probable rate of energy loss of 28 keV per hundred microns for MIPs in Si.

The pedestal σ overall was 40.4 channels for GaAs1, with standard deviation of 7.8 channels. For GaAs2, it was 36.9 channels with standard deviation of 7.1 channels, excluding bad strips. The peak position was channel 253 in GaAs1 and channel 133 in GaAs2, yielding a signal to noise ratio of 6.2:1 and 3.6:1 respectively. Charge collection efficiency was 21 % for GaAs1 and 11 % for GaAs2.

Detection efficiency was also calculated for the two sides of the GaAs device. The overall detection efficiency of GaAs1 was found to be 86 %, and that of GaAs2

was 92 %. The value for GaAs1 is lower than expected from the individual strip spectra due to three faulty strips or readout channels. The arrangement of the Si devices did not allow for correction of this in the analysis, but the good peak separation from the pedestal of the individual strips indicates that they are probably giving full detection efficiency. Detection efficiency for hits spatially selected as before was calculated for GaAs2 and the matched detection efficiency taken as the ratio of the number of such hits to the number of Si tracks. The matched detection efficiency for GaAs2 was 89 %. For the GaAs2 calculations, the Si devices were used to select an area of GaAs2 where there were no bad strips.

It would seem unexpected that the charge collection efficiency, and hence signal to noise ratio, should be higher for one side of the device than the other. As the clustering algorithm only considered strips to hold a signal if their pulse height was greater than 2.56 σ, charge sharing around the noise level was ignored. If the total charge collected on both sides was the same, but shared over a greater number of strips on one side than the other, the side exhibiting a greater sharing would exhibit a lower measured charge collection efficiency.

Charge sharing was examined for events with a hit in all planes. For each plane, the strip with maximum pulse height was selected, and the charge on such strips was averaged over all events. The charge on nearby strips was also averaged over all events, but no cut was used, in order to see charge sharing which was at the level of the noise. This procedure was carried out over five strips on either side of the strip holding the maximum pulse height. For GaAs1, there was found to be no appreciable charge sharing with adjacent strips (Fig.5.23), and the average pulse height on the central strip was 280 ADC channels. For GaAs2 (Fig.5.24), the pulse height on the central strip was 170 channels, with 16 % of this value appearing on each of the adjacent strips. It would appear, therefore, that a difference in the charge sharing was the dominant factor causing the different observed charge collection efficiency for the two sides of the same device.

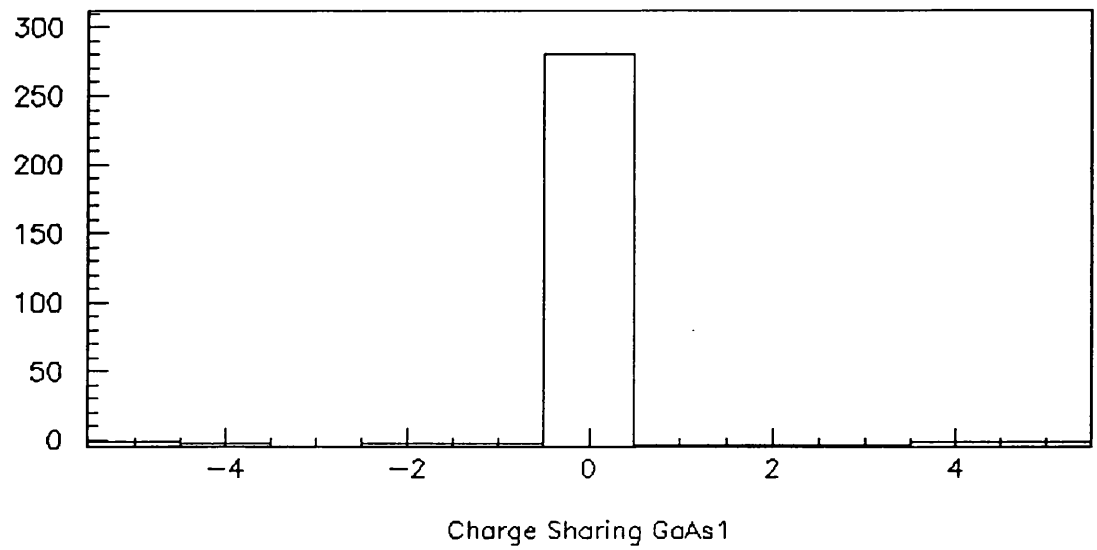

Figure 5.23: **Charge Sharing GaAs1 (Cathode) Side.**

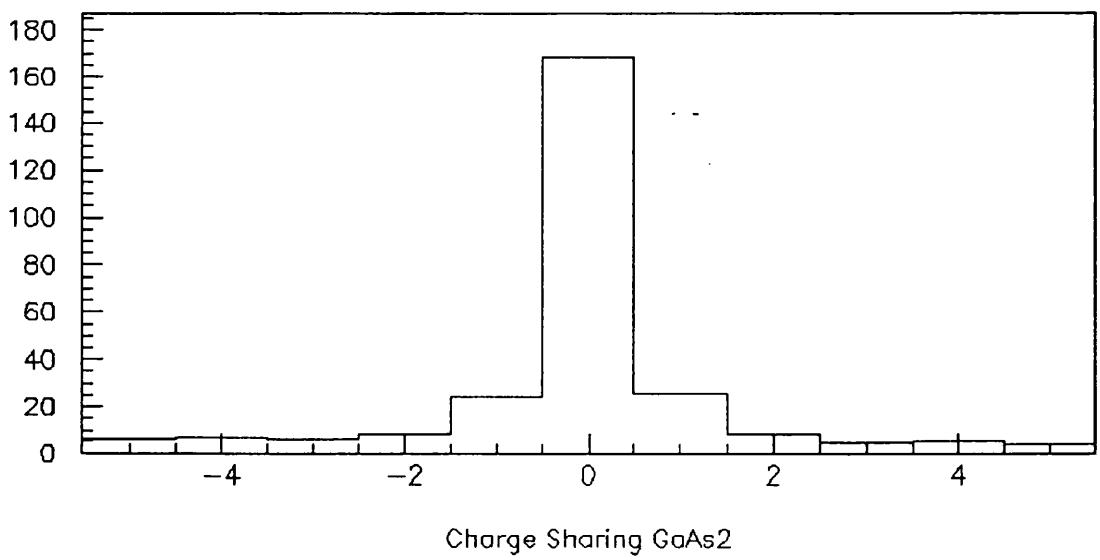

Figure 5.24: **Charge Sharing GaAs2 (Anode) Side.**

A qualitative explanation of why the sharing should be different between the two sides of the device is as follows. In Fig.5.25, a cross section of the device is shown; the strips have been represented as wires running in the same direction on each side for clarity. The two-region model is assumed, such that an incident MIP will lead to drifting charges in the upper region only. Considering, for example, an electron-hole pair generated at the centre of the high-field region as shown, as the carriers traverse that region, the change in radial distance between the carriers and the adjacent wires will be greater for the lower side than the upper. Thus, more induced charge will appear on the adjacent strips for the lower side, as has been seen.

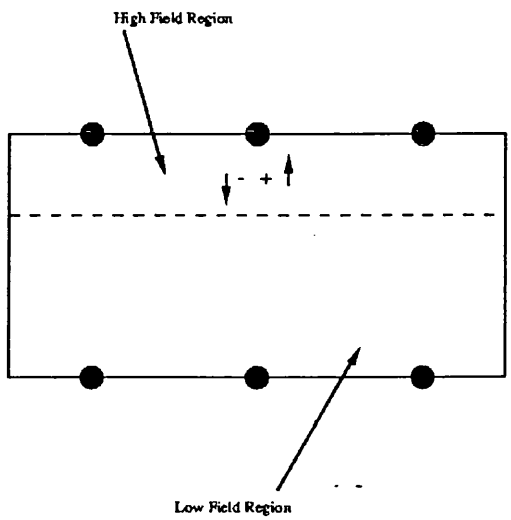

Figure 5.25: Schematic Cross-Section of the Double Sided Detector.

5.7 Conclusions

Gallium arsenide detectors have been fabricated and found to work with full detection efficiency for minimum ionising particles. They exhibit a charge collection efficiency consistent with only part of the device thickness being active, similar to the behaviour seen in tests on simple pad devices. Good correlations have been obtained between spatial information from silicon devices and gallium arsenide devices with parallel strips in the detector telescope.

Charge-sharing between strips for single-sided gallium arsenide detectors is smaller than that found for typical silicon detectors due to the high resistivity of the SI material, although it is apparent to the level of a few percent for the Telettra devices, which had $100\mu m$ wide strips, with a mark to space ratio of 1 : 1. Measurements on the Modena device, with a $200\mu m$ gap between strips at a pitch of $400\mu m$, show evidence for a dead region between the strips. This is due to the role played by defects in the material, increasing the effective donor concentration and decreasing surface depletion region widths.

The double-sided detector showed an asymmetric performance between the two sides, which has been explained qualitatively in terms of a limited region of high field on the cathode side of the device resulting in the collected charge appearing over a greater number of strips on the anode side. No crosstalk problems were evident, as hoped. It is expected that for a thinner device, the active region would extend close to the anode side, leading to a symmetric performance.

Single and double sided devices have been exposed to fast neutron fluences in excess of $10^{14} cm^{-2}$. The charge collection efficiency, and hence signal to noise ratio has been found to fall slightly at this level of irradiation. The devices still exhibit a full detection efficiency. Resistance to neutron irradiation was not reduced by the use of silicon nitride passivation.

References

[1] *RD8 Collaboration Status Report CERN/DRDC 93-37*

[2] ANSARI,R. et al. *Nuclear Instruments and Methods A279 (1989)*

[3] CINDOLO,F. *Private Communication*

[4] NAVA,F. *GaAs Detectors and Electronics for HEP (World Scientific)*

[5] D'AURIA,S. *Private Communication*

[6] D'AURIA,S. and MATULIONIS,I *RD8 Collaboration Internal Note*

Chapter 6

Conclusions

Gallium arsenide particle detectors have been demonstrated to work well for the detection of minimum ionising particles, despite charge collection efficiencies which are less than 100% and high leakage currents compared to silicon for those detectors made on semi-insulating LEC material. These currents might be reduced by use of passivation or by forming a buried rectifying junction by ion implantation, although both techniques may have effects on radiation hardness [7]. Systematic studies of the variation of leakage currents with surface preparation are now needed.

The testing of simple pad devices has yielded a model which explains the loss of charge collection in terms of a dead zone within the thickness of the detectors. The dead zone is due to a higher than expected effective donor concentration, caused by ionisation of defect levels by the applied field. However, an explanation has not yet been found for the departure from the $V^{1/2}$ behaviour predicted by theory for the active region depth dependence on bias voltage.

There exists as yet no definitive measurement of the electric field profile within gallium arsenide detectors. Due to the magnitude of the effective donor concentration in the material, the electric field is much higher close to the Schottky contact and drops much faster with distance into the devices, than would be predicted from resistivity measurements on the wafers. The high field also results

in breakdown voltages which are lower than those expected from resistivity measurements. The central problem now remaining for a quantitative model of the detectors is to predict the field distribution successfully. Thus, it would be interesting and relevant to study the field distribution experimentally using current pulse shape measurements as has been done for irradiated silicon detectors in [1], [2] and [3]. Meanwhile, work is in progress to determine the nature of the defect levels in the material, in the hope of using this information to allow a solution of Poisson's equation in the depletion region, subject to a realistic description of the space charges involved [4].

The devices made on epitaxial material showed practically full charge collection efficiency, and a depletion behaviour according to theory. Liquid phase epitaxial (LPE) material shows the best prospects amongst the epitaxial materials for use in tracking detectors, as it is already available in sufficiently thick layers, which other epitaxial growth techniques cannot match at the present time. As yet, the carrier concentrations available in LPE material are rather high for detector applications $\sim 10^{14} cm^{-3}$; once this obstacle has been overcome, then gallium arsenide will yield a performance as a detector material comparable to that of silicon. Due to the higher atomic number of gallium arsenide, it is expected to exceed silicon in performance for medical X-ray imaging.

For application in the forward region of the ATLAS detector at LHC, semi-insulating material appears to be the most likely candidate, as it is already available commercially in the thicknesses required, in the form of wafers of great enough diameter to make large area coverage feasible. As has been outlined, detectors in this region will require radiation hardness to a neutron fluence in excess of $10^{14} cm^{-2}$ per year. This is too high a dose for easy operation of silicon detectors, which at best will require long inactive periods to allow for the annealing of radiation damage followed by operation at low temperature. At worst, the reverse annealing which has become apparent in some studies [1] may preclude their operation entirely. The rapid changes in silicon detector perfor-

mance under irradiation coupled with the non-uniform particle fluxes through the proposed detector wheels would be expected to exacerbate the problems which silicon faces. Radiation hardness results for simple detectors and microstrips on SI gallium arsenide are encouraging, with full detection efficiency for microstrips after exposure to a neutron fluence of $10^{14} cm^{-2}$. Further work on radiation hardness should include testing of the LPE material and gamma irradiation of devices with passivating layers. Synergistic effects may exist between neutron and gamma irradiation [6], and these should also be investigated.

The spatial resolution of gallium arsenide microstrips still remains to be quantified, although in test-beam studies hits in the gallium arsenide planes of the detector telescope are well correlated spatially with those in the silicon planes. For silicon microstrips with strip pitch d, where $d > 50\mu m$, resistive charge division between strips allows a position resolution of $\sim d/\sqrt{12}$ [5], whilst for smaller pitch, the position resolution is given by equation (1.1), with $a_{cf} \sim 1$ assuming all strips are instrumented. Thus, the lower resistive charge division of gallium arsenide may lead to a poorer position resolution than silicon for large strip pitch. For small strips, where the lateral diffusion of charges as they drift across the device is effectively sampled, gallium arsenide might be expected to exceed silicon in performance due to its higher electron diffusion coefficient. The pitch of the strips of forward tracking wheels is expected to be $50\mu m$, which has been dictated by the need to use the same readout electronics as the silicon detectors in ATLAS. Small-pitch gallium arsenide detectors have been fabricated [4] and it is hoped to beam test them at CERN in the near future. A new detector telescope system will be employed to allow more layers of detectors for better tracking than has been possible previously.

Although more work is required, at the present time gallium arsenide appears to be an excellent candidate to play a complementary role to that of silicon in forthcoming hadron collider experiments. As a tracking detector, its speed and detection efficiency are perfectly adequate. Its greater cost will prevent gallium

arsenide from replacing silicon in those areas where silicon is adequate, but for the areas where the radiation dose is too high for silicon to be used, gallium arsenide can still survive. As the technology matures, it may be expected to play an increasing part in detectors at future colliders.

References

[1] LEMEILLEUR,F. et al *Nuclear Physics B32(1993) 415-424*

[2] KRANER,H.W. et al *Nuclear Instruments and Methods A326(1993) 350-356*

[3] GADOMSKI,S. et al *Nuclear Instruments and Methods A326(1993) 239-242*

[4] *RD8 Collaboration Status Report CERN/DRDC 93-37*

[5] HOFMANN,R. et al *Nuclear Instruments and Methods A225(1984) 601-605*

[6] MEULENBERG,A. et al *IEEE Trans. Electron Devices Vol.35 No.12 (1988)*

[7] JANOUSEK,B.K. et al *IEEE Trans. Nucl. Sci. Vol.35 No.6 (1988)*

Appendix A

Radiation Hardness of the MX7 ASIC

For use at LHC, both radiation-hard detectors and readout electronics will be required. This Appendix outlines gamma irradiation of the RAL MX7 readout chip. Although the objective in this case was to evaluate the MX7 to allow comparison with the Viking chip in terms of possible application in the vertex detector of the ALEPH experiment, the techniques used are also relevant to future studies of readout electronics for LHC. The devices tested are not the radiation-hardened version of the MX7, which will be evaluated when chips become available.

The MX7 IC consists of 128 charge sensitive pre-amplifiers with associated electronics for each channel to sample and hold the output voltage of the pre-amplifier. During operation, the quiescent level of each channel is first stored; when data capture is initiated, the pre-amplifier output voltage represents the quiescent level plus the input charge from the detector. A shift register is incorporated to multiplex the stored signal voltages onto two analogue outputs as a differential signal, which allows rejection of low frequency noise and common mode signals.

The system used for the radiation hardness tests was as follows. A 386 PC equipped with an 86004 CAMAC interface card ran software controlling the data acquisition electronics via a TRANSIAC CAMAC controller. Oxford University is acknowledged for provision of the original DAQ software. An RL858 module generated the voltage signals to control the MX7 chips, which were read out into a SIROCCO ADC via an interface unit designed by Oxford University. The SIROCCO was read out and the data stored on the disk of the PC, before being dumped to tape. The six MX7 chips tested were mounted on a hybrid PCB designed by Liverpool University.

The devices were exposed for several periods of 5 minutes duration to a ^{60}Co gamma ray source at the Scottish Universities Research and Reactor Centre. The dose rate of the source was $1.19kGy$ per hour in water [1], equivalent to $108kRad$ per hour in silicon. Thus, each exposure gave a dose of $9kRad$. The chips were biased during irradiation, but were not undergoing readout cycles. Before irradiation and after each successive exposure the response of the chips was recorded. This was achieved by applying calibration pulses to the inputs of the MX7s. Each channel of the chip is equipped with a capacitor at the input of the pre-amplifier, through which charge can be injected. These have a capacitance of $15fF$, the required charge being controlled by the voltage of the calibration pulses from the RL858 unit. The capacitors are connected in four groups of 32 channels to four calibration inputs. 100 events were recorded for pulses applied to each calibration input for charges of 9, 19, 30 and 180 thousand electrons, allowing a calibration of the system in electrons per ADC channel for each dose level.

The data were transferred to a Vax computer for analysis. All analysis software was written in the FORTRAN language, with the handling of histograms using the CERN Library HBOOK and PAW programs. For each calibration line for each chip, the mean pulse height was calculated over all the events. The average of this was taken over 3 calibrate lines. and pulse height was plotted against dose.

The fourth calibrate line was not connected, so that data from the associated channels were ignored. Of the six devices on the PCB, two were not working initially. Plots of mean pulse height versus channel number indicated that at some times, two MX7s were showing anomalous behaviour, with charge from each calibrate line appearing on two channels instead of one. The sum of the charge on the two channels was greater than the expected value. These two chips were situated on the back face of the PCB and it is believed that the problems experienced were due to a faulty connection in the control lines passing from one side of the PCB to the other. For this reason, only the results from the two working chips on the front side of the PCB will be presented here.

Fig.A.1 shows the fall of pulse height with irradiation for the $180ke^-$ and $30ke^-$ runs respectively. The gain of the two chips has fallen with increasing dose. The

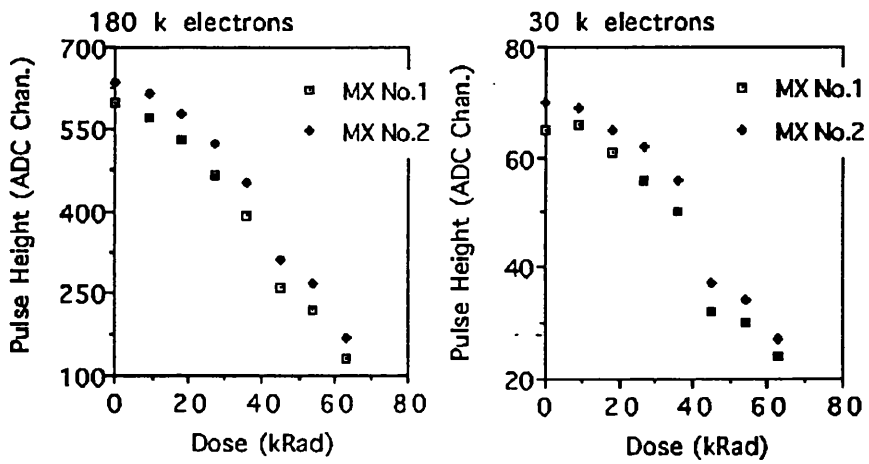

Figure A.1: **Reduction in Pulse Height with Irradiation Level.**

higher charge runs show a greater fall, indicating some increasing nonlinearity of response to injected charge. The runs at $9ke^-$, $19ke^-$ and $30ke^-$ were used to examine the behaviour of the calibration with increasing dose. Fig.A.2 shows that the calibration of MX No.1 has increased from $286e^-$ per ADC channel to $858e^-$ per channel after a dose of $63kRad$, due to the fall in gain. The calibration of MX No.2 has increased from $271e^-$ per channel to $720e^-$ per channel.

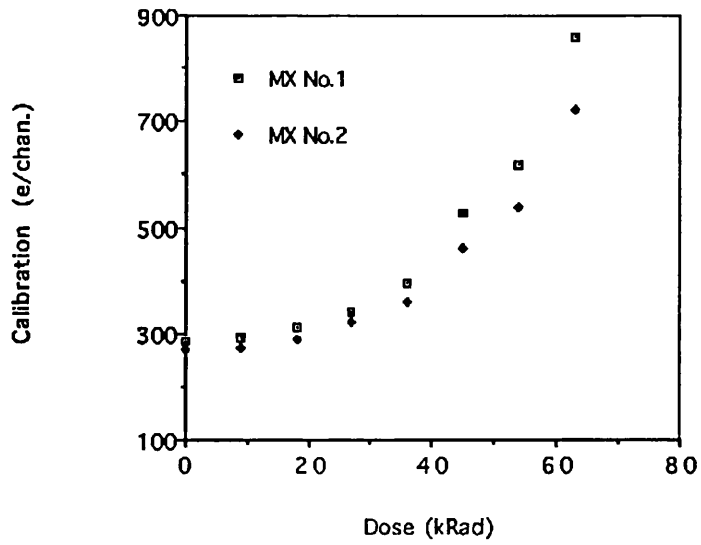

Figure A.2: **Calibration in Electrons/ADC Channel versus Irradiation Level.**

The electronic noise charge collected from the amplifier with no external capacitive load was calculated for each readout channel. The calculation was carried

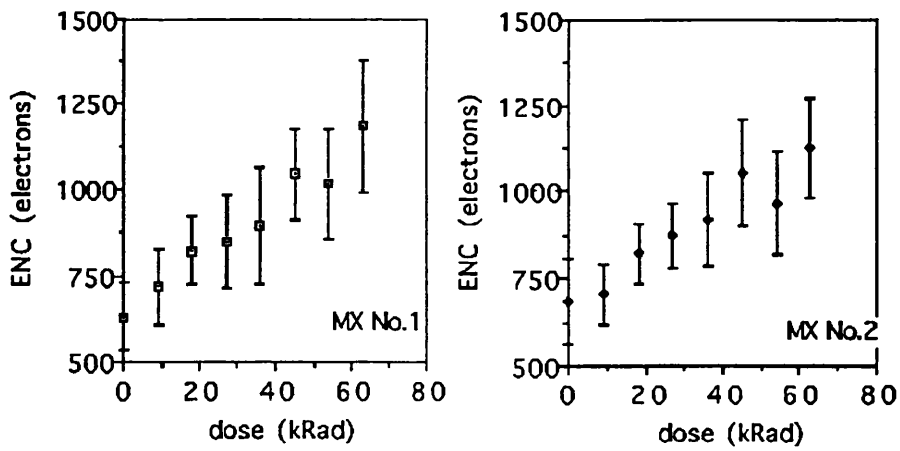

Figure A.3: **Increase in Noise with Irradiation Level.**

out by taking the three runs used in the overall calibration calculation above for each dose level, and calculating the mean pulse height over the 100 events per calibration line to obtain for each channel three values of pulse height in ADC channels corresponding to the three levels of injected charge. A least-squares

algorithm was then used to calibrate each channel in terms of electrons per ADC channel. The RMS deviation from the mean of the output pulse height values was calculated for each channel from the $30ke^-$ run, and the noise taken to be the calibration multiplied by the RMS value. The ENC results obtained in this way are shown in Fig.A.3, where the error bars represent the spread in ENC values over the channels.

The signal to noise ratio was calculated as the mean pulse height in ADC channels for each MX readout channel, divided by the RMS deviation from the mean for the 100 events. The results of this calculation are shown in Fig.A.4 and A.5, where the error bars again reflect the spread over the readout channels. The

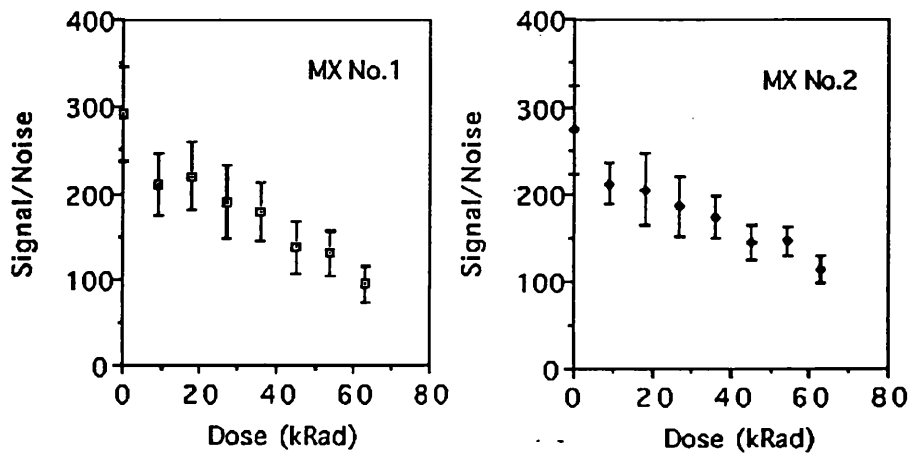

Figure A.4: **Reduction in Signal to Noise Ratio with Irradiation Level ($180ke^-$ Runs).**

fall in signal to noise ratio for the $180ke^-$ runs is greater than that for the $30ke^-$ runs due to the nonlinearity in the calibration for large injected charge. For a MIP in a typical $300\mu m$ thick silicon detector, a signal charge of $23ke^-$ would be expected, so that the fall in pulse height from the $30ke^-$ runs is indicative of the behaviour in a real situation. However, in order to calculate the signal to noise figure for a real situation after irradiation, it would be necessary to calibrate the performance of the chips in terms of noise response to a capacitance at the input,

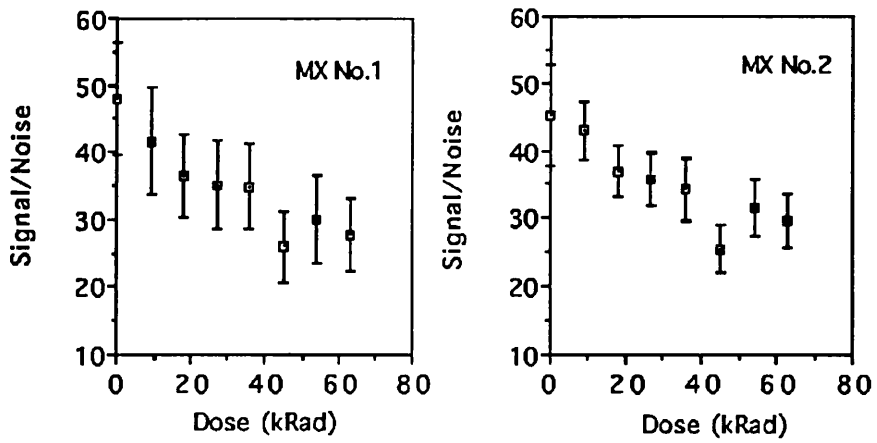

Figure A.5: **Reduction in Signal to Noise Ratio with Irradiation Level ($30ke^-$ Runs).**

in order to take account of the capacitive loading due to the detector.

Subsequent to the irradiations, it has been found that the signal to noise ratio can be increased by a factor of $\sim$ 1.7 by alteration of the timing of the pulses controlling the MX7 readout [2]. The sampling of the input signal is controlled by two strobes, denoted S1 and S2. The quiescent level is sampled at the rising edge of the S1 pulse, and the signal level is sampled at the rising edge of S2. The delay between these two sampling points was initially set at $2.2\mu s$, which allowed all the charge due to the calibrate pulses to be collected. After irradiation, lengthening this delay increased the height of the output signal for calibrate pulses, indicating that the risetime of the pre-amplifiers had changed. The best improvement in signal to noise ratio appeared to be a factor of $\sim$ 1.7 with the delay between the rising edges of S1 and S2 set to be $4.5\mu s$. A similar improvement has been obtained by alteration of the MX7 bandwidth control voltage.

The radiation-hardened version of the MX7 will be tested under irradiation in the near future. Several channels on each chip will be loaded using capacitors of different values, so that an indication of the response of the chip to detector capacitance may be calculated for each level of irradiation. In this way, the

expected signal to noise ratio will be calculated.

References

[1] Banford,H. *Private Communication.*

[2] Raine,C. *Private Communication.*